Defects and Interfaces in Ag-Alloyed PbTe Compounds for Thermoelectric Applications

Research Thesis in Partial Fulfillment of the Requirements for the Degree of Master of Science in Materials Engineering

Ariel Sheskin

Submitted to the Senate of the

Technion – Israel Institute of Technology, Haifa

August 2019, Elul 5779

ACKNOWLEDGMENTS

This research was performed under the devoted and dedicated supervision of Asst. Prof. Yaron Amouyal at the Department of Materials Science and Engineering, Technion – Israel Institute of Technology. The Minerva Foundation (Seed Grant Program) provided funding to perform experiments at MPIE Dusseldorf, Germany, and its generosity is gratefully acknowledged.

Part of the results obtained in this study were published:

- Microstructure Evolution of Ag-Alloyed PbTe-Based Compounds and Implications for Thermoelectric Performance, Grossfeld T,Sheskin A,Gelbstein Y,Amouyal ,Crystals (2017) **7(9)** 281
- Ag-segregation to dislocations in PbTe-based thermoelectric materials, Yuan Yu, Siyuan Zhang, Antonio Massimiliano Mio, Baptiste Gault, Ariel Sheskin, Min Zhu, Christina Scheu, Dierk Raabe, Fangqiu Zu, Matthias Wuttig, Yaron Amouyal, and Oana Cojocaru-Mirédina, ACS Appl. Mater. Interfaces, (2018), **10 (4)**, pp 3609–3615

TABLE OF CONTENTS

ACKNOWLEDGMENTS II

1 ABSTRACT 1

2 INTRODUCTION 2

3 LITERATURE REVIEW 3

3.1 THERMOELECTRIC EFFECT: THE HISTORY 3

3.2 THE THERMOELECTRIC EFFECT: PHYSICAL BACKGROUND 5

3.2.1Seebeck effect 5

3.2.2Peltier effect 6

3.2.3Thomson effect 6

3.2.4Thermoelectric efficiency 7

3.3ELECTRICAL CONDUCTIVITY 8

3.4THERMAL CONDUCTIVITY 8

3.4.1Lattice component of thermal conductivity 9

3.4.2The Callaway model for thermal conductivity 10

3.5A REVIEW OF THERMOELECTRIC MATERIALS 13

3.6 PBTE – BASED COMPOUNDS 15

3.6.1 Single-phase PbTe 15

3.6.2 Two-phase system based on PbTe-matrix/precipitates 17

3.7 PBTE/AG2TE-BASED SYSTEMS AND MICROSTRUCTURE EVOLUTION 17

3.8 KINETICS OF PHASE TRANSFORMATIONS 18

3.9 SYNTHESIS METHODS COMMON TO PBTE COMPOUNDS 19

4 SUMMARY AND RESEARCH GOALS 20

5 RESEARCH METHODS 20

5.1MATERIALS SYNTHESIS 20

5.2DENSITY MEASUREMENTS 21

5.3THERMOELECTRIC PROPERTIES 22
5.3.1Electrical measurements *22*
5.3.2Thermal transport- Laser Flash Analysis (LFA) *24*
5.4 MICROSTRUCTURE ANALYSIS 26
5.4.1 X-ray Diffraction *26*
5.4.2 Scanning Electron Microscopy (SEM) *27*
5.4.3 Transmission Electron Microscopy (TEM) *27*
5.4.4 Atom Probe Tomography (APT) *27*
6 RESULTS 31
6.1 MATERIALS SYNTHESIS OPTIMIZATION 31
6.1.1 HP optimization *31*
6.2 MICROSTRUCTURE CHARACTERIZATION 32
6.2.1 Phase identification: X-ray Diffraction (XRD) *32*
6.3 PRECIPITATE NUMBER DENSITY (N_v) ANALYSIS 33
6.4 THERMOELECTRIC MEASUREMENTS 39
6.4.1 Heat capacity *39*
6.4.2 Thermal diffusivity *41*
6.4.3 Thermal conductivity *42*
6.5 ELECTRICAL PROPERTIES 45
6.5.1 Electrical conductivity *45*
6.5.2 Seebeck coefficient measurements *46*
6.6 M TERIALS CHARACTERIZATION 47
6.6.1 TEM *47*
6.6.2 Atom probe tomography *51*
6.6.3 Process optimization *59*
7 DISCUSSION 62

7.1 TE MEASUREMENTS 63

7.1.1 Thermal transport properties 63

7.1.2 Electrical properties 65

7.2 MICROSTRUCTURE EVOLUTION 65

7.3 PROCESS OPTIMIZATION 67

7.3.1HP optimization 67

7.3.2Aging temperature 67

8 SUMMARY AND CONCLUSIONS 68

9 REFERENCES 70

תודות 2

תקציר 2

List of figures

Figure 1 An illustration of the Seebeck effect for N-type semiconductor(above), and P-type semiconductor (below) 5

Figure 2 A schematic illustration of a typical TE generator with p-type and n-type legs connected thermally in parallel and electrically in series with a load resistor. 7

Figure 3 The balance between the thermal conductivity, Seebeck coefficient and electrical conductivity to gain highest ZT values. The thermoelectric power factor peaks at higher carrier concentrations than does ZT. The difference between the peaks of the power factor and ZT is greater for the newer lower-k_l materials. These trends were modelled using data of Bi_2Te_3[8] 8

Figure 4 The Calculated relative thermal conductivity vs precipitate number density, for 100,200 and 300K. the TC shows a signifacant reduction when reaching number density of 10^{20} and above.[20] 12

Figure 5 figure of merit ZT of current state of the art thermoelectric materials versus temperature. The dashed lines show the maximum ZT values for bulk state of the art materials, and the solid lines show recently reported ZT values, many of which were obtained in bulk nanostructured materials.[23] 13

Figure 7 Normalized thermoelectric properties and ZT versus doping concentration at 300 K for n-type $Si_{80}Ge_{20}$. Curves are calculated from a numerical model developed by the authors. In the figure k refers to thermal conductivity, S refers to the Seebeck coefficient, and s refers to the electrical conductivity[23]*.* 14

Figure 8 Phase diagram of binary Pb–Te system.[24] 15

Figure 9 closed-in chart of the PbTe phase diagram around the 50 at% concentration, showing a stable area at the temperatures which we are doing the synthesis of our material 16

Figure 10 The quasi-binary phase diagram of (PbTe)1-x(Ag_2Te)x system showing the strongly temperature dependency of Ag_2Te in PbTe. 18
Figure 11:Differential thermocouple (taken from Netzsch® official website). 23
Figure 12: A schematic description of the principle of Seebeck coefficient measurement (taken from Netzsch® official website). 24
Figure 13: A typical configuration for the measurement of the Seebeck coefficient (taken from Netzsch® official website). 24
Figure 14 A schematic description of the LFA apparatus (taken from Netzsch® official website). 25
Figure 15: V(x) is potential energy as a function of distance away from the surface of a specimen, x = 0. $\boldsymbol{Va}(\boldsymbol{x})$ *is the potential energy of an atom in the absence of an electric field, E, and* $\boldsymbol{Vi}(\boldsymbol{x})$ *is the potential energy of an ion in its ith ionization state in the presence of E.* $\boldsymbol{Ii}$ *is the ith ionization state of an ion, e is the charge on an electron, n is the number of electronic charges, Λ is the cohesive energy of a solid, .* $\boldsymbol{\phi 0}$ *is the local work function,* $\boldsymbol{Qn}$ *(E) is the height of the Schottky hump, and* $\boldsymbol{xs}$ *is the position of the maximum value of the Schottky hump* 28
Figure 16: Schematic diagram of a local electrode atom probe (LEAP) with a crossed delay line single atom detector at the end of the time-of-flight mass spectrometer. Both voltage and laser pulsing modes of field evaporation are shown. 29
Figure 17 HP density results showing the relative density of each HP time and pressure 31
Figure 18 Electrical conductivity at RT on dependence of the pressure utilized on the specimen, correlated with 32
Figure 19 XRD diffraction of 0 at. % Bi and 0.2 at. % Bi corresponding with the rock-salt PbTe crystal structure (JCPDS number 04-002-0317). 33
Figure 20 a FIB Ion image of Bi free sample AQ, using TLD detector. the dark background is the matrix while the bright needles are the precipitates. 34
Figure 21 a FIB Ion image of Bi free sample 6h, using TLD detector. the dark background is the matrix while the bright needles are the precipitates 34
Figure 22 FIB Ion image of Bi free sample 48h, using TLD detector. the dark background is the matrix while the bright needles are the precipitates 35
Figure 23 HRSEM image of 0.2 at. % Bi AQ, using BSE detector. the grey background is the matrix while the precipitates are the dark dots. 35
Figure 24 HRSEM image of 0.2 at. % Bi 6h, using BSE detector. the grey background is the matrix while the precipitates are the dark dots. 36
Figure 25 HRSEM image of 0.2 at. % Bi 48h, using BSE detector. the grey background is the matrix while the precipitates are the dark dots. 36
Figure 26 HRSEM image of 0.4 at. % Bi AQ, using BSE detector, orientation contrast. the grey background is the matrix while the precipitates are the dark dots 36
Figure 27 HRSEM image of 0.4 at. % Bi 6h, using SE detector after FIB etching, orientation contrast. the dark background is the matrix while the bright needles are the precipitates 37

Figure 28 HRSEM image of 0.4 at. % Bi 48h, using SE detector after FIB etching, orientation contrast. the dark background is the matrix while the bright needles are the precipitates *37*
Figure 29 EDS measurments for the matrix on the left and the precipitate on the right.***Error! Bookmark not defined.***
Figure 30 Nv is given for the different aging times and Bi concentrations *38*
Figure 31 The temperature dependence of the heat capacity values as measured for the 0.2 at. % Bi samples for the Bi free series of specimens aged at 380 °C for 0 , 6 , and 48 hours *40*
Figure 32 The temperature dependence of the heat capacity values as measured for the Bi free samples, for the Bi free series of specimens aged at 380 °C for 0 , 6 , and 48 hours *40*
Figure 33 The temperature dependence of the heat capacity values as measured for the 0.4 at. % Bi samples for the Bi free series of specimens aged at 380 °C for 0 , 6 , and 48 hours *40*
Figure 34 Thermal conductivity for differenet aging times ;(a) is for the Bi free samples, (b) is for the 0.2 at% Bi and (c) is for the 0.4 at.% Bi *43*
Figure 35 Comparison between the lattice component of the thermal conductivity (circle) and the electric component (square) for the Bi-free sample (above) and 0.4 at.% Bi below *44*
Figure 36 temperature dependence of thermal conductivity for differenet Bi concentrations for a certain aging time ;(a) is for the AQ samples, (b) is for the 6h aging time and (c) is for 48h aging times *45*
Figure 37 Electrical conductvity for different samples; (a) Bi-free samples;(b) 0.2 at% Bi and (c) 0.4 at.% Bi samples *46*
Figure 38 temperature dependence of the Seebeck coefficient for different samples; (a) Bi-free samples;(b)close up of the marked area for the Bi free sample (c) 0.2 at% Bi and (d) 0.4 at.% Bi samples *46*
Figure 39 TEM micrograph of 0.4 at% Bi 48h in DF , the matrix (PbTe) is gray and the precipitates have dark contrast *48*
*Figure 40 Diffraction pattern of the precipitate and matrix the red marks represent the precipitate and black the matrix the orientation relationship is OR: PbTe*100011||100010 *Ag2Temonoclinic Z.A: [011]* ..... ***Error! Bookmark not defined.***
Figure 41 TEM micrograph of 0 at. % BI AQ, for Z.A of [011] *48*
Figure 42 HRSTEM micrograph in high annular angle dark field (HAADF) contrast of 0 at % Bi 48h showing precipitates in dark contrast with two different sizes, big precipitate with diameter of 45 nm and smaller ones with size of 10-20 nm. *49*
Figure 43 HRSTEM micrograph in high angle annular dark field (HAADF) contrast of 0 at % Bi 48h showing precipitates in dark contrast with two different sizes, big precipitate with the size of a couple of microns and smaller ones with size of 10-20 nm. *49*
Figure 44 Area of the eds from the 0 at.%Bi 48h on the left ,on the middle the EDS of the precipitates, the measurments ranges between 0 to 2 where the number indicates the content of silver (Ag_xTe), at last on the right the PB-Te ratio is presented *50*

Figure 45 Area of the eds from the 0.4 at.%Bi 48h on the left ,on the middle the EDS of the precipitates, the measurments ranges between 0 to 2 where the number indicates the content of silver (Ag_xTe), at last on the right the PB-Te ratio is presented 51
Figure 46 SEM image of the tip used for APT, sample 0 at.% Bi 6h 52
Figure 47w Mass spectrum ranges of Pb Te and Ag taken using APT for Bi free sample 53
Figure 48 close up of the mass spectroscopy for area that shows the overlap between the Pb and Bi peaks 53
Figure 49 APT reconstruction of 0. at % Bi 48 hr for different iso-concentration surfaces ranging from 0 at. % Ag to 8 at. % Ag 54
Figure 51 HRTEM micrograph (a) and APT reconstrucion (b) of 0 at. % Bi 48 hr, the large precipitate is marked with blue and the small precipitates are marked with red, after matching the isoconcentration surface of the reconstruction to the micrograph , were we able to calculate the Nv. in this figure the Ag % iso-concetration is 2 at. % AgHRTEM micrograph (a) and APT reconstrucion (b) of 0 at. % Bi 48 hr, the large precipitate is marked with blue and the small precipitates are marked with red, after matching the isoconcentration surface of the reconstruction to the micrograph , were we able to calculate the Nv. in this figure the Ag % iso-concetration is 2 at. % Ag 55
*Figure 52 APT reconstruction of the samples a) AQ sample with a box of 988x160x160 [nm3] the precipitates are highlighted by an iso-concentration surface of 2.45 at% Ag b) 6h aging with sample box of 758x187x182[nm2] with iso-concentration of 2.3 at% Ag and 36 M ions Ag c) 48h sample with a box of 975x215*214 [nm3] with iso-concentration of 2 at% Ag with 289M ions* 56
Figure 53 Proxigram taken from a nano-precipitate showing that it's chemical stoichiometry is Ag:Te ..... ***Error! Bookmark not defined.***
Figure 54 APT reconstruction close up for 0 at. % Bi 48h 58
Figure 54 Nv vs aging time for specimen 0 at.% Bi (red) and 0.2 at.% Bi (blue) using the APT data ... 58
Figure 56 Thermal conductivity for differenet aging times at 370°C for the Bi-free sample 60
Figure 57 Thermal conductivity for different aging times at 370oC for the 0.2 at.% Bi sample 60
Figure 58 Seebeck coefficient of the Bi free sample at different aging times for 370°C (right), Electrical conductivity on the left 60
Figure 59 Seebeck coefficient of the 0.2 at. % Bi sample at different aging times for 370oC (right), Electrical conductivity on the left 61
Figure 60 SEM and FIB micrographs of the samples, marked by the table, precipitates have dark contrast for SEM images and bright contrast for the FIB images6 µm 62
Figure 61 SEM and FIB micrographs of the samples, marked by the table, precipitates have dark contrast for SEM images and bright contrast for the FIB images 62
Figure 61 N_V of the samples for the 370°C annealing temperature 62
*Figure 63 The temperature dependent lattice thermal conductivity values evaluated from the measured thermal and electrical conductivities applying the Wiedmann-Franz relationship for HP seires of specimens. of specimens aged at 380 °C for 0 (diamonds), 6 (squares), and 48 h (stars), forthe (**a**) Bi-free (blue symbols) and **b**) Bi-alloyed (red symbols* 64

List of Tabels

Table 1 - PbTe properties 16

Table 2 Nv (m^{-3}) of precipitates for different Bi concentrations and annealing times 39

Table3 Density of the specimens 43

Table 4 Matrix concentration at different aging times of 0 at.% Bi 59

List of abbreviations	
Atom probe tomography	APT
Backscattered electrons	BSE
Hot press	HP
High resolution scanning electron microscopy	HRSEM
High resolution transmission electron microscopy	HRTEM
Laser flash analysis	LFA
Mean free path	M.F.P
Power factor	PF
Proximity histogram	Proxigram
Room temperature	RT
Seebeck analyzer	SBA
Scanning electron microscopy	SEM
Secondary electrons	SE
Transmission electron microscopy	TEM
Thermoelectric	TE

Thermoelectric generator	TEG
List of symbols	
Absolute temperature	T
Charge carrier mobility	μ
Debye temperature	θ_D
Electron charge	E
Electrical conductivity	σ
Electronic thermal conductivity	κ_e
Fermi energy	E_f
Gibbs free energy	G
Heat	Q
Lattice thermal conductivity	κ_l
Mean atomic weight	M_W
Material's bulk density	ρ
Material figure of merit	ZT
Mean free path	λ
Melting point	T_m
Peltier coefficient	Π
Phonon relaxation time corresponding to boundaries	τ_{GB}
Precipitate number density	N_v
Relaxation time	τ
Relaxation time corresponding to dislocations	τ_D
Relaxation time due to normal phonon-phonon scattering	τ_N
Relaxation time corresponding to precipitates	τ_G
Relaxation time corresponding to strains	τ_s
Relaxation time corresponding to Umklapp processes	τ_U
Seebeck coeffiecient	S
Sound velocity	ν_s
Specific heat at constant Pressure	C_P
Specific heat at constant volume	C_V
Thermal conductivity	κ ,TC
Thermal diffusivity	D
Thermo-power	α

The time at 50% of the temperature increase	$t_{0.5}$
Voltage	V
List of constants	
Avogadro's number	N_A
Boltzmann constant	k_B
Grüneisen parameter	γ
Lorenz number	L_0
Planck constant	h
Planck constant - reduced	$\hbar$

1 ABSTRACT

Conversion of waste heat into electrical power is performed using thermoelectric (TE) generators, which are based on the Seebeck effect. PbTe is considered one of the best compounds for TEGs operating at mid-temperature ranges owing to its high figure of merit, ZT, which denotes the thermodynamic conversion efficiency and can be improved by increasing electrical conductivity and the Seebeck coefficient while reducing thermal conductivity. A common way to improve TE properties is alloying with selected elements above their solubility limits to initiate the formation of second-phase precipitates, which reduce lattice thermal conductivity due to phonon scattering. Our approach is to enhance the TE performance of PbTe by co-doping with Ag (3.3 at. %) and Bi (0, 0.2, or 0.4 at. %), where Ag-atoms serve as Ag_2Te-precipitate forming agents and Bi atoms act as electron donors. We track the microstructure evolution of both alloys for different aging times at 380 °C and investigate its effects on TE transport coefficients.

Materials synthesis includes vacuum melting and homogenization, followed by grinding and hot pressing. Thermal conductivity is measured using laser flash analysis (LFA), and electronic transport coefficients are measured employing a dedicated four-point probe system equipped with micro-heating segments. We find that the thermal conductivity of the Bi-free samples decreases upon aging for 6 h, but increases for aging times as long as 48 h. Interestingly, electrical conductivity values decrease monotonously upon aging times. The key parameters determining these transport coefficients are the Ag_2Te precipitate number density (N_v) and the matrix concentration. To elucidate these findings, we employ basic and advanced characterization techniques including scanning electron microscopy (SEM) as well as complementary transmission electron microscopy (TEM) and atom probe tomography (APT). Application of complementary TEM and APT enables us to perform a quantitative evaluation of the Ag isoconcentration surfaces surrounding the Ag_2Te precipitates, which are critical for determining N_v.

APT analysis yields N_v-values as high as 10^{24} m^{-3} together with an accurate evaluation of the Ag concentration in the inter-precipitate space (< 1.0 at. %). We account for the aging time-dependent transport coefficients in terms of interplay between the degree of PbTe-matrix super-saturation and the spatial distribution of the Ag_2Te-precipitates.

This unique combination of experimental tools enables us, for the first time, to track the microstructure evolution of PbTe-based compounds and understand the implications for TE transport properties.

2 INTRODUCTION

The emerging global need for energy production, conservation, and management has intensified interest in more effective renewable sources, including solar, wind, biomass, and others. Another potential source of renewable power is electricity from heat sources using thermoelectric (TE) materials. TE modules are solid-state devices that directly convert thermal energy into electrical energy. This process is based on the "Seebeck effect", which is the appearance of electrical voltage caused by a temperature gradient across a material.

The application of TE devices in daily life strongly depends on their thermodynamic conversion efficiency, which is determined by the TE figure of merit (ZT). Better TE performance, which means an increased ZT, is manifested in a large Seebeck coefficient, high electrical conductivity, and low thermal conductivity. These three requirements are usually contradictory, which makes the development of TE materials a grand challenge from the point of view of material science. Furthermore, these properties are highly sensitive to the finest features of microstructure.

The lead-telluride (PbTe) compound offers many advantages, among them a high melting point (1190 K) and good structural and chemical stability. PbTe-based compounds have been the primary thermoelectric material for midrange temperature (600-800 K) applications. They crystallize in the NaCl crystal structure with Pb atoms occupying the cation, and Te atoms forming the anion sublattice sites. The maximum ZT values for PbTe have been reported to range between 0.8 and 1.0 at $T \approx 650$ K.

The present study focuses on the Pb-Te-Ag system, which has the potential of forming Ag_2Te precipitates dispersed in a PbTe-based solid solution. The Ag_2Te precipitates are expected to serve as phonon-scattering centers, thereby reducing lattice thermal conductivity and increasing its ZT value. To achieve a significant decrease of thermal conductivity, κ, we must attain values of precipitate number densities, N_v, as high as 10^{20} m^{-3}.

We prepare ternary $(PbTe)_{1-x}(Ag_2Te)_x$ alloys with x=0.032 and dope them with either 0, 0.2, or 0.4 at. % Bi, applying vacuum melting and hot-pressing. We perform homogenization and aging heat treatments at 380 and 370 °C for durations of up to 48 h to control nucleation and growth of the Ag_2Te phase. We analyze the precipitates' number density (N_v), employing high-resolution scanning electron microscopy (HRSEM).

We find that the Ag_2Te precipitates undergo nucleation and growth followed by coarsening, which is manifested in a non-monotonous variation of the number density. We determine the materials' electrical properties and thermal conductivities, which indicate significant changes associated with microstructure evolution. Advanced characterization combining transmission electron microscopy (TEM) and atom probe tomography (APT) allows us to delineate the direct relationship between the microstructure and its thermal evolution with the TE transport properties. Finally, we discuss the interplay between precipitation and the solid-solution degree of supersaturation, and how it affects thermal conductivity and electrical properties.

The present research is based on a previous M.Sc. study conducted by Mr. Tom Grossfeld at the Thermoelectric Materials Research Group, Technion.

3 LITERATURE REVIEW

3.1 The thermoelectric effect: The history

Between 1821-1823, Thomas Johann Seebeck found that a circuit made from two dissimilar metals, with junctions at different temperatures, deflects a compass magnet. Seebeck initially believed this was due to magnetism induced by the temperature difference and thought it might be related to the earth's magnetic field. However, it was quickly realized that a "Thermoelectric Force" induced an electrical current, which by Ampere's law deflects the magnet. [1] More specifically, the temperature difference produces an electric potential (voltage) that can drive an electric current in a closed circuit. Today, this is known as the Seebeck effect. Later, other similar effects were found, such as the Peltier effect (production of heat flux by electric current, 1834) and the Thomson effect (heating or cooling of a current-carrying conductor with a temperature gradient, 1851). Since temperature gradients are essential for thermoelectricity, the basic requirements for thermoelectric materials are that they conduct electricity but do not conduct heat significantly.

It was only in 1909 that the engineer Edmund Altenkirch mathematically expressed the relationship between the physical properties of TE materials and the efficiency of a simplified thermopile or Thermoelectric Generator (TEG).[2] Altenkirch's equation includes, among other parameters and variables, the electromotive force and the thermal and electrical resistance/conductivity of a thermopile. Later, in 1949-1956, the famous Russian scientist Abram F. Ioffe integrated these parameters into the Z parameter and used it to express the efficiency of thermoelectric (TE) devices. The total efficiency increases monotonously with ZT and approaches the Carnot limit, which is the maximum value allowed by the 2nd law of thermodynamics, as given by Ioffe's parameter: [3]

(1) $$ZT = T\frac{S^2\sigma}{\kappa}$$

where T is the absolute temperature, Z is proportional to the electrical conductivity, σ and the Seebeck coefficient (S), and is inversely proportional to the thermal conductivity, κ.

The parameter ZT is considered the most important characteristic of TE materials, from an engineering point of view. It is known as the "Thermoelectric Figure of Merit", and it is accepted that this parameter correctly expresses the capacity of TEs for the generation of cold as well as for the direct conversion of heat into electricity. The parameter Z serves to facilitate the evaluation of TE performance and makes the comparison of TE materials easier. TE performance is often expressed in scientific papers as the product of z by temperature T. Notably, the product ZT is a dimensionless quantity of the TE performance, and it should be emphasized that the properties S, κ, σ of materials depend on the temperature T of every given material. Consequently, the figure of merit is not a number, but a function of the temperature. Generally, the value of T in the product ZT corresponds to the maximum temperature of the TE operation. Thus, the product ZT is the maximum value of the performance of the material. This value varies from one material to another.[4] In addition, thermal and electrical conductivities are related to the Wiedemann-Franz rule, which results in an increase of thermal conductivity with increasing electrical conductivity.

During the 1930's, thermoelectric research went through a resurgence of interest with the discovery of semiconducting materials, in which Seebeck coefficients greater than $100\frac{\mu V}{K}$ were obtained. Since then, many new approaches have been proposed. Thus, following progress in solid-state physics, the first thermoelectric generators (TEGs) were based on electricity conductors and semiconductors, such as antimony, bismuth, copper, iron, lead, zinc, and different alloys, among others.[5]

Even though there are some TE materials with a high figure of merit, they are not used for electric power generation, as the results of numerous experimental investigations have shown that the performance of

TE materials is not only dependent on chemical composition but also on microstructure and nanostructure, which is determined in its material processing, especially sintering. Based on these results, many researchers focus their efforts on the development of TE materials with sophisticated microstructures.

The most common TE materials are bismuth telluride (Bi_2Te_3), lead telluride $(PbTe)$, and silicone germanium $(SiGe)$. Over the last decades, significant improvements have been made in developing highly efficient materials.

3.2 The thermoelectric effect: Physical background

The thermoelectric effect occurs due to the fact that charge carriers in metals and semiconductors can carry both heat and charge. When there is a thermal gradient in a material, the charge carriers at the hot side of the material diffuse to the cold side. This transport results in an accumulation of charge carriers and produces a net charge at the cold side of the material, creating an electrostatic potential, or voltage, which is referred to as the Seebeck effect and is the basis for thermoelectric power generation.

3.2.1 The Seebeck effect

The ratio of the voltage to temperature difference is an intrinsic property of a material, defined as the Seebeck coefficient or thermo-power.

(2)
$$\alpha = \frac{\Delta V}{\Delta T}$$

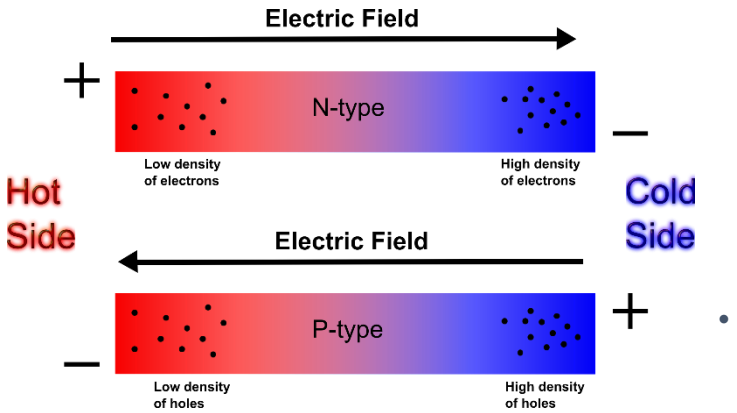

Figure 1 An illustration of the Seebeck effect for an N-type semiconductor (above) and P-type semiconductor (below)

Another way of defining the Seebeck coefficient is entropy transport per charge carrier divided by the charge. The Seebeck coefficient can be presented as an integral of one-electron energy states over conductivity:

(3) $$S = -\frac{k_B}{e}\int\left(\frac{E-E_f}{k_BT}\right)\frac{\sigma(E)}{\sigma}dE$$

Where k_B is Boltzmann's constant, e is the electron charge, and σ is the conductivity.

The charge carrier type (N-type or P-type) is defined by the sign of the Seebeck coefficient. A positive Seebeck coefficient indicates a P-type where the concentration of the carriers has a hole majority, and a negative one implies an N-type or electron majority.

If we look at the charge carrier concentration (for example of the electrons):

(4) $$n = N_c \exp\left(\frac{E-E_f}{k_BT}\right)$$

we can observe that while the Seebeck coefficient rises as the difference of the valance band with the Fermi level, the concentration of electrons decreases and so does the electric conductivity, accordingly. There is a contradiction between both attributes and thus fine-tuning is needed to find the best configuration.

3.2.2 The Peltier effect

If an electric current is sent through a material, the charge carriers will transport heat in the direction of the electric current, resulting in heating at one end and cooling at the other end of the material. This is, in fact, the opposite effect to the Seebeck effect. When a current is passed between two dissimilar materials, heat is either released or absorbed at this junction, depending on the differences between the Fermi energies of the two materials. If current flows from a material with a higher Fermi energy to a material with a lower one, then heat is pumped out, and vice-versa. The rate at which the Peltier heat (Π) is liberated or rejected at the junction of two materials is given by[7]:

(5) $$\dot{Q} = \Pi I$$

3.2.3 The Thomson effect

Lord Kelvin (Thomson) predicted the cooling or heating of a homogeneous conductor, resulting from the flow of electrical current with the presence of a temperature difference. This is known as the Thomson effect, which is a continuous version of the Peltier effect, when there is a gradient in the Seebeck coefficient

and a current is going through this gradient. The Thomson relation shows the relations between the Seebeck and Peltier coefficients:[8]

(6) $$\Pi = \left(S_2 - S_1\right)T$$

3.2.4 Thermoelectric efficiency

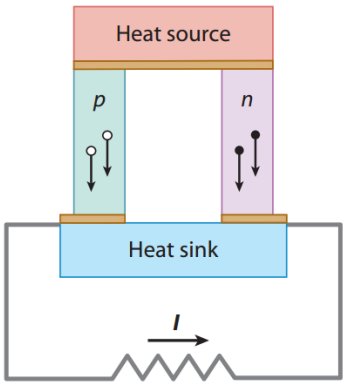

Figure 2 A schematic illustration of a typical TE generator with p-type and n-type legs connected thermally in parallel and electrically, in series and with a load resistor.

Figure 2 shows a typical p-n TE segment in generation mode. A thermodynamic analysis of the hot junction yields:

(7) $$Q_H = Q_{H,p} + Q_{H,n} = \left(\kappa_p \frac{A_p}{L_p} + \kappa_n \frac{A_n}{L_n}\right)\left(T_H - T_C\right) + \left(\alpha_p - \alpha_n\right)T_H I - \frac{I^2}{2}\left(\rho_p \frac{L_p}{A_p} + \rho_n \frac{L_n}{A_n}\right)$$

Where $Q_{H,p/n}$ is the heat transferred by conduction from the hot side of the p-n TE segment to the cold side. $Q_{C,p/n}$; $A_{n/p}, L_{n/p}$ are the cross-section areas and lengths of the p-type or n-type legs respectively. $\alpha_{p/n}.\kappa_{p/n}$ and $\rho_{p/n}$ are the thermo-power, thermal conductivities, and electrical resistivities of the p- or n-legs, respectively. T_H, and T_C are the hot- and cold-side temperatures, respectively, and *I* is the electrical current passing through the legs.

Equation (7) consists of three parts, which comprise the heat balance in the device. The first part refers to heat loss via conductivity, the second is associated with Peltier heating, and the latter part is due to Joule heating. The Peltier term incorporates T_H as this is the temperature in which the heat evolves. Only half of the Joule heat travels towards the hot side, thus we have half in the Joule terms.

3.3 Electrical conductivity

The electrical conductivity is proportional to the number density of electrons n, and the charge carrier mobility μ:[9]

(8) $$\sigma = ne\mu$$

Electrical conductivity has a major role in maximizing the figure of merit ZT, as shown in Eq. (1). This extremum usually occurs when carrier concentration is between 10^{19} and 10^{21} cm^{-3} (varies for different materials), which falls between those of metals and semiconductors. This corresponds to charge carrier concentrations that are heavily doped.[8]

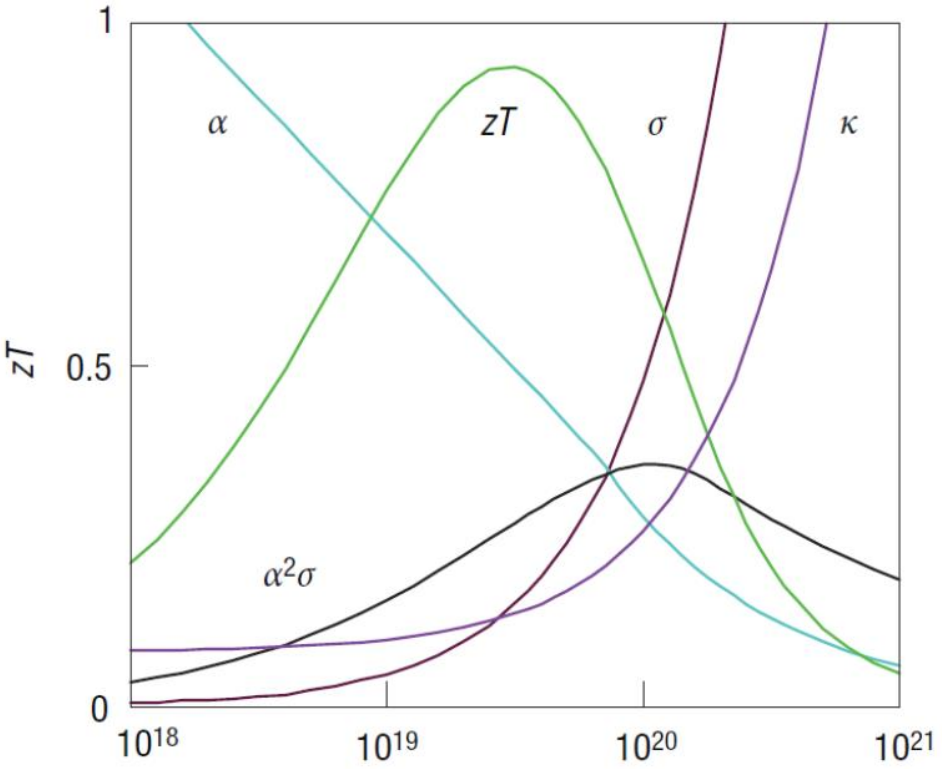

Figure 3 The balance between thermal conductivity, the Seebeck coefficient, and electrical conductivity in order to obtain the highest possible ZT values. The thermoelectric power factor peaks at higher carrier concentrations than ZT. The difference between the peaks of the power factor and ZT is greater for the newer lower-k_l materials. These trends were modelled using data from Bi_2Te_3[8]

3.4 Thermal conductivity

The rate of heat transfer in a materials depends upon the temperature gradient and the thermal conductivity of the material. Non-metallic solids transfer heat by lattice vibrations, mainly as the energy propagates through. Such heat transfers are described using phonons or lattice vibrations. Metals are much better thermal conductors than non-metallic materials because the same mobile electrons that participate in electrical conduction also take part in the transfer of heat.

The relationship between the heat transferred per unit of time and the temperature gradient through a cross-section area is defined as thermal conductivity:

(9) $$\frac{dQ}{dt} = \dot{Q} = -\kappa A \frac{T_2 - T_1}{\Delta x}; \dot{q} = -\kappa \frac{T_2 - T_1}{\Delta x}$$

Thermal conductivity is a material-specific property used for characterizing steady heat transport. It can be calculated using the following equation:

(10) $$\kappa = D(T)\rho(T)C_p(T)\ ,$$

where D represents the thermal diffusivity, ρ is the density, and C_p is the specific heat. Thermal conductivity consists of contributions from the electrons and phonons, as follows:

(11) $$\kappa = \kappa_e + \kappa_l$$

Metallic materials exhibit relatively high thermal conductivity, which is associated with the contribution of electrons. At a given temperature, their thermal conductivity is proportional to the electrical conductivity, which is defined as the Wiedemann-Franz rule:[1,10]

(12) $$\kappa_e = L_0 \sigma T = ne\mu L_0 T\ ,$$

The constant of proportionality L_0 is the Lorenz number for free electrons[11],

(13) $$L = 1.5 + \exp\left(-\frac{|S|}{116}\right) \approx 2.45x10^{-8}\left(\frac{J^2}{K^2C^2}\right) or \left(\frac{W\Omega}{K^2}\right)$$

The relationship in eq. 12 is based on the fact that the heat and electrical transport both involve the free electrons in the metal.

3.4.1 The lattice component of thermal conductivity

In addition to the thermal conduction in metals from free electrons, there is also heat transport by the lattice, which occurs as free electrons interact with the lattice waves and limit the phonon mean free path. Lattice conductivity is usually much smaller than normal thermal conductivity, although in some cases it is possible to have a relevant lattice component[12].

Using the heat equation and the equipartition theorem, classical kinetic theory provides a good approximation for lattice thermal conductivity:[13,14]

(14) $$\kappa_l = C_V \nu_s \lambda$$

C_v is the specific heat at constant volume, λ is the phonon mean free path (MFP), and v_s is the average velocity of sound in the material. At very low temperatures, the dominant part is ruled by the Debye law for C_v. Phonon scattering is insignificant in this temperature range, because of the low number of excited phonons and their very long wavelengths. However, for temperatures above the Debye temperature, the lattice component depends mainly on phonon-to-phonon scattering. For such cases, lattice thermal conductivity can be described by Keyes' expression:[15]

(15) $$\kappa_l T = \frac{\left(k_B T_m\right)^{3/2} \rho^{2/3}}{3\gamma^2 \varepsilon^3} \left(\frac{N_A}{M_W}\right)^{7/6}$$

where T_m is the melting point, M_W is the mean atomic weight, γ is the Grüneisen parameter, ε is the fractional amplitude of interatomic thermal vibration, k_B is the Boltzmann constant, N_A is Avogadro's number, and ρ is the bulk density.

This equation provides several useful insights into thermal conductivity:

- In the high temperature range, κ_l is proportional to $\frac{1}{T}$.
- A low melting point can lead to low thermal conductivity.
- κ_l decreases with the increase in atomic mass.
- The proportionality to $\rho^{2/3}$ makes κ_l low for crystals with large interatomic distances of soft interatomic bonds.

3.4.2 The Callaway model for thermal conductivity

To evaluate the phonon scattering mechanisms of the precipitates in PbTe-based materials in more detail, theoretical calculations of the lattice thermal conductivity using a theory of relaxation can be performed, such as the model developed by Callaway.[16,17] This model describes the dependence of lattice thermal conductivity on temperature, for different phonon scattering mechanisms.

(16) $$\kappa_l = \frac{k_B}{2\pi^2 \nu} \left(\frac{k_B T}{\hbar}\right) \int_{0.}^{\theta_D/T} \tau_c(x) \frac{x^4 e^x}{\left(e^x - 1\right)^2} dx$$

It considers the conservation of the total wave vector of the phonon system by both normal and Umpklapp processes:[18]

$$\kappa_l = \frac{k_B}{2\pi^2 v}\left(\frac{k_B T}{\hbar}\right)^3 \left\{ \int_0^{\theta_D/T} \tau_c(x) \frac{x^4 e^x}{\left(e^x - 1\right)^2} dx + \frac{\left(\int_0^{\theta_D/T} \frac{\tau_c(x)}{\tau_N(x)} \frac{x^4 e^x}{\left(e^x - 1\right)^2} dx \right)^2}{\int_0^{\theta_D/T} \frac{1}{\tau_N(x)} \left(1 - \frac{\tau_c(x)}{\tau_N(x)}\right) \frac{x^4 e^x}{\left(e^x - 1\right)^2} dx} \right\}; x = \frac{\hbar\omega}{k_B T}\tau_C \quad \textbf{(17)}$$

where $\hbar$ is the reduced Plank constant, T is the absolute temperature, and x is the combined relaxation time. The latter is obtained by averaging the relaxation times from various processes. For temperatures above θ_D (Debye temperature) all the phonon modes have the same energy as $k_B T$ at the high-temperature limit, so the probability that a phonon will suffer a collision is directly proportional to the number of other phonons present.

The equivalent relaxation time incorporates the effects of scattering from strain, nanoscale precipitates, dislocations, internal boundaries, and phonon-phonon interactions:

$$\kappa_l = CT^3 \int_0^{\theta_D/T} \tau_C(x) J(x) dx \quad \textbf{(18)}$$

For cases where both normal and U-processes are dominant, eq. 18 can be corrected by the addition of the term.

$$\tau_c^{-1} = \tau_U^{-1} + \tau_N^{-1} + \tau_B^{-1} + \tau_p^{-1} + \tau_0^{-1} \quad \textbf{(19)}$$

where $\tau_U^{-1}, \tau_N^{-1}, \tau_B^{-1}, \tau_p^{-1}, \tau_0^{-1}$ are the relaxation times corresponding to scattering from Umklapp processes, normal processes, boundaries, precipitates, and scattering from other defects, respectively.

From the second-order perturbation theory, the relaxation time for Umklapp scattering, caused by inelastic phonon-phonon interactions, is given by:[12,19]

$$\tau_U^{-1} \approx \frac{\hbar\gamma^2}{M_W v^2 \theta_D} \omega^2 T e^{\left(-\frac{\theta_D}{3T}\right)} \quad \textbf{(20)}$$

where M_W is the average mass of an atom in the crystal. The relaxation time due to momentum-conserving processes in normal phonon-phonon scattering, τ_N, is modeled by several studies. The following expression is a conventional one[1]

(21) $$\tau_N^{-1} \approx \omega^2 T^3$$

Particles/precipitates have an important role in phonon scattering, thus reducing lattice thermal conductivity. Today it is clear that the mere presence of nano-structuring in a semiconductor is not enough to increase phonon scattering. To scatter phonons effectively, we prefer nanometer-sized precipitates having large mass contrast with respect to their environs, which exert long-range elastic strain fields. The phonon relaxation time is described by:[20]

(22) $$\tau_p^{-1} \approx N_v \nu_s \left[\frac{1}{2\pi R^2} + \frac{9}{4\pi R^2} \left(1 - \frac{\rho}{\rho_m} \right)^{-2} \left(\frac{\omega R}{\nu_s} \right)^{-4} \right]^{-1}$$

where N_v is the number density of the particles, ν_s is the sound velocity, R is the radius of the precipitate (assuming it is spherical), ρ is the precipitate density, and ρ_m is the matrix density.

In this study we do not consider the precipitate morphology but the N_v only. When the number density values reach as high as 10^{20}, thermal conductivity starts to decrease. This is shown in the graph below:[20]

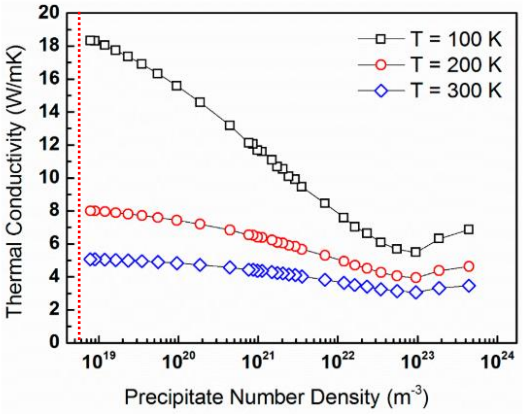

Figure 4 The calculated relative thermal conductivity vs precipitate number density, for 100, 200, and 300K. TC shows a signifacant reduction when reaching number density of 10^{20} and above.[20]

3.5 A review of thermoelectric materials

In general, TE materials require a balance between high electrical conductivity (EC) and S on one hand, and low TC on the other; however, these properties contradict one another. We can divide most materials to metals, insulators, and semiconductors. Metals have high EC, but also high TC, thus they make for poor TE materials. Insulators have very low TC but of course have close to 0 EC. Thus, TE materials should be semi-conductors, with a rather low band gap. To enhance their efficiency, one can modify the thermal conductivity while leaving the electrical properties almost unchanged.[21]

The family of IV-VI[21] chalcogenides, such as PbSe, PbS, PbTe, GeSe, GeS, GeTe, $SnSe_2$, SnS_2 and their alloys are promising TE materials for TEGs and have been widely studied.[21,22] The temperature dependent ZT-values of common chalcogenide TE materials is presented in Figure 6:

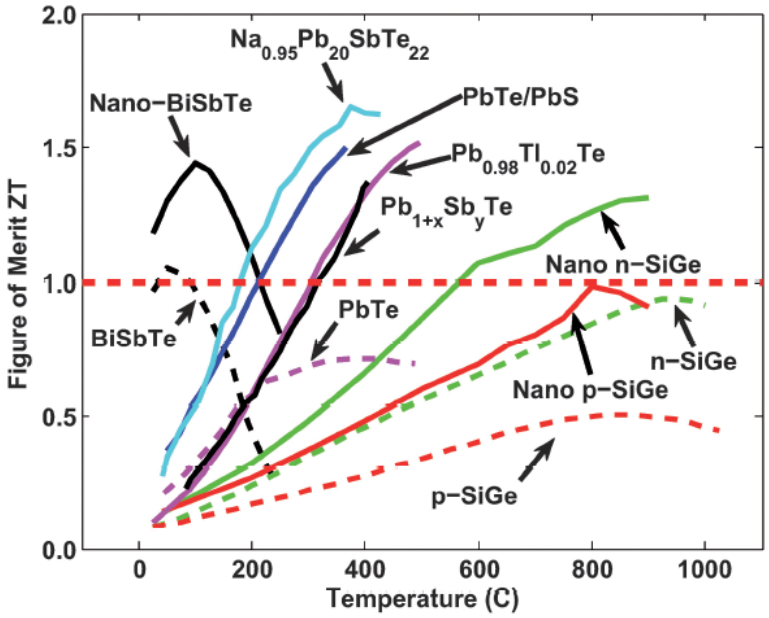

Figure 5 Figure of merit ZT of current state of the art thermoelectric materials versus temperature. The dashed lines show the maximum ZT values for bulk state of the art materials, and the solid lines show recently reported ZT values, many of which were obtained in bulk nanostructured materials.[22]

The high-charge carrier concentration allows for good electrical conductivity, and TE properties can be optimized by varying the carrier concentration. Alloying disrupts the transport of phonons (quantized lattice vibrations which carry heat), resulting in a reduced thermal conductivity. Lattice thermal conductivity can be further reduced by using heavy elements with low sound velocities, such as Bi, Te, and Pb. Examples of commercial thermoelectric materials are Bi_2Te_3 and alloys such as $Bi_xSb_{2-x}Te_3$ at room temperature; PbTe and alloys such as PbTe–PbSe at moderate temperature; and the alloy $Si_{80}Ge_{20}$ at high temperature. Despite having multiple parameters to adjust, optimizing all the parameters together is quite difficult because the properties are interdependent. For example, if we found that the electrical conductivity is too low, we would want to increase the carrier concentration. However, though increasing the carrier concentration would result in better

electrical conductivity, it would also reduce the Seebeck coefficient and increase the electronic contribution to the thermal conductivity.

Eq. (1) implies that these changes in properties will most likely not lead to a net increase in ZT, since any favorable change in one property is accompanied by an unfavorable change in the others. These conflicting trends are illustrated in Fig. 7:[22]

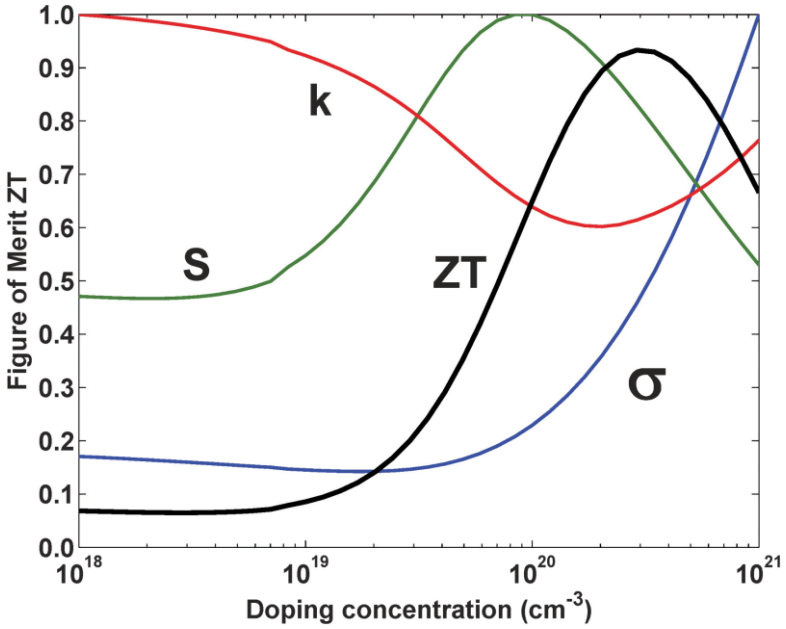

Figure 6 Normalized thermoelectric properties and ZT versus doping concentration at 300 K for n-type $Si_{80}Ge_{20}$. Curves are calculated from a numerical model developed by the authors. k refers to thermal conductivity, S refers to the Seebeck coefficient, and σ refers to electrical conductivity[22].

3.6 PbTe-based compounds

3.6.1 Single-phase PbTe

The lead telluride compound, PbTe, is a mid-temperature range (600–800 K) thermoelectric material. Its maximum operating temperature is 900 K[23]. PbTe has a relatively high melting point (1190 K). The binary phase diagram of Pb and Te is presented in Figure 7.

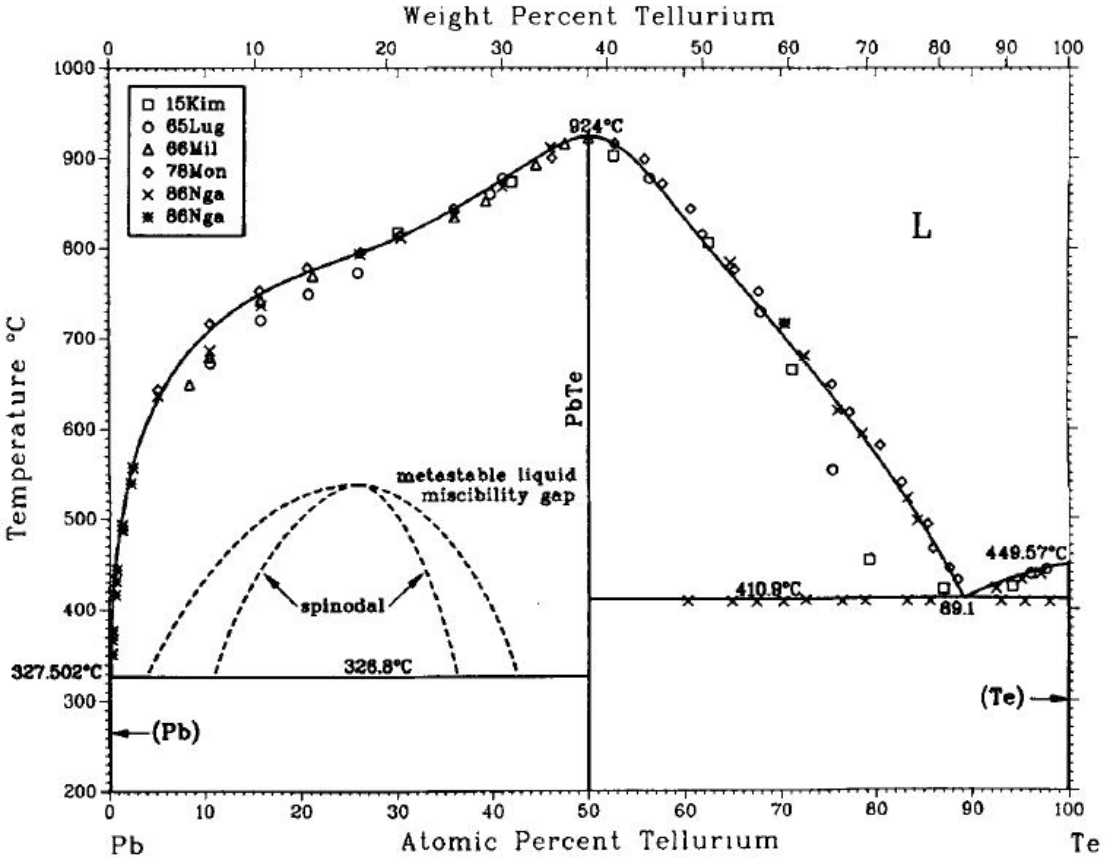

Figure 7 Phase diagram of a binary Pb–Te system.[24]

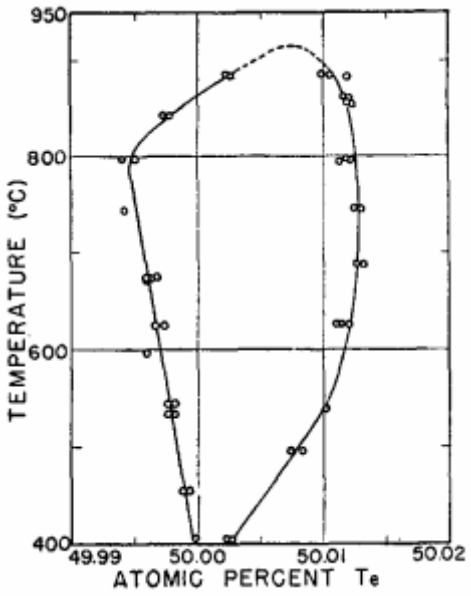

Figure 8 Close-up chart of the PbTe phase diagram around the 50 at% concentration, showing a stable area at the temperatures in which we are doing the synthesis of our material

PbTe will serve as the matrix in our research. It crystallizes in the NaCl crystal structure, with Pb atoms occupying the cation and Te forming the anionic lattice. The band gap is approximately 0.32 eV, which is optimized for power generation applications and can be doped as either n-type or p-type with appropriate dopants or anti-site defects (Pb-rich PbTe is n-type, while Te rich PbTe is p-type). The maximum ZT values of undoped PbTe[25] have been reported to range from 0.8 to 1.0 at ≈ 650 K, and the TE properties of PbTe have been thoroughly investigated. The lattice thermal conductivity of PbTe is around 2.2 $Wm^{-1}K^{-1}$ at room temperature and decreases with a $1/T$ dependence as temperature increases. Doping is necessary to obtain Seebeck coefficients above $200 \mu V K^{-1}$. The following table displays some of the relevant physical properties of PbTe:[21]

Table 1 - PbTe properties [20]

Lattice constant	a Å	**6.454**
Density	$\rho \frac{g}{cm^3}$	**8.24**
Grüneisen parameter	γ	**1.96**
Longitudinal sound velocity	$v_L \frac{m}{s}$	**3596**
Transverse sound velocity	$v_S \frac{m}{s}$	**1610**
Average sound velocity	$v_A \frac{m}{s}$	**1770**
Young's modulus	E GPa	**27.7**
Debye temperature	$\theta_D K$	**136**

Charge carrier concentration	$n\ \frac{10^{18}}{cm^3}$	**2.6**
Charge carrier mobility	$\mu\ \frac{cm^2}{V \cdot s}$	**383**
$\frac{\kappa_l}{\kappa_{tot}}\ at\ RT$	**%**	**90.3**
$\frac{\kappa_l}{\kappa_{tot}}\ at\ 723K$	**%**	**87.9**

The band gap $\left(E_g\right)$ and charge carrier effective mass of PbTe depend strongly on temperature due to thermal expansion and the interaction of carriers with the lattice vibrations. Tsang et al. estimated E_g in eV for PbTe as[26]:

(23)

$$E_g\left(T\right) = 4.2 \cdot 10^{-4} T + 0.19 \left(T < 400K\right)$$
$$E_g\left(T\right) = 0.358 \qquad \left(T > 400K\right)$$

Band engineering is an important concept in TE materials, and precise control of band structure and doping level of lead chalcogenides are additional strategies to improve overall device ZT.

3.6.2 A two-phase system based on PbTe matrix/precipitates

Several alloys have been explored as thermoelectric materials, such as PbTe-Se, PbTe-Sn, PbTe-Bi_2Te_3, and PbTe-Sb_2Te_3 [27,28], where both semiconducting phases are of great interest and prospected to yield excellent thermoelectric performance. In particular, the pseudo-binary PbTe-Sb_2Te_3 system has been widely investigated, as PbTe is one of the leading candidates for medium temperature applications. Preliminary experimental studies have demonstrated that the presence of hetero-interfaces in this system can reduce thermal conductivity via additional interfacial phonon scattering, which is analogous to that existing in super-lattice materials.

Theoretically, it has been found that maximal enhancement of the TE power factor in TE materials is possible with a parallel slabs microstructure.[29] Annealing is also an important technique in TE materials since changes in composition and structure, as well as elimination of defects, can be achieved during the process to enhance TE performance. However, to date, only few studies have been conducted to examine the microstructural evolution during annealing.

3.7 PbTe/Ag_2Te-based systems and microstructure evolution

The PbTe/Ag_2Te quasi-binary phase diagram is presented in Figure 9:[30,31]

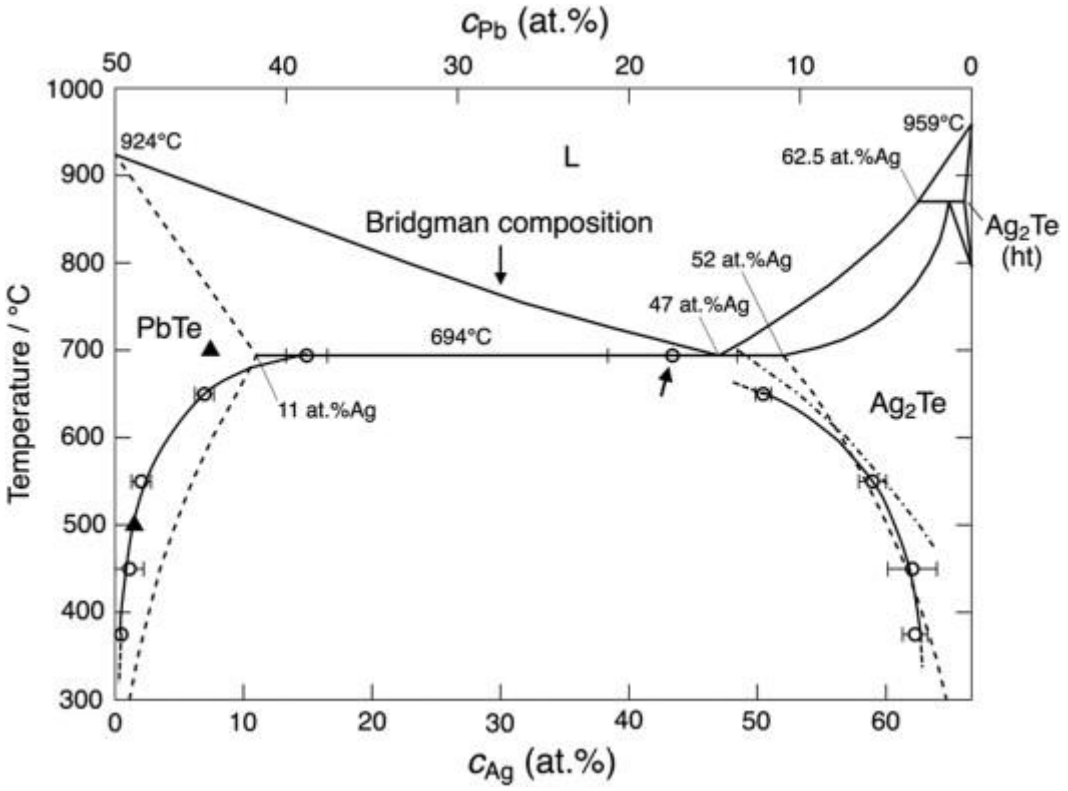

Figure 9 The quasi-binary phase diagram of $(PbTe)_{1-x}(Ag_2Te)_x$ system, showing the strong temperature dependency of Ag_2Te in PbTe.

The supersaturated compound consisting of PbTe and α-Ag_2Te precipitates can be grown after heat treatments below the solvus. The maximum solubility of Ag_2Te in PbTe, which is about 7–11 mol. % at the eutectic temperature of 694 ˚C quickly drops to about 1 mol. % at ~500 ˚C. The Ag_2Te-phase includes three stable polymorphs.[32]. Below 145 °C, a structural distortion occurs and the β-phase with a monoclinic cell ($P2_1/c$). The lattice mismatch between the Ag_2Te (both polymorphs) and PbTe crystal structures is ~ 2%, suggesting that these precipitates could be semi-coherent and oriented with respect to the matrix. α-Ag_2Te has a rock salt lattice structure ($Fm\bar{3}m$) and is stable at the temperature range between 145 °C and 802 °C Above 802°C a BCC like phase- γAg_2Te ($Im\bar{3}m$). [30,33]

3.8 Kinetics of phase transformations

Introducing nanostructured defects is a well-known way to improve TE performance of materials due to scattering of phonons.[34] The challenge in producing such materials is controlling the size, density, and distribution of the precipitates, which corresponds to the phonon mean free path, in order to yield maximum scattering. For homogenous nucleation, the transformation kinetics are deduced using the difference in Gibbs free energy between the two phases:[35]

(24) $$\Delta G = V_0 \left(\Delta G_v + \Delta G_s \right) + s\gamma_s$$

where V_0 and s are the volume and surface area of the nucleus, ΔGv is the change in specific chemical energy, ΔGs is the specific elastic strain energy, and γs the interfacial free energy.

The critical free energy for nucleation as a function of the radius of a spherical nucleus is given by:

$$\Delta G^* = \frac{16\pi\gamma_s^3}{3(\Delta G_v + \Delta G_s)^2} \quad \textbf{(25)}$$

The maximum value of ΔG is the energetic barrier for nucleation, ΔGv, and is attained for a given critical radius, r*

$$\Delta G_v \propto \frac{1}{\Delta T^2} \ \left(\Delta T = T_m - T\right) \quad \textbf{(26)}$$

where ΔT is defined as the degree of super-cooling. The nucleation rate, Ir, depends on both ΔG* and the rate in which solutes arrive at the nucleus, ΔGD, according to the following Arrhenius-type expression:

$$I_{rate} \propto \exp\left(-\frac{\Delta G^* + \Delta G_D}{k_B T}\right) \quad \textbf{(27)}$$

3.9 Synthesis methods common to PbTe compounds

PbTe compounds are well-studied materials that have a variety of appropriate synthesis procedures; here we describe the major ones. NASA has been using the hot-pressing technique for manufacturing PbTe based materials for TE generators in their space missions since the 1960's.[36] In this technique, powder is loaded into a single-action graphite die, and the faces of the top and bottom punches are coated with high-purity alumina to ensure easy removal of the pressed pellet. New dies are baked out at or near the hot-pressing temperature prior to use, to eliminate volatiles that might cause contamination. The die is placed into an inert atmosphere chamber and purged with argon, and heat is applied through the induction unit.

A PbTe compound can be also prepared using the Spark Plasma Sintering (SPS) technique[37,38] , in which elemental Pb and Te are sealed in a quartz vial under an Ar atmosphere and held at 975 °C for 2 h and subsequently quenched in water, followed by homogenization heat treatment at 600 °C for 24 h. The resulting ingot is ball milled for 8 h. The resulting material with the composition PbTe:Na (2%) is consolidated using induction hot pressing at 350 °C for 5 min. The density of the sample has 98% of the theoretical value.

$(PbTe)_{1-x}(Ag_2Te)_x$ compounds are prepared by mixing Ag_2Te and PbTe pieces in appropriate fractions in a quartz tube[30]. The tube is evacuated to less than 10^{-7} torr before it is sealed, while actively pumping. The contents of the sealed ampoule are then melted at 975 °C for 2 h, followed by cooling to 700 °C. The ingot is held at this temperature, which is in the single-phase PbTe region, for 75 h for homogenization. Then, the

ingot is quenched into an iced-brine solution. Finally, pieces of the quenched ingot are annealed in sealed and evacuated ampoules for 1–24 h at 400 °C.

A similar method can be implemented to prepare $(PbTe)_{1-x}(Ag_2Te)_x$ compounds by mixing pure elements in the appropriate amount and sealing them in a quartz ampoule evacuated to 10^{-5} torr or less.[39] The ampoule is subsequently heated to 1000- °C and undergoes melting in a vertical programmable tube furnace. After soaking at this temperature for approximately 6 h, the ampoule is cold-water quenched, followed by annealing and homogenization at 700 °C for 2 days and water quenching again. Then, the ampoule is re-annealed at 500 °C for 3 additional days in order to control the nucleation and growth processes. The resulting ingots are ground into fine powder and then hot-pressed at 427 °C for one hour, to form a dense pellet. The density of the pressed disk is ~98% of the theoretical value.

4 SUMMARY AND RESEARCH GOALS

One of the challenges in understanding the lattice thermal conductivity of two-phase alloys based on PbTe is differentiating between the influence of nano-particle content, density, and size and the effect of the matrix composition (which affects both impurity-scattering and electronic doping). In this research we focus on the Pb-Te-Ag system, which has the potential of forming Ag_2Te precipitates dispersed in a PbTe-based solid solution. The Pb-Te-Ag system has attracted scientific interest owing to its potential for enhanced TE performance, in the form of Ag_2Te-precipitates. The dependence of thermal conductivity on the volume fraction and average size of Ag_2Te precipitates has been investigated, as well as the morphological evolution of Ag_2Te precipitates, though not in a systematic manner.

The goal of this research is, therefore, to form Ag_2Te-precipitates dispersed in a PbTe host matrix for reducing lattice thermal conductivity, to characterize the resulting microstructure down to the nanometer length scale, and to examine the resulting TE performance, which consists primarily of the lattice thermal conductivity, the electronic component of thermal conductivity, electrical conductivity, and the Seebeck coefficient. Obtaining this knowledge will help us improve the TE performance of PbTe compounds.

5 RESEARCH METHODS

5.1 Materials synthesis

We chose Ag as the precipitate agent, since it demonstrated interesting results in previous research in our laboratory.[40] We use Ag as a precipitate agent to form Ag_2Te using the following classical metallurgical approaches to synthesize nanostructured bulk material:[39]

- Solidification from the melt
- Solid-state precipitation upon cooling due to transition from a single to two-phase region
- Formation and subsequent decomposition of β- Ag_2Te metastable phase

Some methods of synthesis were introduced in section 3.10. Our methodology of synthesizing our compounds is as follows:

Ag-alloyed PbTe specimens were synthesized from pure elemental Pb powder (99.96%, Riedel-de Haën®), Te ingots (99.99%, STREM CHEMICALS®), Ag shots (99.999%, Alfa Aesar®), and by mixing in the appropriate molar ratios to obtain the average composition of $(PbTe)_{0.97}(Ag_2Te)_{0.03}$, This composition is a product of composite optimization conducted in our group.[41] The pure Pb, Te, Ag, and Bi raw materials were poured into a quartz ampoule, which was brought to an atmosphere of 120 torr Ar-7% H_2 gas mixture in order to avoid oxidation. The sealed ampoule was then heated to 1000 °C for 6 h in a vertical programmable tube furnace to enable melting, and then slow heated at the rate of 5°C/MIN down to 700 °C, staying at that temperature for 48h for homogenization. The melting procedure was finished by quenching in an ice-water bath. The ingot, a super-saturated PbTe-based solid solution, was then ground into a fine powder and hot-pressed at 650 °C (within the single-phase region) in a 12.5 mm dia. die under a pressure of 45 MPa for 15 minutes under Ar-7% H_2 atmosphere and quenched in iced water. The hot-pressed disks were, finally, aged at 380 °C for 6 hours, and sealed in quartz ampoules for 48 hours under a 120 torr Ar-7% H_2 atmosphere, followed by ice-water quenching.

5.2 Sample preparation

5.1.1 TEM and APT sample preparations

Both TEM and APT samples were created using the *in-situ Lift-Out* method utilizing a dual focused ion beam (FIB) and SEM.

5.3 Density measurements

Archimedes' principle aids in the experimental determination of density by providing a convenient and accurate method for determining the volume of an irregularly shaped object using, for instance, a rock. The principle is that an object totally or partially immersed in a fluid (liquid or gas) is buoyed by a force equal to the weight of the fluid that is displaced. Using the following equation, we can determine the sample's density:

(28) $$B = \frac{D\rho_w}{S - M}$$

where $B \frac{gr}{cm^3}$ is the buoyancy, $D\,gr$ is the dry sample weight, $\rho_w \frac{gr}{cm^3}$ is the water density at a given temperature, $S\,gr$ is the soaked-in-water weight of the sample, and $M\,gr$ is the moist weight of the sample. The method was adapted from ASTM-C373-18[42].

5.4 Thermoelectric properties

The thermoelectric properties are divided into two categories: the thermal measurements and electrical measurements. The thermal part includes thermal diffusivity/conductivity and heat capacity (C_p), while the electrical measurements include the Seebeck coefficient and electrical conductivity.

5.4.1 Electrical measurements

All of our measurements were conducted using the Netzsch SBA-458 Nemesis® system to measure the electrical conductivity and the Seebeck coefficient of bulk materials and thin films at a temperature range of 300 K to 1073 K. All of the measurements were carried out in an Argon atmosphere. Measurement reproducibility was confirmed by the consistency of the heating and cooling thermal cycles on the same sample.

5.4.1.1 Measurement procedure

The sample is placed on a sample holder inside a chamber in a furnace. Each of the two opposite edges of the sample is connected to an electrical contact, a thermocouple, and a micro-heater. The chamber can be either evacuated or continuously purged with an inert gas. The entire measurement procedure is fully automatic.

The furnace starts to heat and follows a predefined program of temperature steps. When a temperature step is reached, electrical conductivity is measured, using the electrical contacts. Then the two micro-heaters generate a temperature difference along the sample and the Seebeck coefficient is measured. Both measurement procedures are repeated at every predefined temperature step. Finally, the furnace cools down and the sample can be removed.

5.4.1.2 Principles of operation

A differential thermocouple is shown in Figure 10. A voltage between two poles is created in the presence of a temperature difference between two different metals. The voltage created by a thermocouple of type K and T is of the order of 20-40 μV/K (compared to 7-15 μV/K for a type R thermocouple).

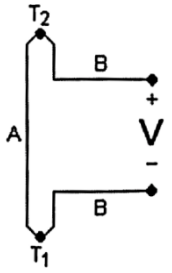

Figure 10:Differential thermocouple (taken from Netzsch® official website).

In the circuit shown in Figure 10, the voltage developed can be derived from:

(29) $$V = \int_{T_1}^{T_2} \left(S_B(T) - S_A(T) \right) dT$$

The Seebeck coefficients of both materials, S_A and S_B, are effectively constant for the measured temperature difference between the two junctions, T_1 and T_2. Thus, the above formula can be approximated as:

(30) $$V = \left(S_B - S_A \right) \left(T_2 - T_1 \right)$$

It should be noted that the analysis performed in the SBA-458 considers the change in Seebeck coefficient of the thermocouple in the temperature range between T_1 and T_2. In the SBA-458, one of the junctions of each differential thermocouple is attached to the sample, as shown in Figure 11. The second junction of each thermocouple is called the reference junction; both prevail at the same reference temperature, T_{ref}.

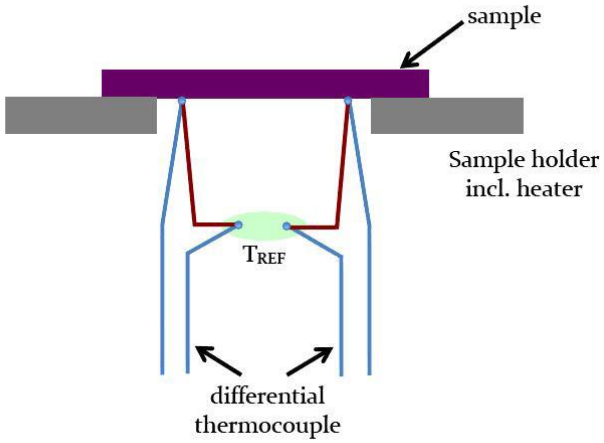

Figure 11: A schematic description of the principle of Seebeck coefficient measurement (taken from Netzsch® official website).

This measurement setup allows a simple way for determining the Seebeck coefficient of a sample, since it can be reduced to the configuration shown in Figure 12.

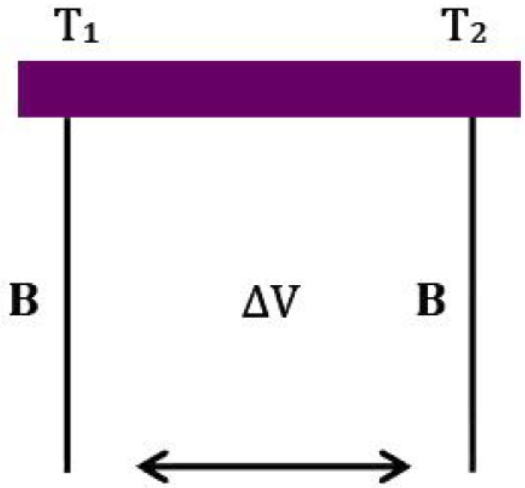

Figure 12: A typical configuration for the measurement of the Seebeck coefficient (taken from Netzsch® official website).

A temperature difference $\Delta T = T_2 - T_1$ is applied by external heaters on the sample, and the built-in voltage ΔV is then measured. Then the Seebeck coefficient of the sample (S) is measured and the known Seebeck coefficient of the thermocouple material B (α_B) is related to ΔT and ΔV using eq.7.

5.4.2 Thermal transport: Laser Flash Analysis (LFA)

To determine the thermal properties of our materials, the Netzsch laser flash apparatus 457 MicroFlash® is used. We can determine the thermal diffusivity of a cylindrical specimen with a 12.7 mm diameter and ~ 3

mm thickness within a wide range of temperatures from -125 °C to 1100 °C using two different exchangeable furnaces.

5.4.2.1 LFA system

The measuring compartment is constructed vertically. The laser system is housed in the lower closed casing, and the laser beam is illuminated vertically toward the specimen's bottom surface. The laser is Nd/glass based with a wavelength of 1054 nm (infrared range).

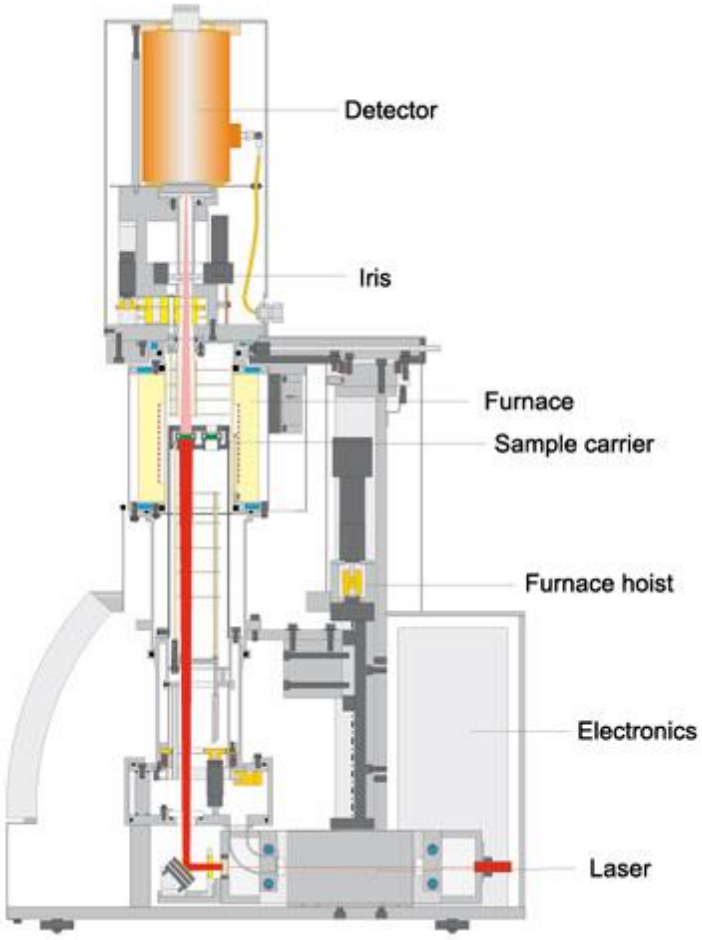

Figure 13 A schematic description of the LFA apparatus (taken from Netzsch® official website).

The thermal signal at the top surface of the sample is probed using an infrared detector. The vertical configuration of the sample holder, furnace, and detector simplifies sample placement and guarantees an optimum signal-to-noise ratio of the detector signal.

5.4.2.2 Principles of operation

For uni-directional heat transport under adiabatic conditions and instantaneous laser pulse, the thermal diffusivity, D, is determined by the equation:

(31) $$D = 1.388 \frac{l_T^2}{t_{0.5}}$$

where l_T is the thickness of the sample and $t_{0.5}$ is the time required for the output signal to reach 50% intensity.

The main features of the LFA-457 system are:

- Temperature range: -125 °C to 500 °C, RT to 1100 °C, (2 exchangeable furnace types)
- Heating and cooling rates: 0.01 to 50 $Kmin^{-1}$
- Laser pulse energy: up to 18 $Jpulse^{-1}$, (adjustable power)
- Thermal diffusivity measuring range: 0.01 to 1000 mm^2s^{-1}
- Thermal conductivity measuring range: 0.1 to 2000 $Wm^{-1}K^{-1}$
- Sample dimensions: 10 mm to 25.4 mm diameter and 1 mm to 6 mm thickness;

The LFA technique also includes important features such as pulse length correction, heat-loss corrections, and integrated conventional models[43]. The latter include the following options: non-linear regression of the output signal for a Cowan-type fit[44], an improved Cape-Lehmann[45] model for three-dimensional heat transport, and radiation correction for semi-transparent samples.

5.5 Microstructure Analysis

In order to determine phase composition, homogeneity, and microstructure, x-ray diffraction (XRD) and high-resolution scanning electron microscopy (HRSEM) equipped with an energy dispersive spectrometer (EDS) were used. The nano-structure was investigated using transmission electron microscopy (TEM) and atom probe tomography (APT), for further understanding of the behavior of our compounds.

5.5.1 X-ray Diffraction

Powder X-ray analysis was conducted in order to determine the phases of each step of the heat-treated ingots. The measurements were carried out using a Rigaku Smartlab® XRD diffractometer with an angular resolution of 0.02° applying Cu-K_α radiation at the angular range of 2θ = 20-90 °. The data were collected by angular scanning with 0.02 ° steps

5.5.2 Scanning Electron Microscopy (SEM)

Most of the microstructure characterization of the samples was carried out using a Zeiss® Ultra Plus high-resolution scanning electron microscope (HR-SEM), equipped with 80mm^2 active area Oxford® SDD EDS detector with an energy resolution of 127 eV, located at the Materials Science & Engineering Department and equipped with a Schottky field-emission electron gun. The images presented in this study were taken with secondary and backscattered electron detectors. Some of the images were taken using a Zeiss® Merlin high-resolution scanning electron microscope, located at the Max-Planck-Institut für Eisenforschung GmbH, Düsseldorf, Germany.

5.5.3 Transmission Electron Microscopy (TEM)

Nanostructure characterization procedures were conducted using the Philips CM20 200 kV LaB_6 TEM, located at the Max-Planck-Institut Für Eisenforschung GmbH, Düsseldorf, Germany, and The FEI Tecnai™ TEM, located at the Materials Science & Engineering Department, Technion.

TEM lamellae specimens were prepared using a dual-beam scanning electron microscope/focused ion beam (Helios NanoLab 650, FEI), following the site-specific "lift-out" method. STEM investigations were carried out using an aberration-corrected FEI Titan Themis microscope operated at 300 kV. The convergence angle of the probe was 24 mrad, and the collection angles of the annular bright field (ABF) and high angle annular dark field (HAADF) detectors were 8~16 mrad and 73~352 mrad, respectively. HRTEM characterization was carried out at the Max-Planck-Institut Für Eisenforschung GmbH, Düsseldorf, Germany.

5.5.4 Atom Probe Tomography (APT)

Atom probe tomography (APT) is a technique capable of concurrently determining three-dimensional material structure and chemistry at near-atomic resolution[46]. It was developed from the field emission microscope (FEM) and field ion microscope (FIM). Erwin Wilhelm Müller invented the first FEM in 1936, at the Technical University of Berlin, Germany. It utilized a negative potential to emit electrons to the surface of a sharp metallic needle. The electrons are then projected onto a phosphorus screen to form an image.

In 1956 Müller made the discovery of field evaporation.[47] Field evaporation is a phenomenon in which surface atoms sublime from a material's surface in the presence of a high electrostatic field. By careful control of the field, atoms can be removed in an orderly fashion. In 1967 and 1968, Müller and Panitz constructed the first atom probe microscope by adding a mass spectrometer to an FIM to identify the composition of the sample atoms that were field evaporated[48].

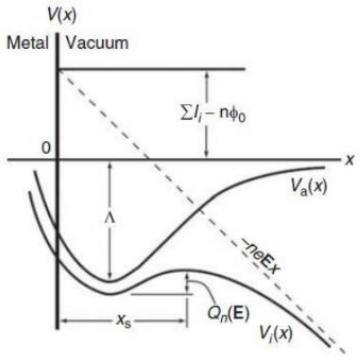

Figure 14: V(x) is potential energy as a function of distance away from the surface of a specimen, x = 0. $\boldsymbol{V_a(x)}$ is the potential energy of an atom in the absence of an electric field, E, and $\boldsymbol{V_i(x)}$ is the potential energy of an ion in its ith ionization state in the presence of E. $\boldsymbol{I_i}$ is the ith ionization state of an ion, e is the charge of an electron, n is the number of electronic charges, Λ is the cohesive energy of a solid. $\boldsymbol{\phi_0}$ is the local work function, $\boldsymbol{Q_n}$ (E) is the height of the Schottky hump, and $\boldsymbol{x_s}$ is the position of the maximum value of the Schottky anomaly.

Once generated at the surface, the ions are accelerated by the surrounding electric field. The ions are expected to follow only the field lines defined by the electrostatic field and should hence follow exactly the same trajectories whatever their mass or charge-state, at any applied voltage. The probability of ionization depends on the relative transparency of the potential barrier to the electron tunneling process. Ions strike the position-sensitive detector and, in atom probe tomography, the location of the impact will subsequently be treated to build a tomographic reconstruction of the analyzed volume. This is achieved by using a needle-shaped tip geometry for the specimen, with an end radius smaller than 100 nm. The shape of the tip is generally a truncated cone with a hemispherical cap, although some deviations from the sphere shape are encountered[49,50]. The half angle at the apex of the cone is referred to as the shank angle of the tip. The radius of the hemisphere is considered the radius of the curvature of the tip. The electric field, F, generated at the apex of a needle-shaped specimen with a radius of curvature, R, that is subjected to a high voltage, V, can be estimated based on the idealized expression for a charged sphere. It does require slight modification to account for the fact that the tip is not exactly spherical, giving[46]:

(32)
$$F = \frac{V}{k_f R}$$

The analysis in APT can be divided into two separate steps. First is the experiment, where ions are field evaporated and detected, and second is the reconstruction. In the reconstruction, the original atomic positions and identities are determined by the hit order and position on the detector along with the time of flight information about the hit from the mass spectrometer. The mass spectrometer relies on the fact that each ion has a typical mass and takes a different amount of time to reach the detector. This is schematically presented in Fig. 15[51]:

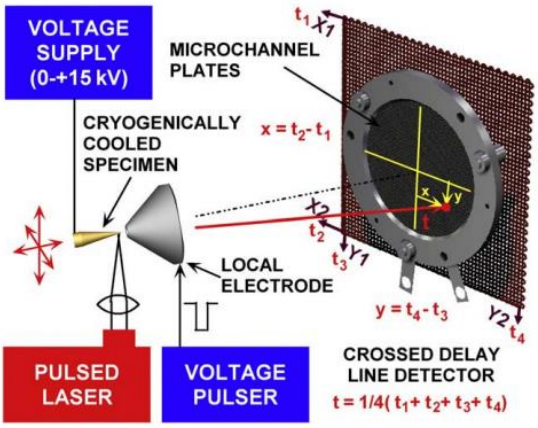

Figure 15: Schematic diagram of a local electrode atom probe (LEAP) with a crossed delay line single atom detector at the end of the time-of-flight mass spectrometer. Both voltage and laser pulsing modes of field evaporation are shown.

The x and y atomic coordinates on the specimen are derived from the X and Y positions of the hit of each ion on the position-sensitive detector. The X position is given by t_2-t_1 and the Y position by t_4-t_3. t is the time from the evaporation pulse to the pulse recorded at one end of the delay line due to the impact of the ion. The z coordinate is estimated from the sequence in which the atoms are collected, assuming uniform field evaporation over the surface of the specimen. A third delay line is incorporated to assist in the assignment of the mass-to-charge to the correct ion when multiple ions strike the detector in the same evaporation pulse.

The mass-to-charge state is estimated from the potential energy neV of the escaping ion, where V is the applied voltage between the specimen and the local (or counter) electrode that is the entrance aperture to the mass spectrometer. The ion velocity, v, can be estimated from the distance from the specimen to the single atom detector, d, and the flight time, t.

Thus we can calculate the mass using the next equation[52]:

$$\frac{m}{n} = \frac{c\left(V_{dc} + \alpha V_{pulse}\right)t^2}{d^2} \quad (33)$$

where V_{dc} and V_{pulse} are the direct and pulse voltages applied to the specimen, respectively; α is the pulse amplitude coupling factor to account for some loss in the effectiveness of the pulse, and c is a constant ($c=1.93\times10-4$) used to convert the mass into atomic mass units.

The time-of-flight mass spectrometer has sufficient mass-resolving power to detect individual isotopes of all elements. The typical detection (or collection) efficiency is 50–60 % of the ions removed from the specimen, and in more advanced machines this can reach up to 80%.[53] The loss is mainly due to some ions striking the inter-channel regions of microchannel plates in the position-sensitive detector, and thereby not being detected.

A color-coded sphere or dot is plotted for each atom of interest at its magnified coordinates and an atom map can be visualized. Using the 3D reconstruction, we can determine different phases, clusters, and segregation to microstructural features, such as dislocations, interfaces, and grain boundaries. These may be deduced from local solute enrichments. The local density of atoms is a combination of the solute concentration and the atomic density of the phases. The interpretation of solute enrichments or partitioning solely from atom maps must be handled carefully. Many factors lead to distortions in the observed density of atoms, such as effects due to different evaporation fields for different phases, trajectory aberrations at the emergence of major poles, and zone lines on the surface.

The concentration of an element i in an analyzed volume or a selected volume is given in atomic percent by $C_i = \frac{N_i}{N_t}$, where Ni is the number of atoms of the element and Nt is the total number of atoms in the volume.

The standard error of the concentration estimate due to counting statistics, σ, is given by:[20]

(34) $$\sigma = \sqrt{\frac{C_i\left(1-C_i\right)}{N_t}}$$

These features and the morphology and size of phases are visualized with the use of iso-concentration surfaces. The 3D data is divided into voxels, or small cubes, that contain 20 to 100 atoms, and the concentration of one or more selected elements are estimated for each voxel. The surface of a particular concentration over the entire three-dimensional volume can be constructed with a marching cube algorithm, which is a computer graphics algorithm used to extract a polygonal mesh of an isosurface from a three-dimensional discrete scalar field (also called a voxel). The algorithm processes the 3D data in scan-line order and calculates triangle vertices using a linear interpolation.[54] The concentration used for the surface is generally selected to be approximately midway between the solute concentrations of the coexisting phases. The appearance of the surface can be refined by the use of smoothing techniques or downsizing the data. Using the iso-concentration surface, the precipitates' number density (Nv) can be deduced.

Another tool we use is the proximity histogram (proxigram), which is the profile of the local atomic concentrations vs. proximity to an interface, and is the most direct way to illustrate the interfacial segregation. We perform three main data analysis steps to generate a proxigram:

1. A sampling to generate a regular grid of concentration points from the individual atomic positions
2. An interpolation to identify the iso-concentration surface in the regular grid
3. Correlation of the surface to the original set of discrete, three-dimensional atomic positions

6 RESULTS

This chapter will describe the experimental results obtained in this study in three main sections. The first section describes the microstructure characterization using XRD for phase identification and HRSEM for defect and precipitate number density (N_v) analysis. The second section details the thermoelectric measurements and includes TE characterization, electrical conductivity, Seebeck coefficient measurements, and thermal conductivity. The last section describes the use of advanced microscopy on the samples, TEM and APT, and the correlation between the nano/micro- structure and the TE properties.

6.1 Materials synthesis optimization

6.1.1 Hot-Press (HP) optimization

EC is correlated to the density of the material. To obtain the best results, we performed HP optimization, and the results are shown in Fig. 16.

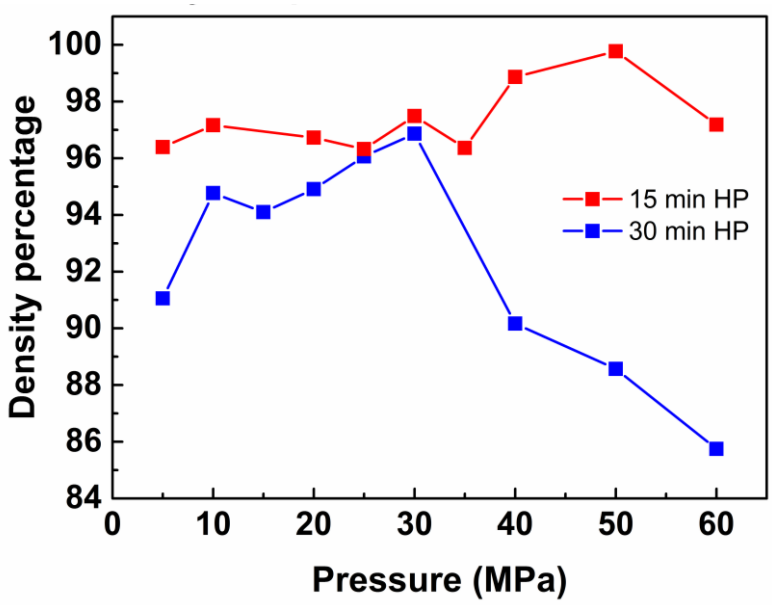

Figure 16 HP density results showing the relative density of each HP, time, and pressure

We found optimized conditions for HP ingots with 650 °C at 50 MPa for 15 minutes.

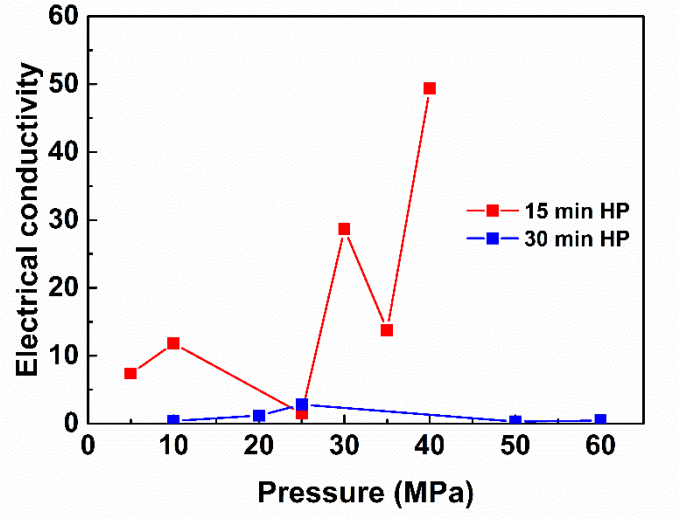

Figure 17 Electrical conductivity at RT correlated with the pressure utilized on the specimen when hot-pressed at 650°C,

Fig. 17 shows the correlation between density and electrical conductivity (residual to the pressure).

6.2 Microstructure characterization

This section focuses on precipitate number density, Nv. The analysis was carried out for the AQ specimen and those aged at 380 °C for different durations. The Nv values measured for both the 6 h and 48 h aged specimens are compared to their counterparts that are doped with Bi.

6.2.1 Phase identification: X-Ray Diffraction (XRD)

We performed an XRD analysis on the specimens prepared in the multi-stage process detailed in Section 5.1 to validate that we obtained the desirable single-phase PbTe. The XRD patterns presented in Fig. 18 indicate the existence of a single-phase PbTe material. As we found out later, there is precipitation even at the AQ specimen. These precipitates are very small and might not be detectible with simple XRD.

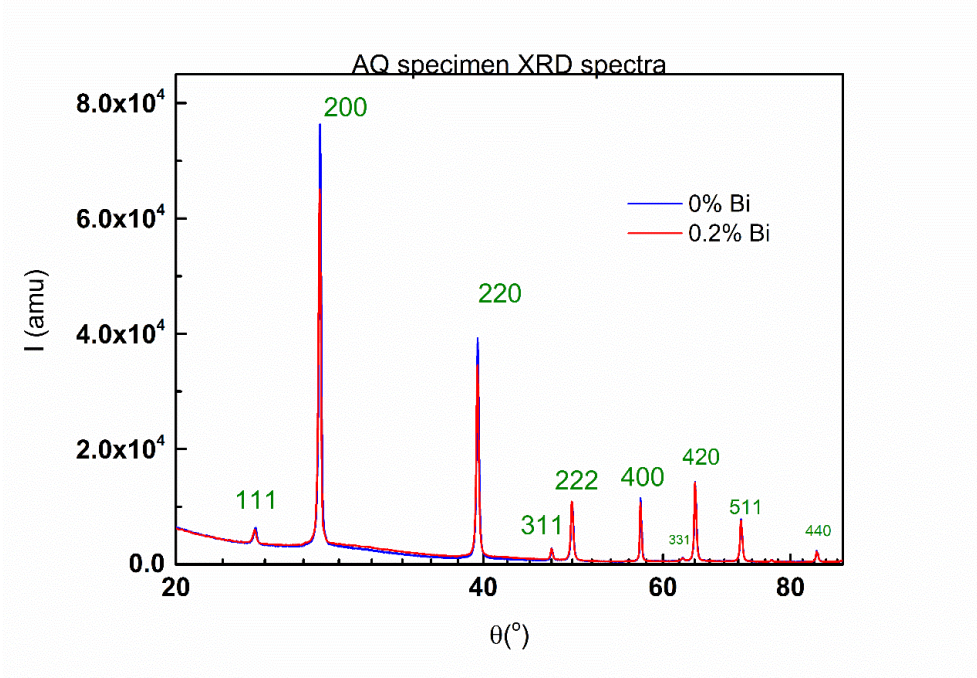

Figure 18 XRD diffraction of AQ specimen: 0 at. % Bi (blue) and 0.2 at. % Bi (red) corresponding with the rock-salt PbTe crystal structure (JCPDS number 04-002-0317)

6.3 Precipitate number density (N_v) analysis

This section presents the microstructure analysis obtained using extensive sampling of HRSEM images that were taken from the aged samples. We performed HRSEM analysis for several purposes related to thermal conductivity analysis, given that the latter strongly correlates with a material's microstructure.

We are interested in the presence of nanometer-sized second-phase precipitates, which are undetectable in XRD and are useful for reducing thermal conductivity. All micrographs presented demonstrate the microstructure variety obtained during the different heat treatments. Herein, we are interested in quantitative precipitate size analysis and particularly the precipitate number density, N_v.

Figure 19 through 21 show the Ag2Te precipitates evolution in the PbTe matrix for the Bi-free samples. These micrographs were taken using the ion beam in the FIB using the TLD detector. The precipitates are less susceptible to the ion beam, and therefore the matrix is etched in a higher grade, which allows us to distinguish between the precipitates and the matrix. PbTe is a relatively soft alloy, which makes it difficult to polish the top surface and obtain HRSEM figures without leaving scratches and other defects; hence, FIB etching was used. It is common that HRSEM figures present this material with defects.

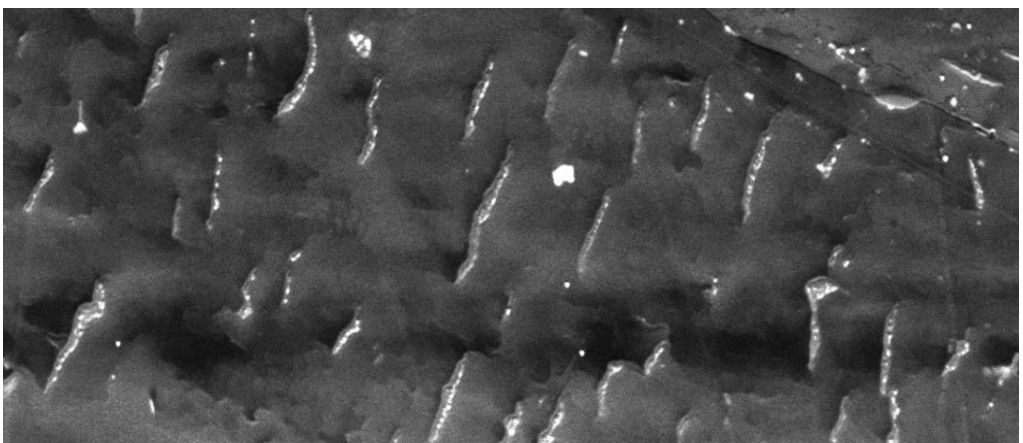

Figure 19 FIB ion image of a Bi-free sample AQ, using a TLD detector. The dark background is the matrix and the bright needles are the precipitates.

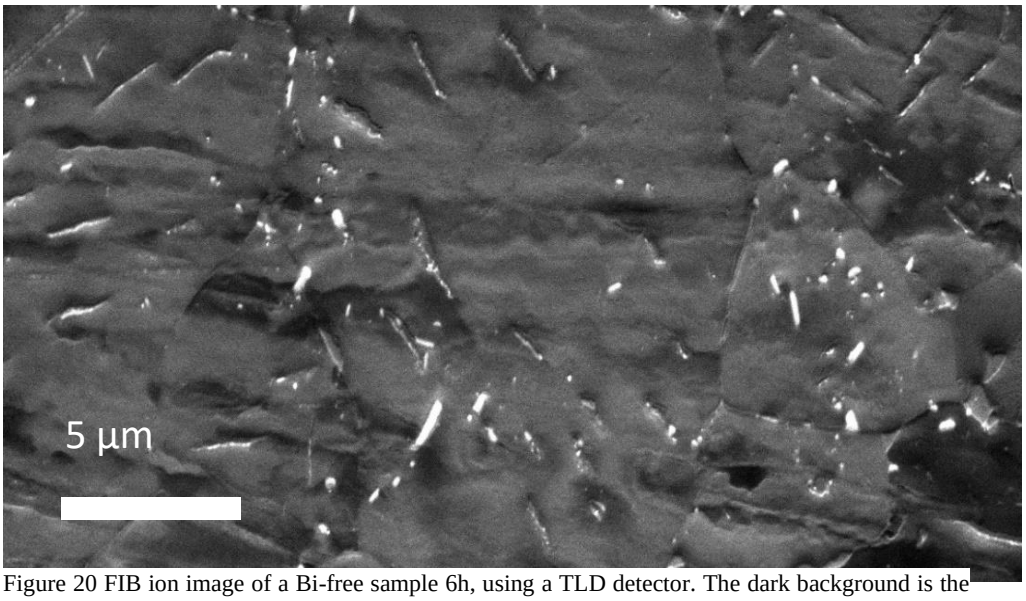

Figure 20 FIB ion image of a Bi-free sample 6h, using a TLD detector. The dark background is the matrix and the bright needles are the precipitates.

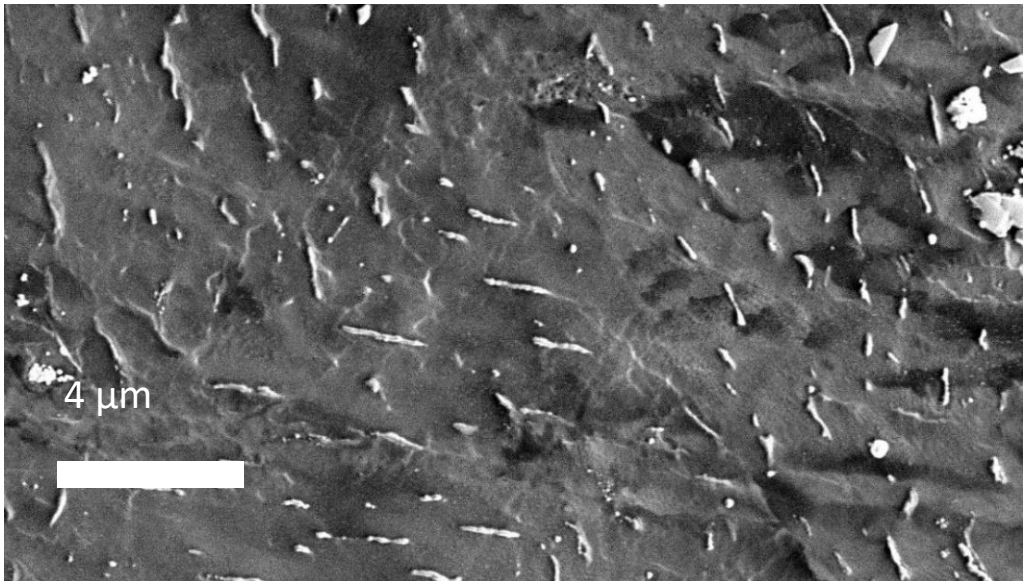

Figure 21 FIB ion image of a Bi-free sample 48h, using a TLD detector. The dark background is the matrix and the bright needles are the precipitates.

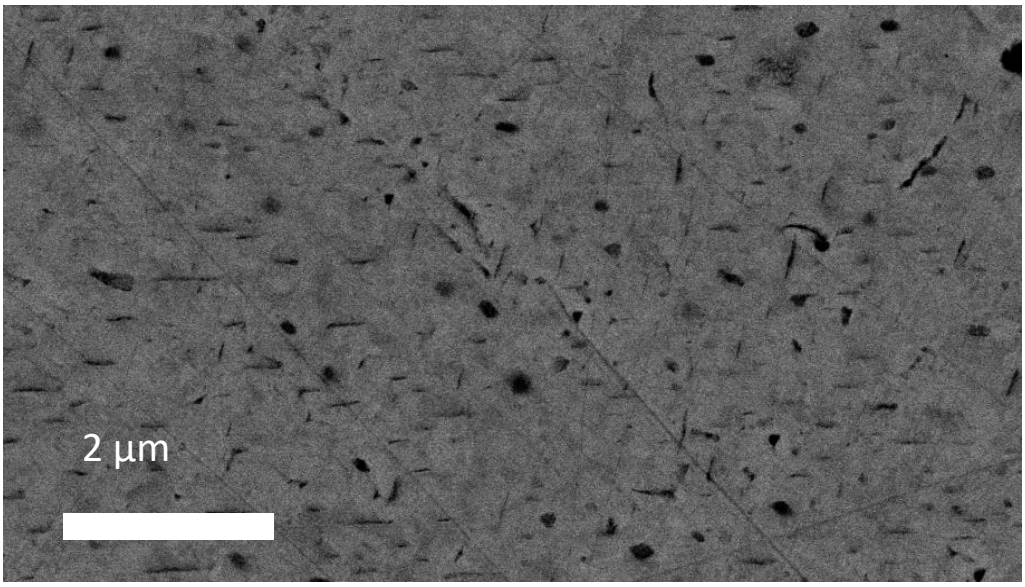

Figure 22 HRSEM image of 0.2 at. % Bi AQ, using a BSE detector. The grey background is the matrix and the precipitates are the dark dots.

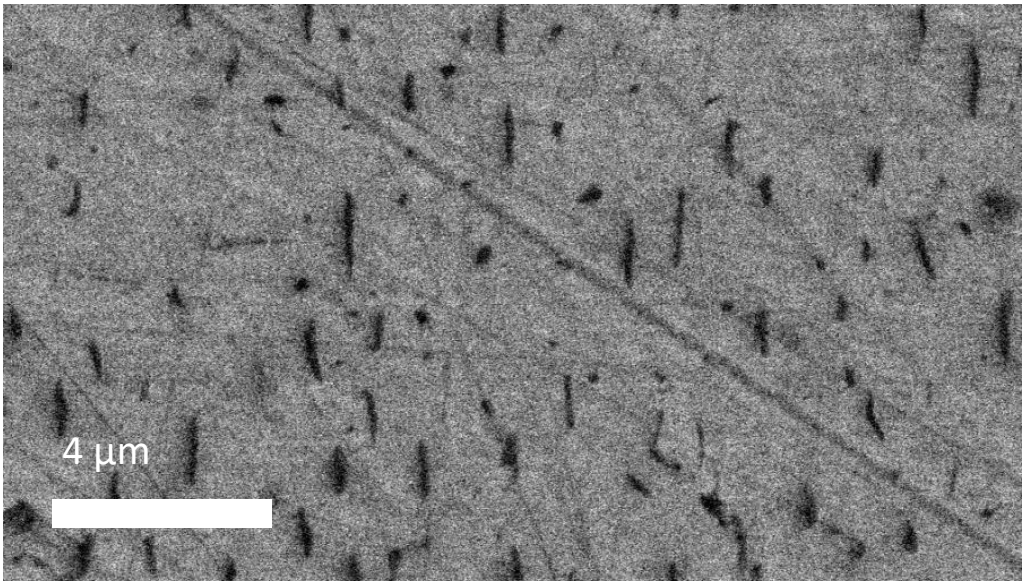

Figure 23 HRSEM image of 0.2 at. % Bi 6h, using BSE detector. The grey background is the matrix and the precipitates are the dark dots

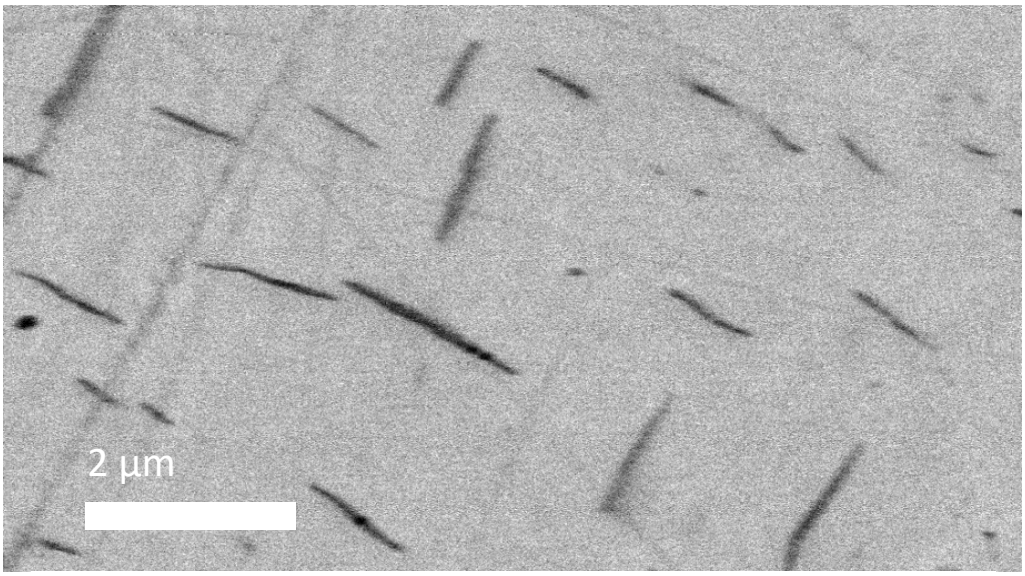

Figure 24 HRSEM image of 0.2 at. % Bi 48h, using a BSE detector. The grey background is the matrix and the precipitates are the dark dots.

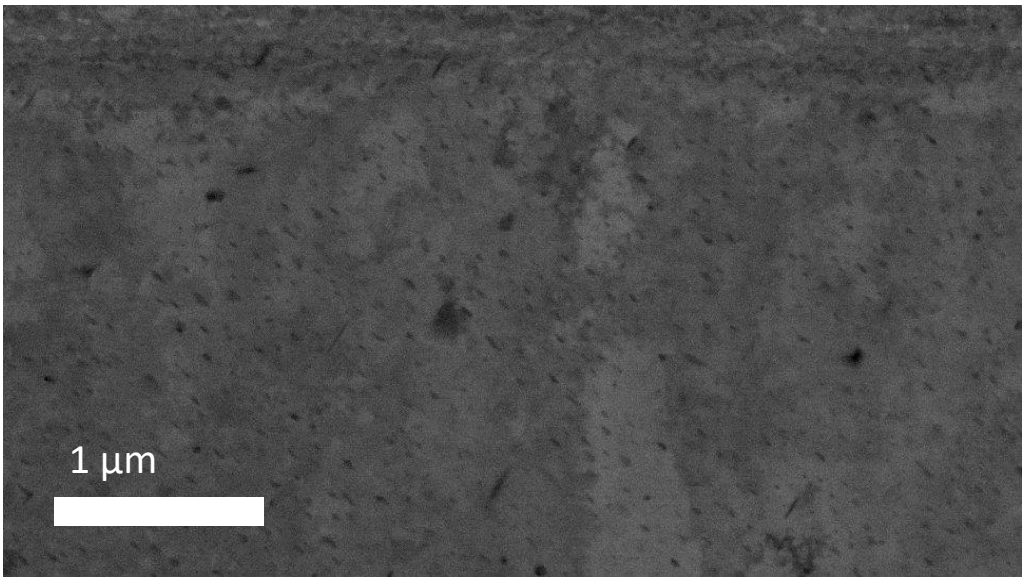

Figure 25 HRSEM image of 0.4 at. % Bi AQ, using a BSE detector, orientation contrast. The grey background is the matrix and the precipitates are the dark dots.

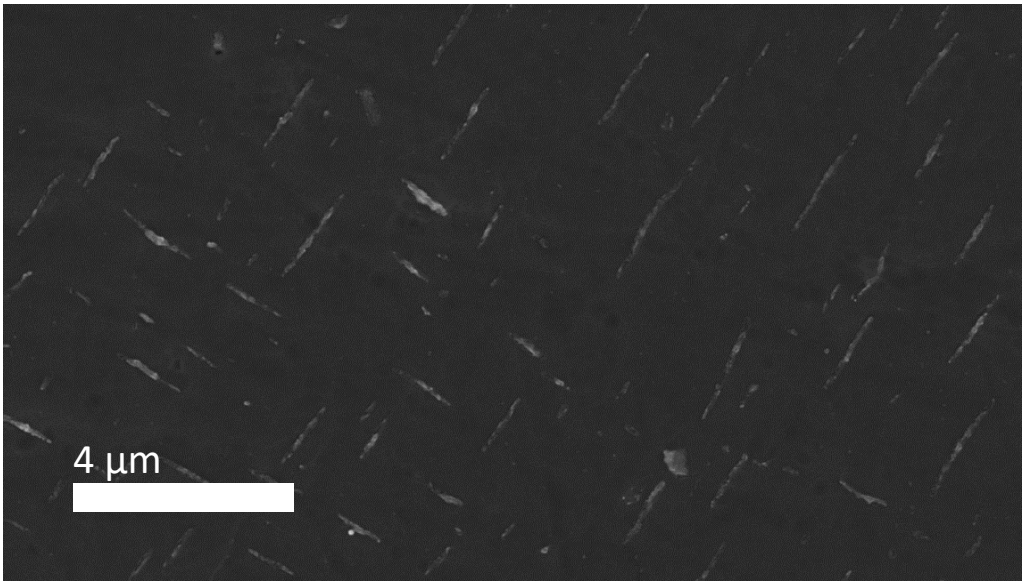

Figure 26 HRSEM image of 0.4 at. % Bi 6h, using an SE detector after FIB etching, orientation contrast. The dark background is the matrix and the bright needles are the precipitates.

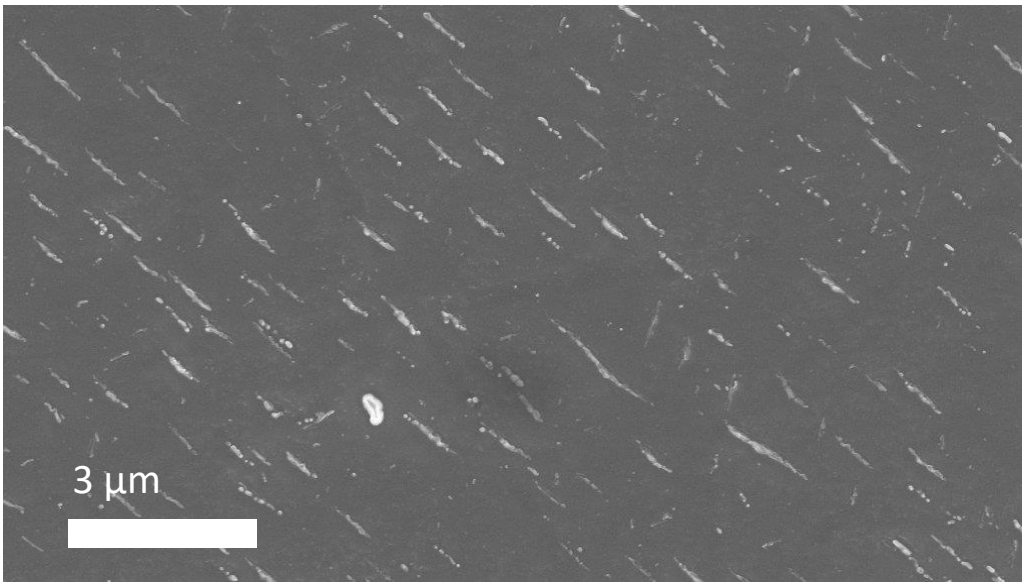

Figure 27 HRSEM image of 0.4 at. % Bi 48h, using an SE detector after FIB etching, orientation contrast. The dark background is the matrix and the bright needles are the precipitates.

EDS analysis was performed on the precipitates showing a silver-rich particle, while the matrix showed almost no signal from the Ag, as shown in **Error! Reference source not found.**.

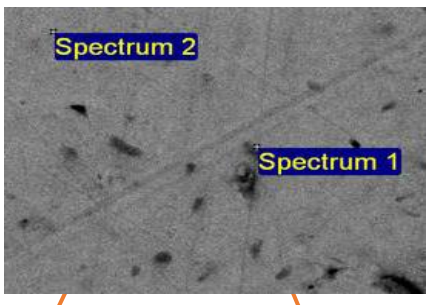

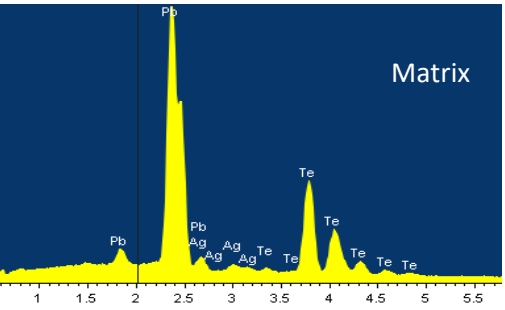

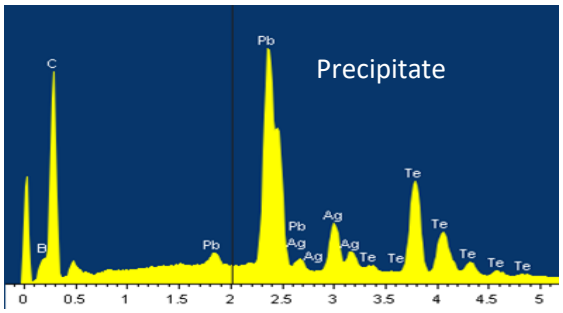

The N_v values calculated are not higher than 10^{20} m^{-3}, as seen in Figure 4. Hence, a higher resolution microscopy was used. Assuming that the precipitates are spread homogenously across the specimen and their size and shape remain the same, we can count the amount of precipitates seen in the micrograph, and utilize the following conversion to volume values:

(35) $$N_v = \left(\frac{number\ of\ precipitates}{S \times (pixel\ factor)}\right)^{3/2}$$

where S is the measured area in which the precipitates were counted, and the pixel factor is the conversion of pixels to nm/μm (using the scale given in the micrograph). We repeated this several times with different samples to achieve statistical confidence.

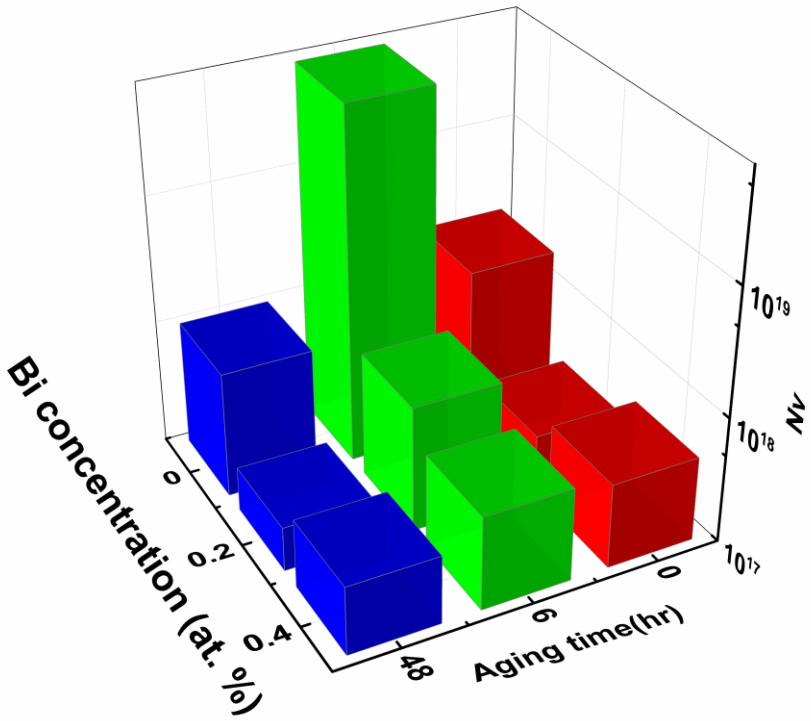

Figure 28 Nv (m^{-3}) is given for the different aging times and Bi concentrations

We can see that the N_v of the bismuth free sample is higher than the Bi-doped counterparts. There is an increase after short aging times and a decrease for longer times for all samples.

Table 2 Nv (m^{-3}) of precipitates for different Bi concentrations and annealing times

Bi concentration %at / aging time (h)	**0**	**6**	**48**
0	$(5\pm1.5)x10^{17}$	$(1.07\pm0.46)x\ 10^{18}$	$(4.0\pm1.5)x10^{17}$
0.2	$(1.63\pm0.58)x10^{17}$	$(5.87\pm1.01)x10^{17}$	$(2.24\pm0.83)x10^{17}$
0.4	$(3.5\pm7.34)x10^{17}$	$(5.55\pm0.81)x10^{17}$	$(4.72\pm0.95)x10^{17}$

6.4 Thermoelectric measurements

We measured the TE transport properties at a temperature range from room temperature to 300 °C. Graphical representations of the temperature-dependent electrical conductivities, classified according to the aging times, are presented in this section.

6.4.1 Heat capacity

Heat capacity values were determined using LFA for a temperature range between room temperature (RT) and 300 °C, with alumina standards as reference samples. The heat capacities of several samples are presented in Figs. 31 through 33. It can be seen that the heat capacity values of all specimens for the entire temperature range are very close to each other. Each chart shows the temperature dependence of the as-quenched (AQ) samples and those aged at 6 h and 48 h (denoted as 6 h and 48 h).

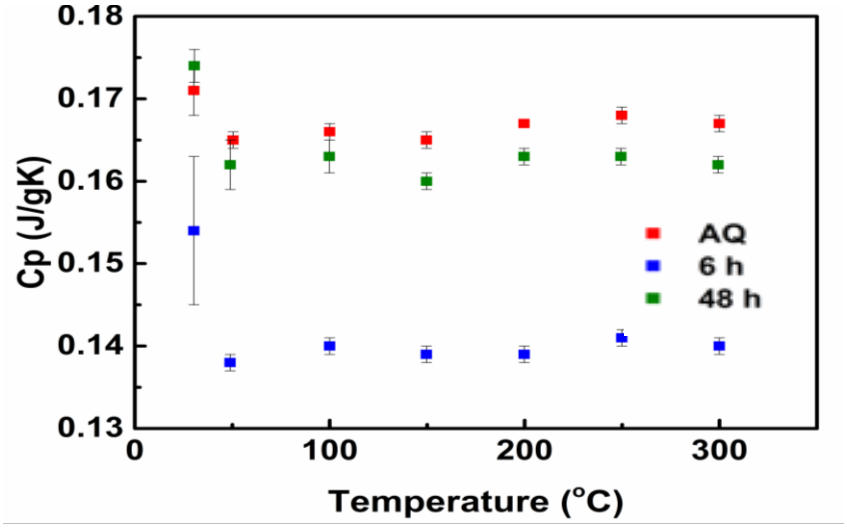

Figure 29 The temperature dependence of the heat capacity values as measured for the 0.2 at. % Bi samples for the Bi-free series of specimens aged at 380 °C for 0, 6, and 48 hours

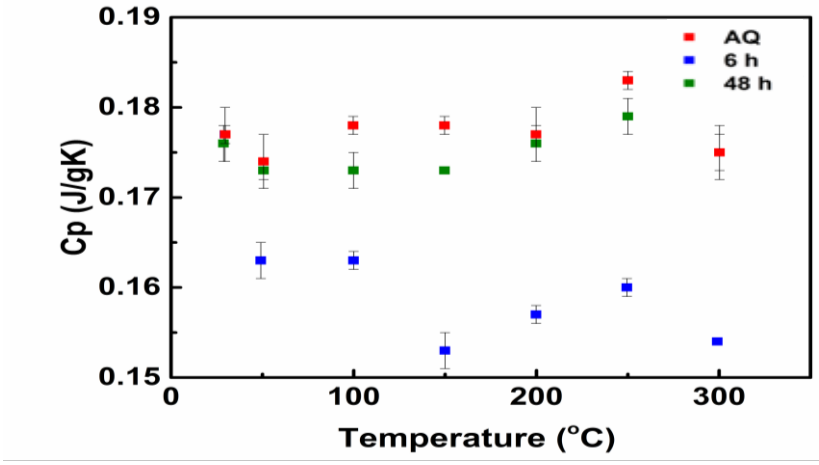

Figure 30 The temperature dependence of the heat capacity values as measured for the Bi-free samples, for the Bi-free series of specimens aged at 380 °C for 0, 6, and 48 hours

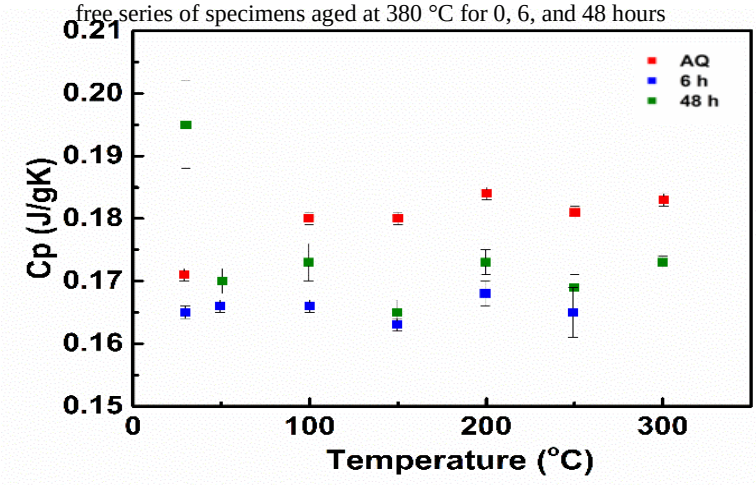

Figure 31 The temperature dependence of the heat capacity values as measured for the 0.4 at. % Bi samples for the Bi-free series of specimens aged at 380 °C for 0, 6, and 48 hours

The Cp remains relatively stable and constant for each temperature and compound.

6.4.2 Thermal diffusivity

We measured the thermal diffusivity for all of the samples using LFA, for a wide temperature range from RT to 300 °C.

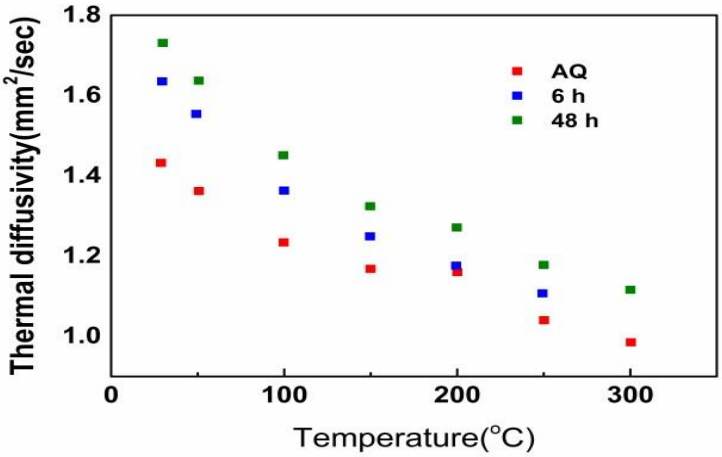

Figure 32 The temperature dependence of the thermal diffusivity values as measured for the Bi-free samples, for the Bi-free series of specimens aged at 380 °C for 0, 6, and 48 hours

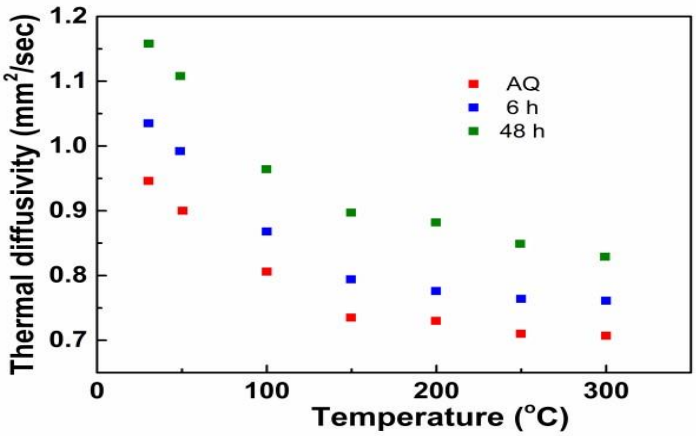

Figure 33 The temperature dependence of the thermal diffusivity values as measured for the 0.2 at. % Bi samples, for the Bi-free series of specimens aged at 380 °C for 0, 6, and 48 hours

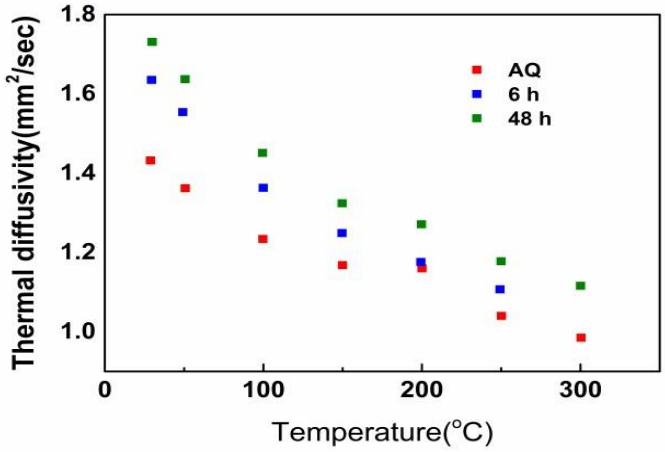

Figure 34 The temperature dependence of thermal diffusivity values as measured for the 0.4 at. % Bi samples, for the Bi-free series of specimens aged at 380 °C for 0, 6, and 48 hours

6.4.3 Thermal conductivity

We calculated the thermal conductivities of the compounds based on EQ 31, as a product of thermal diffusivity, heat capacity, and density while comparing to alumina as a sample reference. Whereas the materials densities, as shown in Table*3* , were measured at room temperature and considered to be constant, the thermal diffusivities were determined using LFA for a wide temperature range. The heat capacities were determined indirectly by a reference sample using LFA, for the same temperature range.

Figure 35 shows the thermal conductivity dependence on temperature for one cycle for each of the samples. The Bi-free sample and 0.2 at. % Bi show a similar trend of decreasing thermal conductivity after short aging times and an increase after longer times. The higher the Bi-doping, the higher the thermal conductivity, probably due to a larger electronic component of the thermal conductivity as shown in Fig. 36.

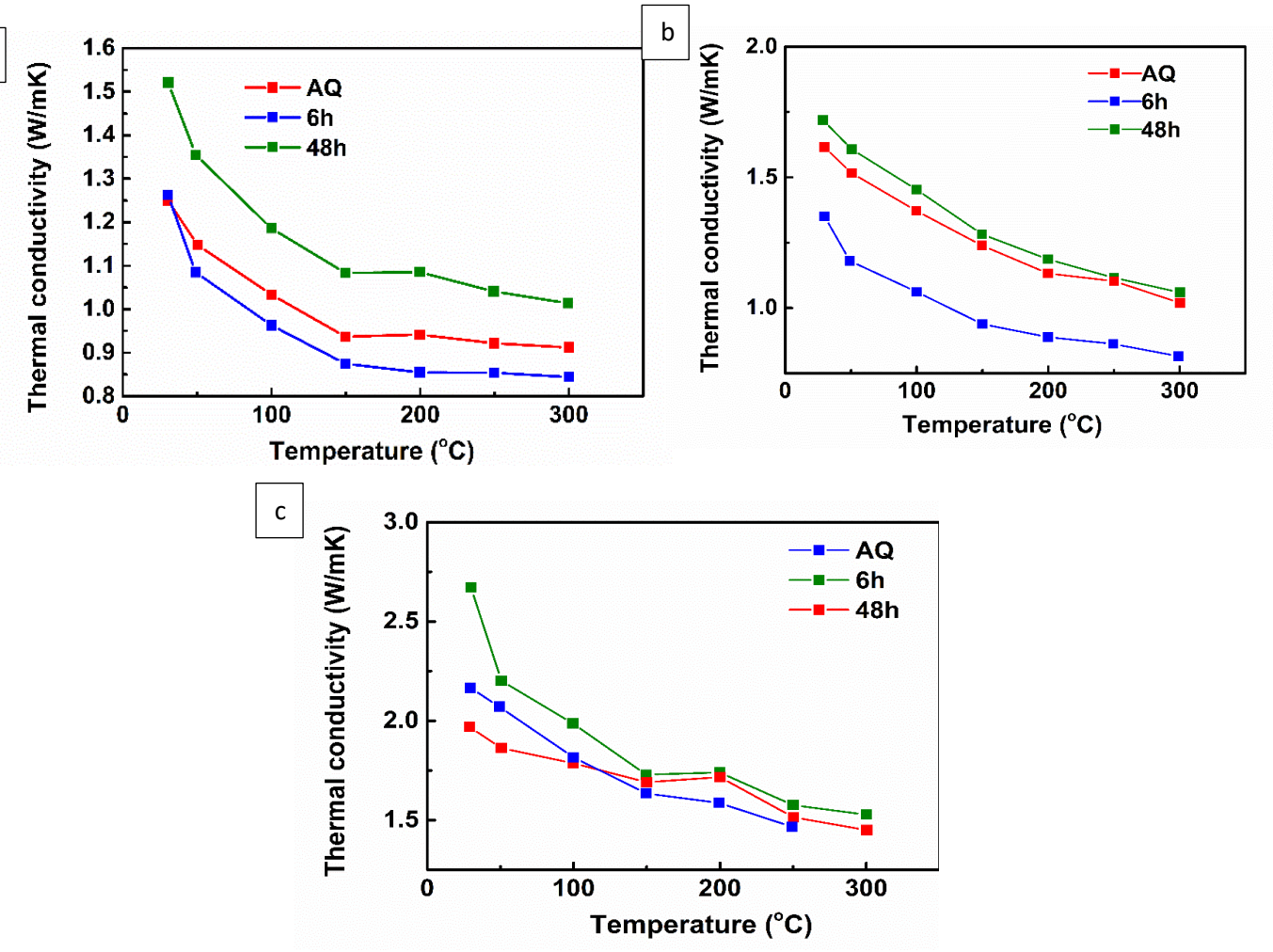

Figure 35 Thermal conductivity for different aging times: (a) Bi-free samples, (b) 0.2 at% Bi, (c) 0.4 at.% Bi

Table3 Density of the specimens

Specimen(at. %Bi,hr)	**0,AQ**	**0,6**	**0,48**	**0.2,AQ**	**0.2,6**	**0.2,48**	**0.4,AQ**	**0.4,6**	**0.4,48**
Density[gr/cm^3]	7.725	7.925	7.548	7.938	7.925	7.731	8.043	8.029	7.913
Relative density (%)	93.7	96.1	91.6	96.3	96.1	93.8	97.6	97.4	96

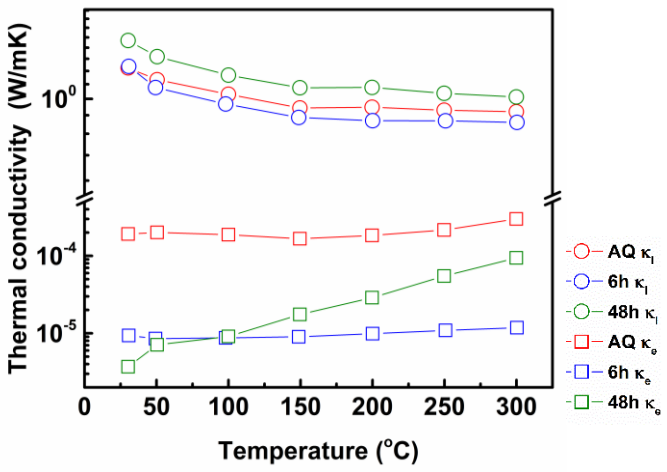

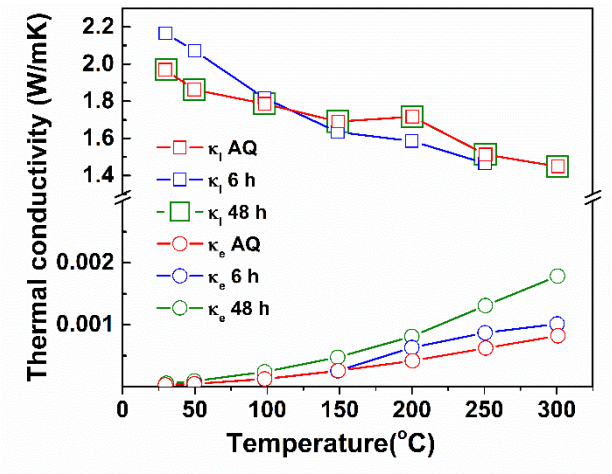

Figure 36 Comparison between the lattice component of the thermal conductivity (circles) and the electric component (squares) for the Bi-free sample (above) and 0.4 at.% Bi (below)

The electronic part of the TC was calculated using the Wiedemann-Franz rule mentioned in section 3.5.1

(a)

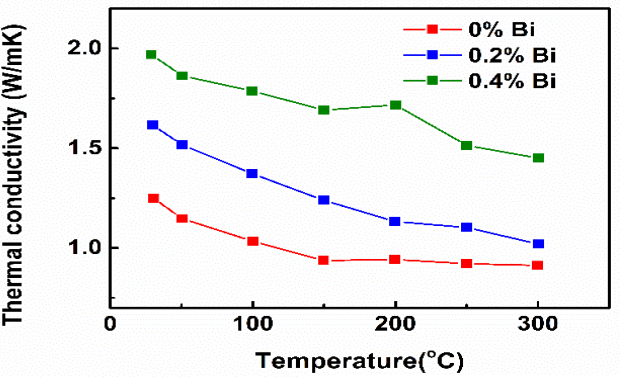

(b)

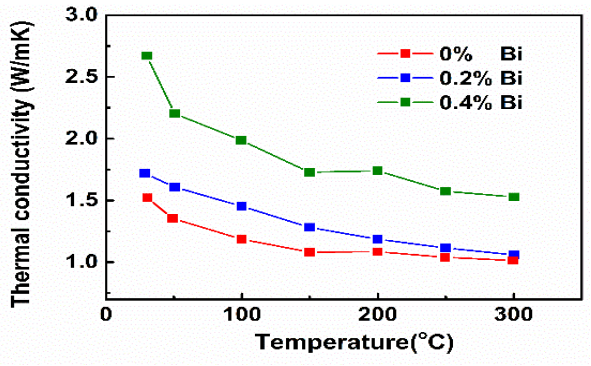

Figure 37 Temperature dependence of thermal conductivity for different Bi concentrations for various aging times: (a) AQ samples, (b) 6h aging time, (c) 48h aging time

(c)

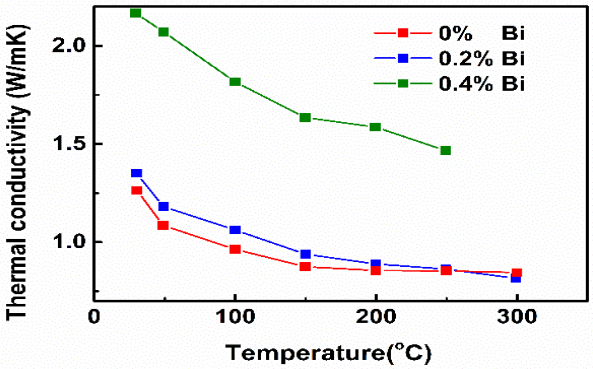

6.5 Electrical Properties

Using the SBA we measured both the Seebeck coefficients and electrical conductivity for the temperature range RT–300°C.

6.5.1 Electrical conductivity

Figure 38 displays electrical conductivity vs. temperature. The Bi-free sample exhibits a decrease in electrical conductivity for longer aging times, which can be interpreted as consumption of Ag from the supersaturated matrix. The Bi-doped samples have higher overall electrical conductivity values than those of their undoped counterparts.

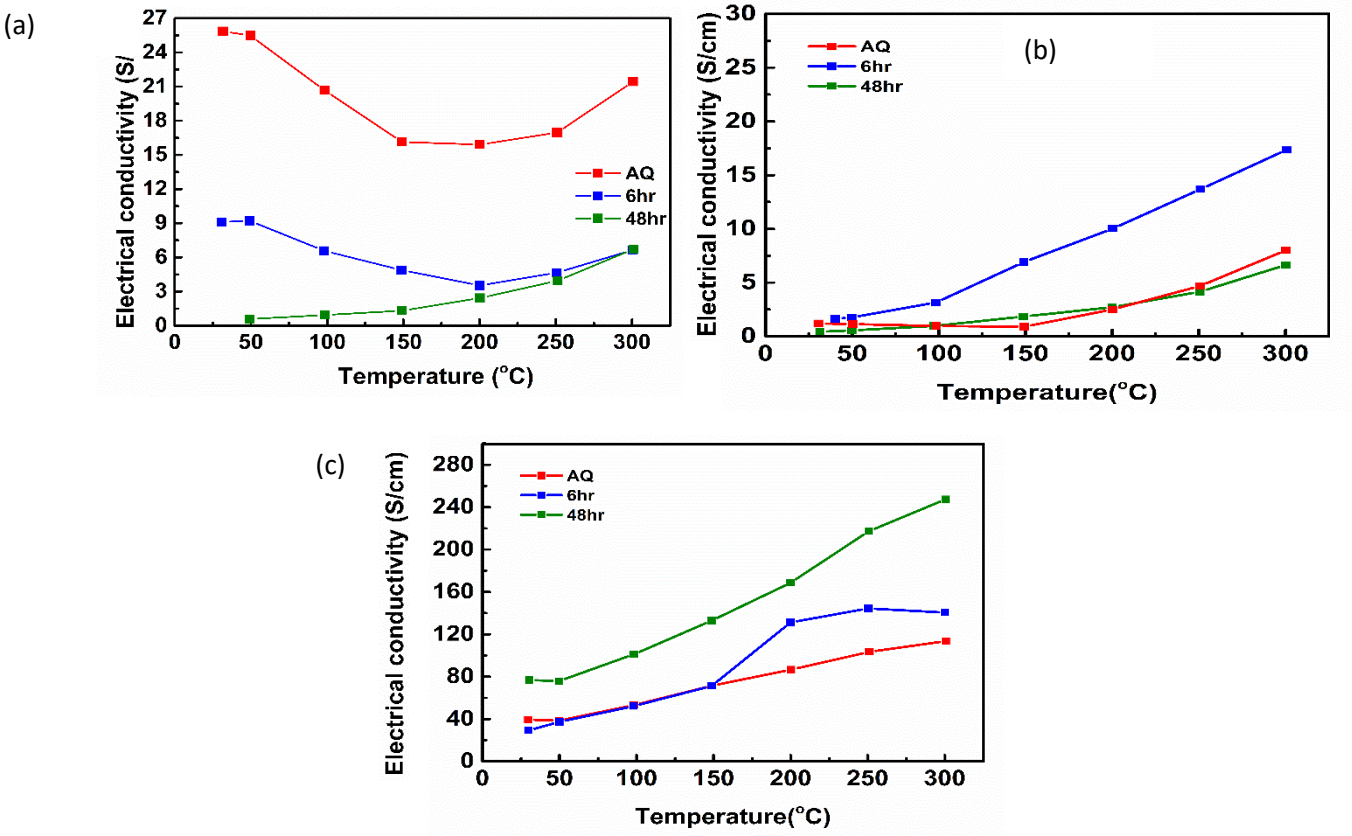

Figure 38 Electrical conductvity for different samples: (a) Bi-free samples, (b) 0.2 at% Bi, (c) 0.4 at.% Bi samples

6.5.2 Seebeck coefficient measurements

We measured the Seebeck coefficients for all of the samples, and the results are graphically represented in Figure 3938 for different aging times. It can be seen that the Bi-free sample exhibits positive Seebeck coefficients, except for 48h above 150 °C, where the sign becomes negative, implying a p-type polarity. The doped compounds possess lower values of the Seebeck coefficient compared to those of their undoped counterparts, due to increased charge carrier concentrations. Higher doping levels of Bi result in a change of polarity to n-type.

Figure 39 presents the Seebeck coefficient vs. temperature for each sample for different aging times. The trend of the Seebeck coefficient is opposite to that of electrical conductivity, as the S values increase with aging time for the Bi-free sample.

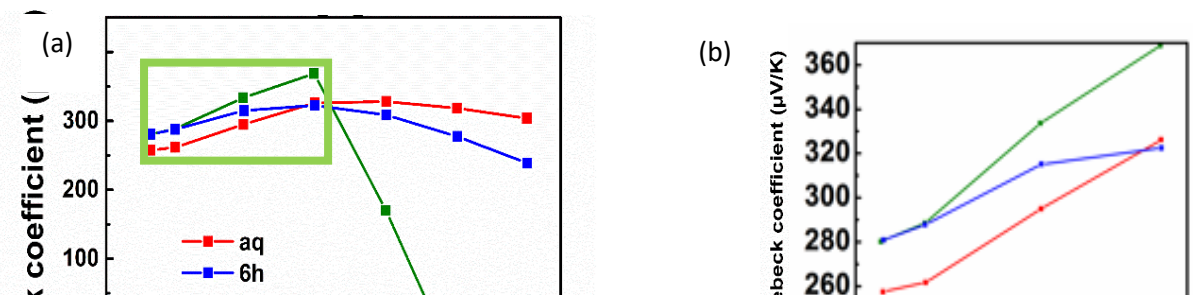

(d)

(c)

6.6 Materials Characterization

In order to be able to detect higher number densities, we employed TEM and APT, as these methods have atomic resolution, giving us the possibility to find lower-scale precipitates

6.6.1 TEM analysis

Figure 40 shows a TEM micrograph of the matrix and the precipitate in a dark field. The matrix is an FCC that allows limited diffraction planes, which is also seen in the DP. The Ag_2Te has a monoclinic structure with limited symmetry, hence many points are seen.

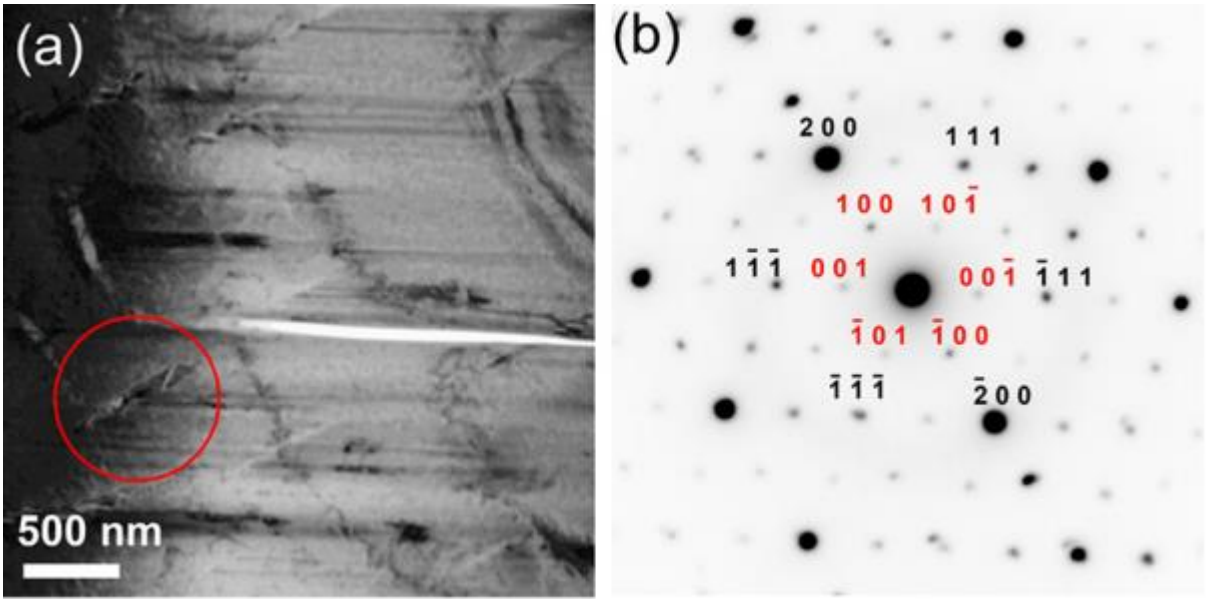

Figure 40 TEM micrograph of 0.4 at% Bi 48h in DF. (a) The matrix (PbTe) is gray and the precipitates have a dark contrast. (b) Diffraction pattern of the precipitate and matrix: the red marks represent the precipitate and black is the matrix. The orientation relationship is OR: $PbTe(100)[0\bar{1}1]||[100](010)\ Ag_2Te(monoclinic)$ Z.A: [011]

Figure 41 (TEM) and 45 (HRSTEM HAADF) show micrographs of 0 at % Bi AQ showing the precipitates in dark contrast with round shapes and a size range of 5-15 nm in diameter.

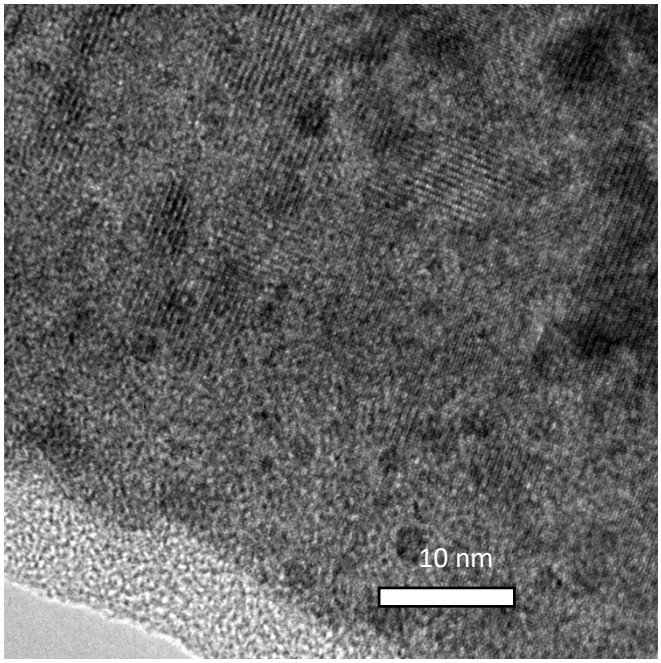

Figure 41 TEM micrograph of 0 at. % BI AQ, for Z.A of [011]

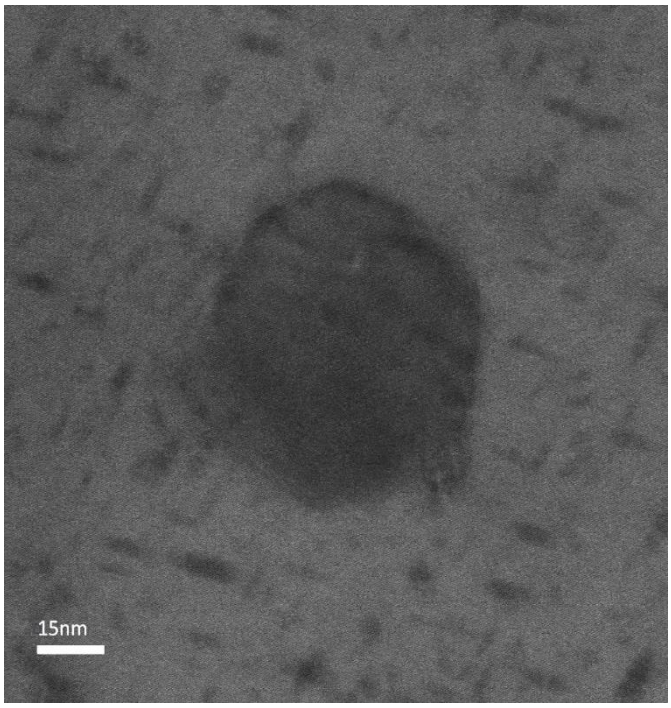

Figure 42 HRSTEM micrograph in a high annular angle dark field (HAADF) contrast of 0 at % Bi 48h showing precipitates in dark contrast with two different sizes, a big precipitate with a diameter of 45 nm and smaller ones with sizes between 10-20 nm.

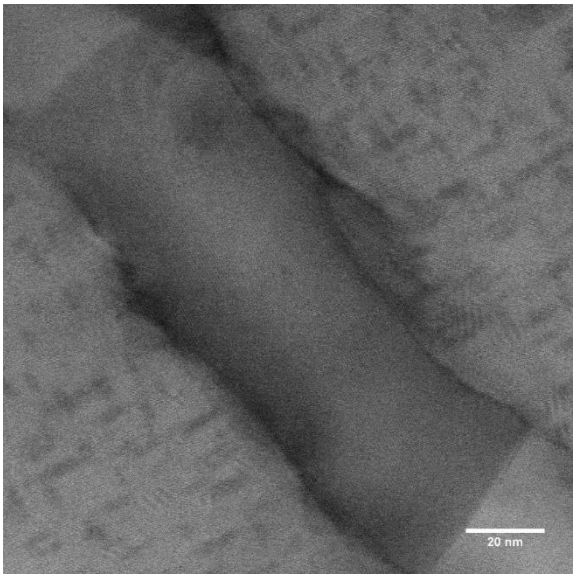

Figure 43 HRSTEM micrograph in high angle annular dark field (HAADF) contrast of 0 at % Bi 48h showing precipitates in dark contrast with two different sizes, a big precipitate the size of a couple of microns and smaller ones with sizes between 10-20 nm.

The TEM number density values are more qualitative than quantitative, as TEM is not a statistical tool; however, it can give an approximation of the actual number density, and we can assume that it describes the right order of magnitude.

N_v (m^{-3}) values were calculated using the TEM micrographs, and are listed below similar to the method used in the SEM specimens:

0 at. % Bi AQ: $(3.3\pm0.9)x10^{23}$

0 at.% Bi 48h : $(3.0\pm0.7)x10^{23}$

0.4 at.% Bi 48h : $(5.6\pm0.93)x10^{22}$

EDS analysis was performed for both precipitates, and the results are shown in Figure 44.

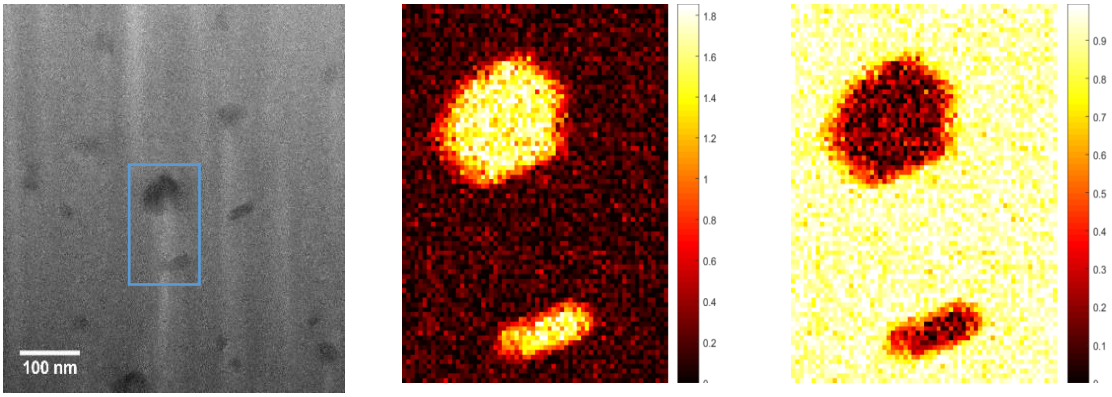

Figure 44 Area of the EDS from the 0 at.%Bi 48h on the left. In the middle is the EDS of the precipitates. Measurements range between 0 to 2, with the number indicating the silver content (Ag_xTe). On the right, the PB-Te ratio is presented

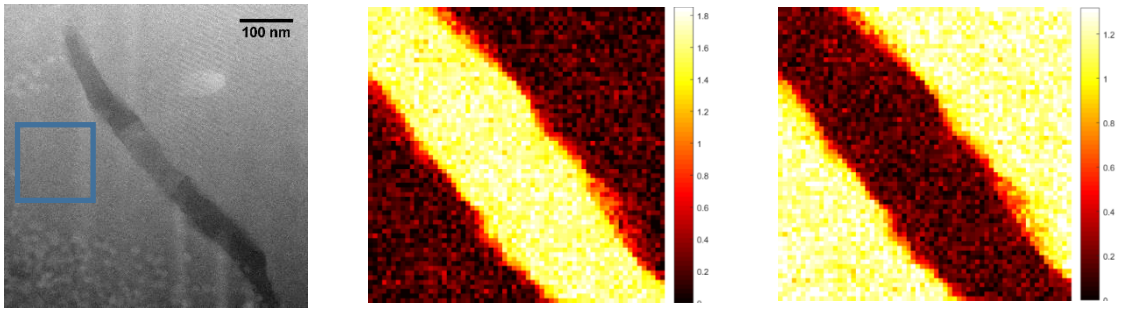

Figure 45 Area of the EDS from the 0.4 at.%Bi 48h on the left. In the middle the EDS of the precipitates, the measurements range between 0 to 2, with the number indicating the silver content (Ag_xTe). On the right, the PB-Te ratio is presented

The EDS shows us that the large precipitates indeed have an Ag_2Te stoichiometry. While the matrix has mostly PbTe, we can see that there are small areas with smaller concentrations of PbTe and higher concentrations of Ag, implying Ag_2Te-precipitates.

6.6.2 Atom probe tomography analysis

Using APT we can evaluate N_V more accurately, which can represent the real N_v values more accurately than ever before. For the rest of this work the Ag isoconcentration surface will represent the precipitates and the Te solutes (in green) will represent the matrix.

An example of the APT tip specimen is shown in Fig. 49.

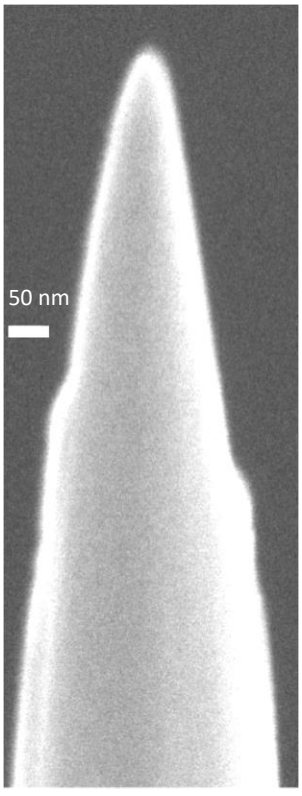

Figure 46 SEM image of the tip used for APT, sample 0 at.% Bi 6h

Figure 47 shows a typical mass spectroscopy for our system. We usually detect all isotopes for each atomic specie; however, for the Bi-doped samples, the Bi peak overlaps the thermal tail of one of the Pb-peaks, which makes it impossible to analyze the distribution of Bi-atoms.

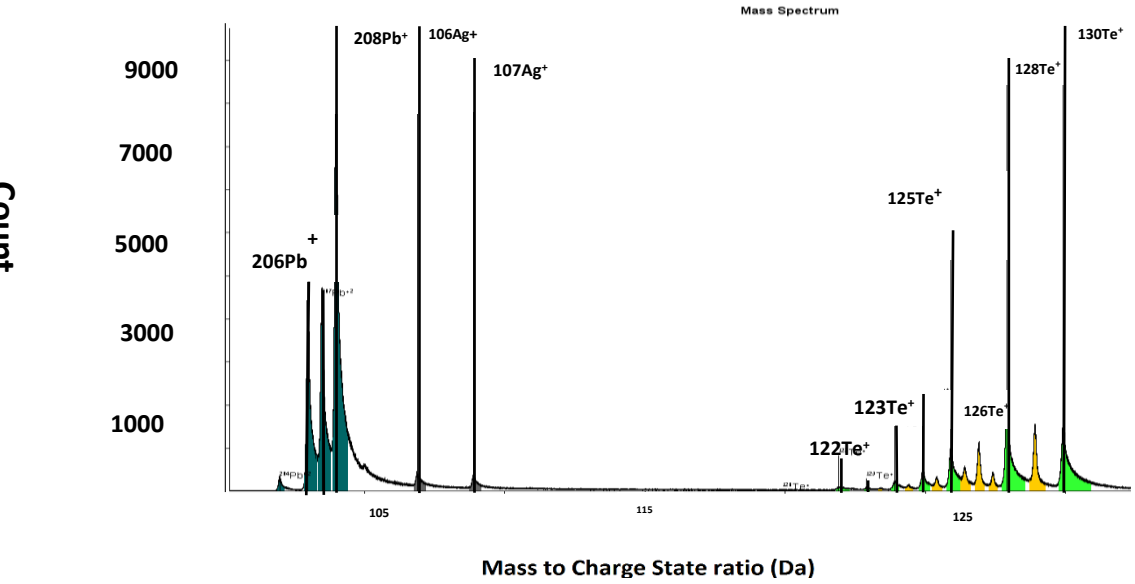

Figure 47 Mass spectrum ranges of PbTe and Ag, taken using APT of the Bi-free sample

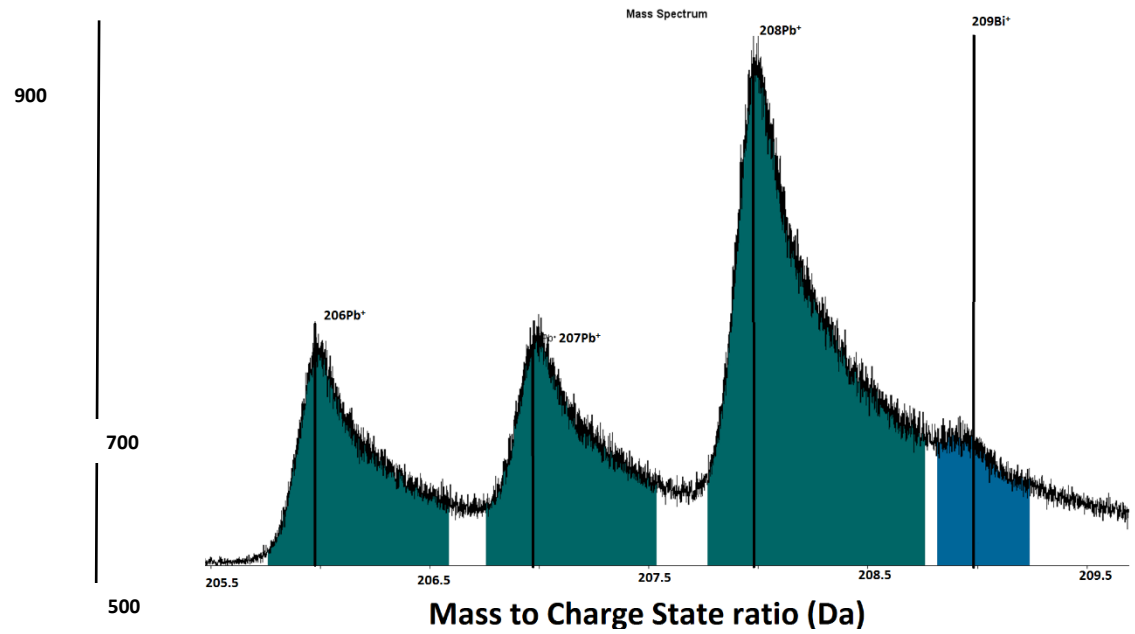

Figure 48 Close-up of the mass spectroscopy for an area that shows the overlap between the Pb and Bi peaks

In order to have an accurate quantitative measurement, we needed to assign the right isoconcentration surface, which was chosen using a correlation with the TEM micrographs. To this end, we apply Figure 42 and Figure 43 to choose the right values, by comparing the sizes of precipitates with the APT reconstructions.

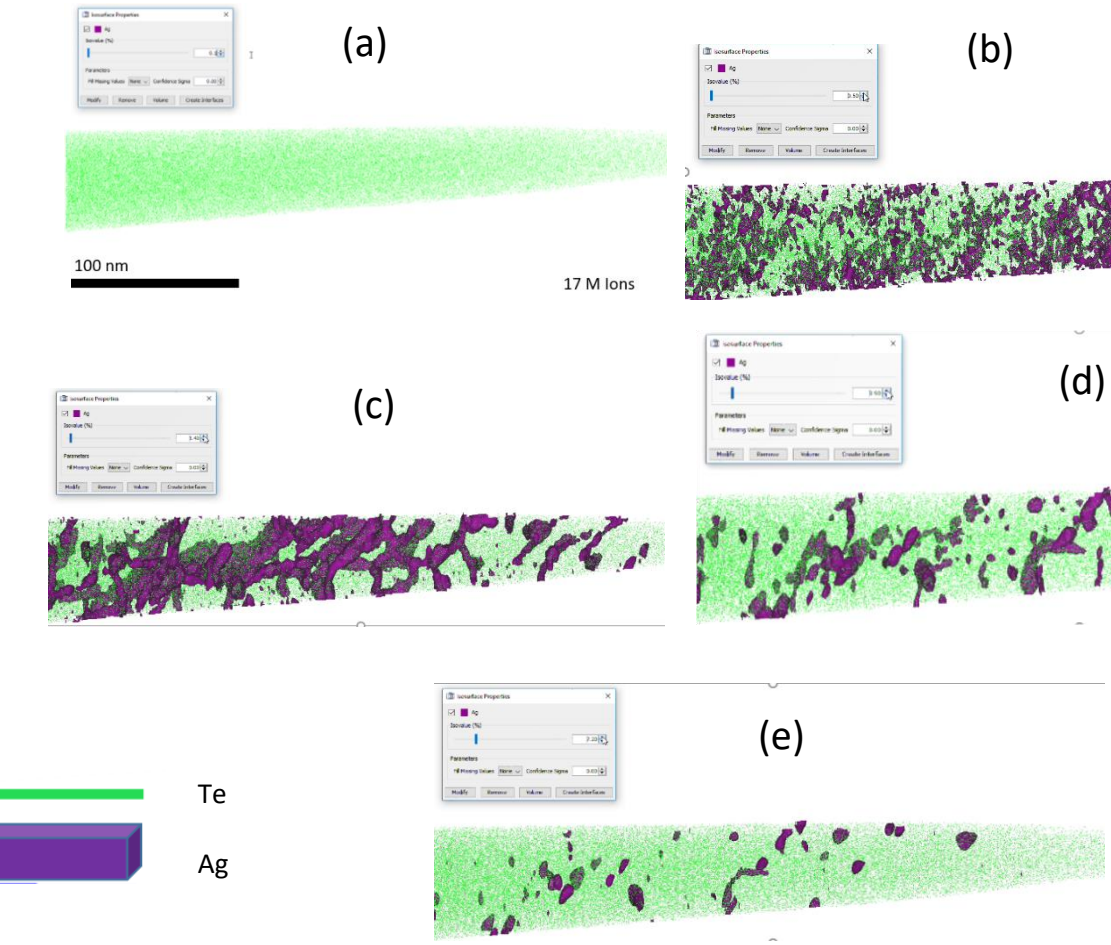

Figure 49 APT reconstruction of 0. at % Bi 48 hr for different isoconcentration surfaces, ranging from 0 at. % Ag to 8 at. % Ag (a is the lowest and e has the highest values)

When the isoconcentration value is 0% there is no isoconcentration surface. After we set the value to 0.5 at. %Ag, we notice that there are many surfaces that also intertwine with each other, so the probability of having a surface with 0.5% Ag is relatively high. The higher we raise the value of the isoconcentration surface, the less the probability of obtaining an isosurface, until almost no precipitates are found for higher concentrations, and only large precipitates can manifest, at a low probability. This illustrates that in order to assess N_v, the right isoconcentration value must be chosen carefully. This was achieved by comparing the APT reconstruction with the respective TEM micrographs of each specimen and assessing the size of the different precipitates, followed by averaging the small precipitate sizes in the reconstruction.

An illustration of this method is presented in Fig. 51.

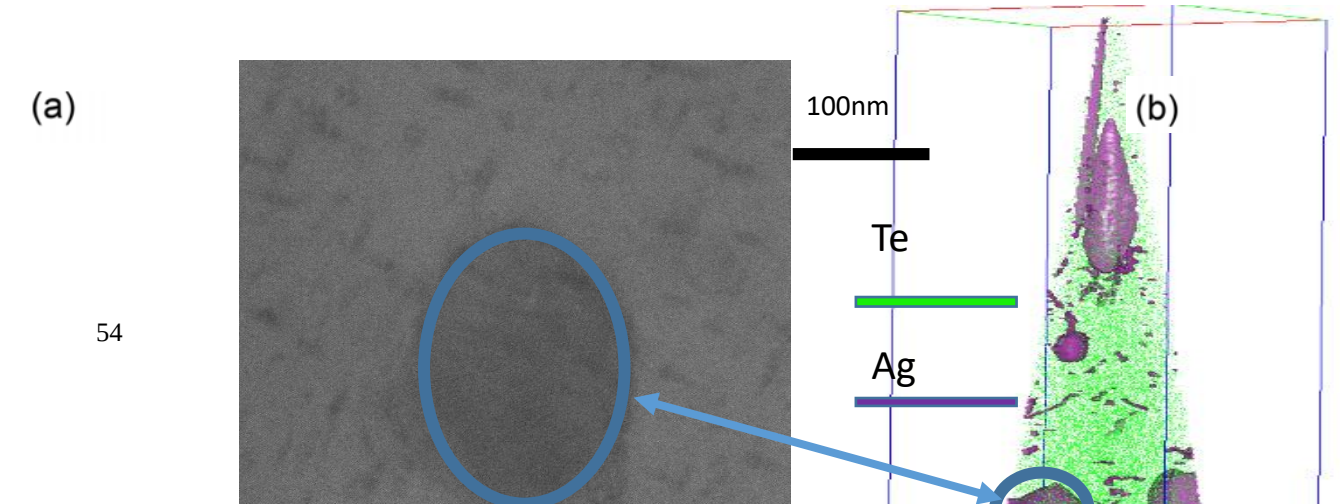

Figure 50 (a) HRTEM micrograph and (b) APT reconstruction of 0 at. % Bi 48 hr. The large precipitate is marked blue and the small precipitates are marked red. After matching the isoconcentration surface of the reconstruction to the micrograph, were we able to calculate the Nv. In this figure, the Ag % isoconcetration is 2 at. % Ag

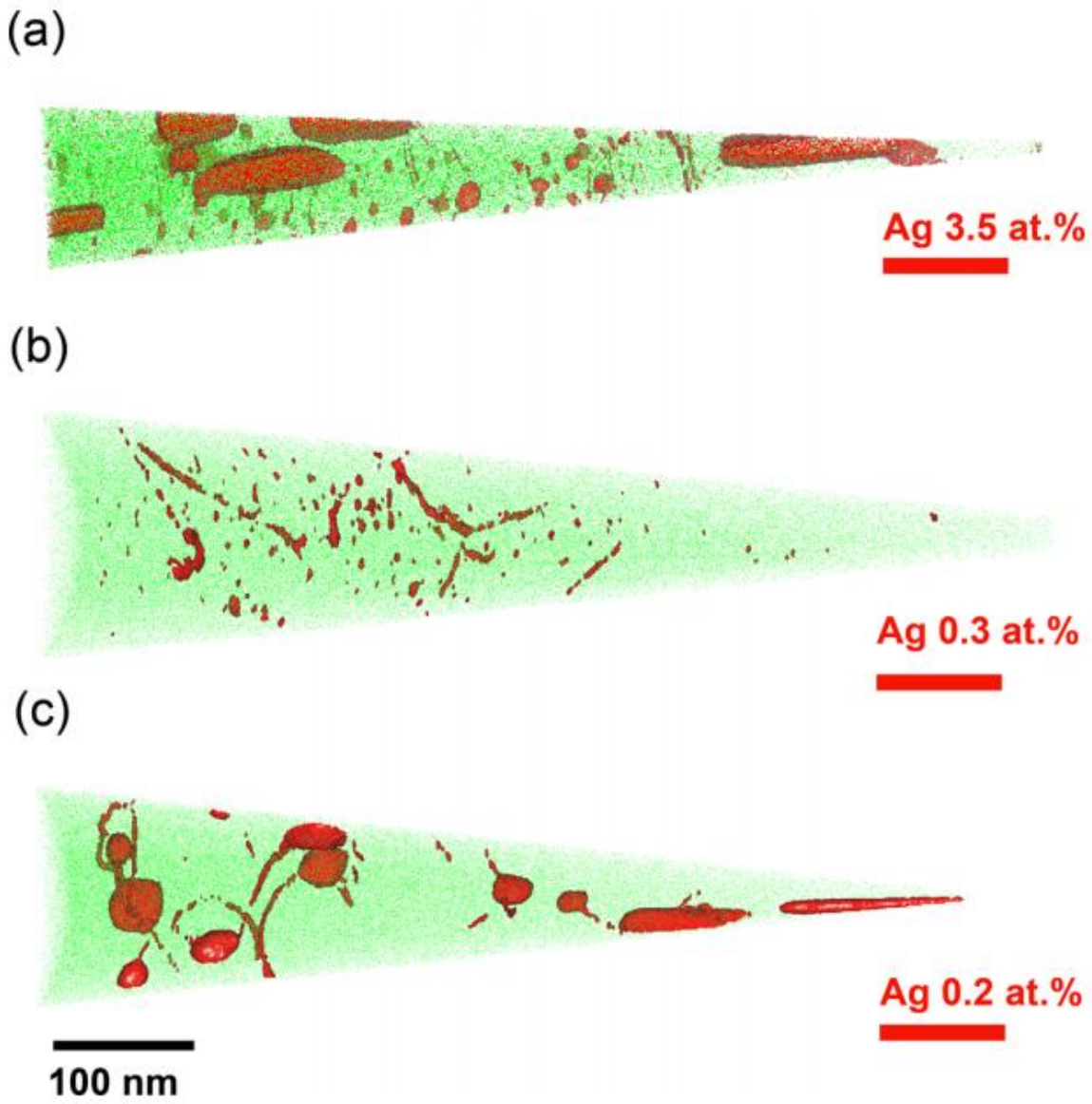

Figure 51 Three-dimensional (3D) atom probe tomography (APT) reconstructed volumes acquired from the (a) as-quenched (AQ) alloy and those aged for (b) 6 h and (c) 48 h. For clarity, only the Te ions are marked (green dots). Ag-rich precipitates are indicated by isoconcentration surfaces, marked in red, with Ag concentration values marked in red.

Figure 52 shows the evolution of the precipitation of the Bi-free samples. We can see that at first there is a relatively large amount of large Ag precipitates (hundreds of nanometers in radius) and almost no small precipitates (smaller than 30 nm in diameter). After brief heat treatments, the large precipitates are almost entirely gone, while smaller precipitates appear, suggesting that they are used for the precipitation. Finally, after 48 h, the large precipitates reappear at the expense of the smaller precipitates. This confirms our hypothesis of supersaturation of Ag after quenching, followed by precipitation and, at last, coarsening.

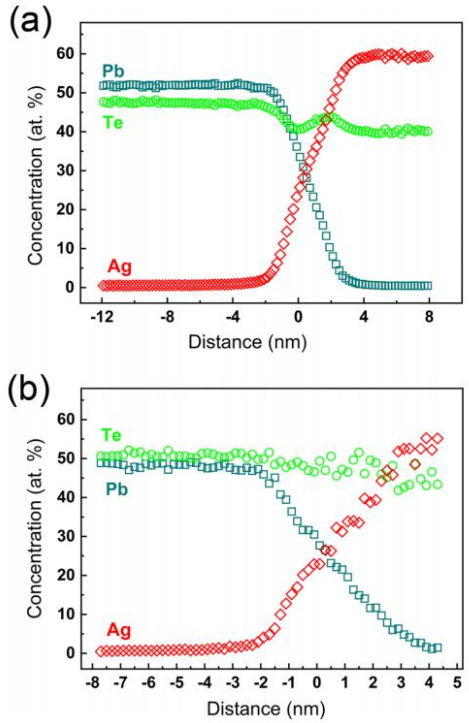

Figure 52 Typical proxigrams acquired across the interfaces between (a) large and (b) small Ag-rich precipitates and the PbTe matrix of the as-quenched (AQ) sample, indicating a difference in the Ag/Te stoichiometry of the precipitates.

Interestingly, the large precipitates show the stoichiometry of Ag_2Te, which is the expected stoichiometry. However, the smaller precipitates have a stoichiometry of 1:1; apparently, the “unmatured” precipitates did not have enough time to age and reach equilibrium values.

Figure 53 shows a zoomed-in reconstruction where the isoconcentration surfaces were chosen and a region of interest (ROI) where no precipitates are present, allowing us to measure the matrix composition in the ROI.

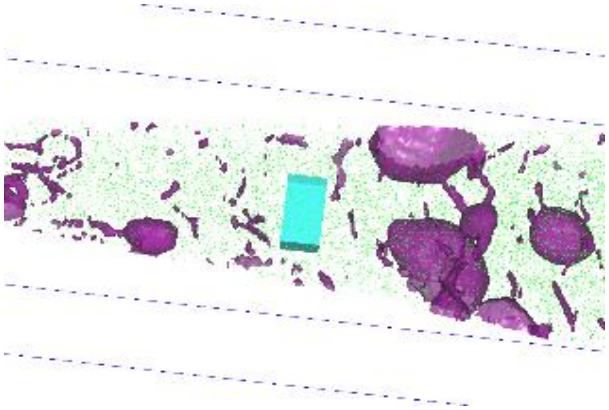

Figure 53 APT reconstruction close-up for 0 at. % Bi 48h

The precipitates' number densities were calculated for the 0 and 0.2 at.% Bi samples, and are shown in Figure 54.

0: (AQ)- $(3.61 \pm 1.51) \times 10^{21}$

6: $(1.68 \pm 0.92) \times 10^{24}$

48: $(1.21 \pm 0.75) \times 10^{22}$

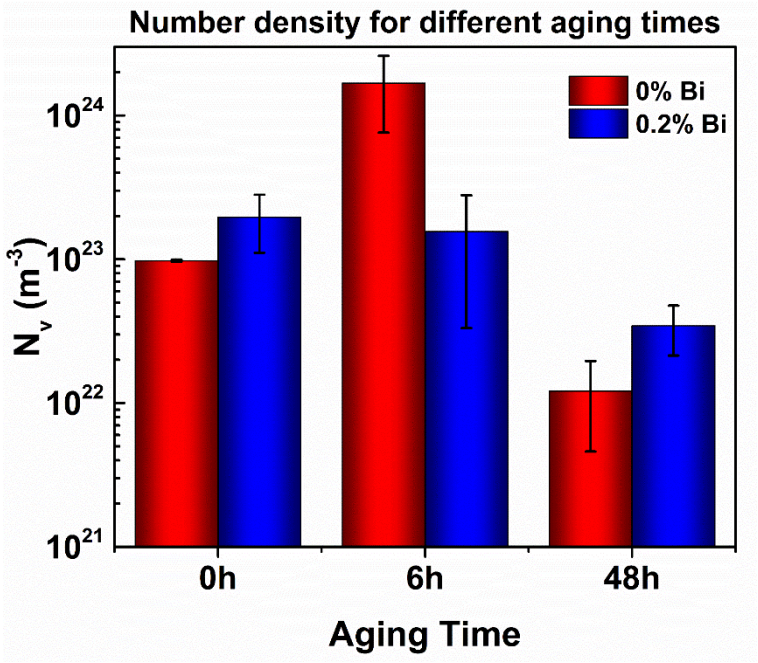

Figure 54 Nv vs aging time for specimen 0 at.% Bi (red) and 0.2 at.% Bi (blue) using the APT data

These number density values were obtained due to the use of complimentary microscopy with TEM micrographs as a reference for a more accurate realization of the precipitates. The precipitates were counted after choosing the desired isoconcentration surface; given the volume of the cube we measured, we were able calculate the Nv.

The matrix concentrations of 0 at. %Bi are presented in table 4:

Table 4 Matrix concentration at different aging times of 0 at.% Bi

Aging time [h]	**Pb**	**Te**	**Ag**
0	44.88 ± 0.23	54.33 ± 0.23	0.78 ± 0.04
6	40.94 ± 0.26	58.47 ± 0.26	0.62 ±0.04
48	39.67 ± 0.25	59.24 ± 0.24	0.62 ± 0.04

6.6.3 Process optimization

The previous research conducted in our laboratory utilized temperature optimization, to find which temperature can yield the best performance. These experiments were conducted in 450, 400, and 380^{O}C. The best results for TE properties were found at 380^{O}C.

There is a competition between diffusion, or precipitate growth, and nucleation energy formation. On one hand, we want a high supercooling temperature in order to have a strong driving force for nucleation. On the other hand, we want the precipitates to grow, which requires low supercooling or higher temperatures. Here, we wanted to find out if 380^{O}C annealing is indeed the process temperature with the best yield. In previous experiments we only aged for 6 h or 48 h; however, due to the lower temperature we also annealed for 10 h as a median time. The thermal conductivity of the 370^{o}C experiment is presented in Fig. 57:

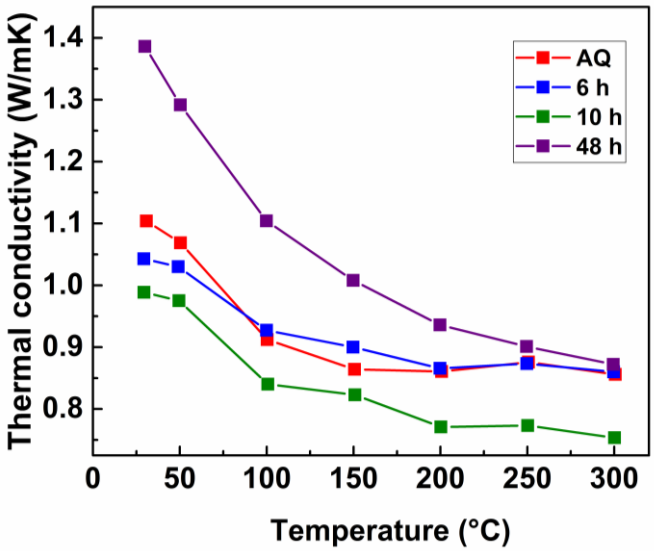

Figure 55 Thermal conductivity for different aging times at 370ºC for the Bi-free sample

The 10 h Bi-free specimen appears to have reached a lower TC than the 380ºC counterpart.

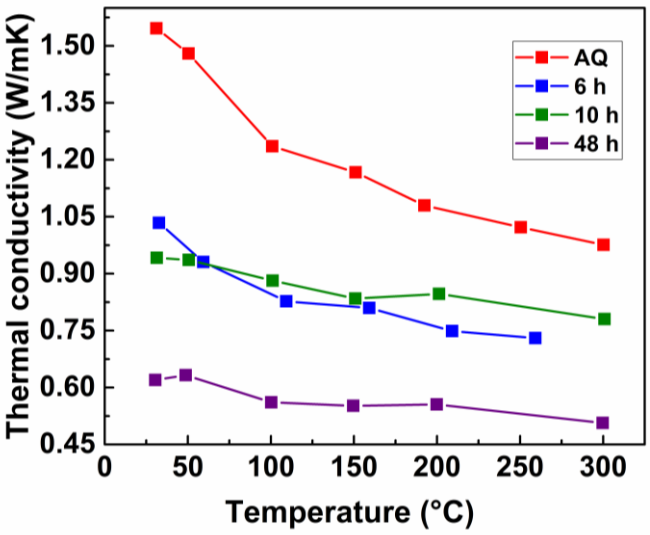

Figure 56 Thermal conductivity for different aging times at 370ºC for the 0.2 at.% Bi sample

6.6.3.1 Electrical properties

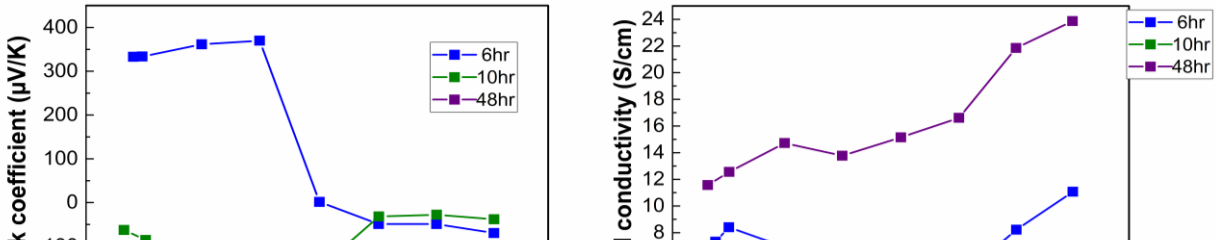

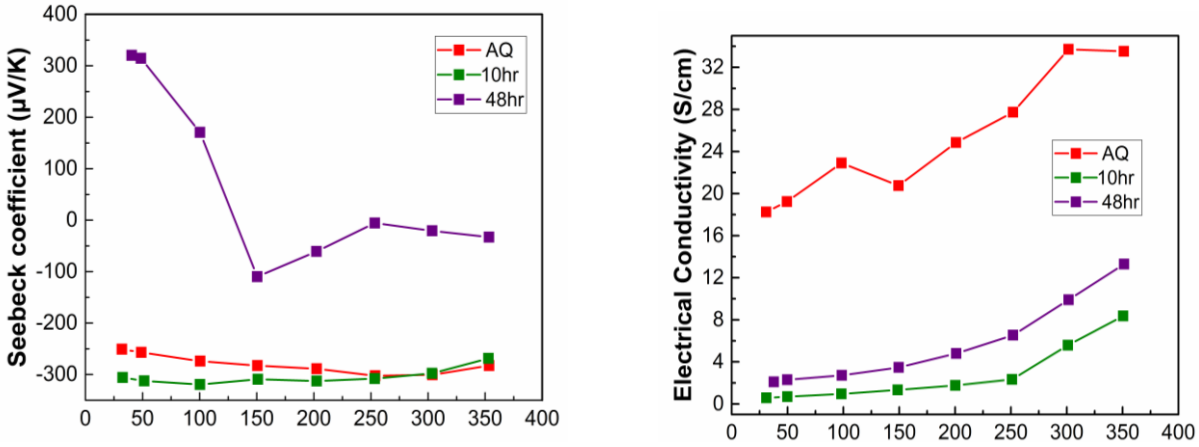

Figure 58 Seebeck coefficient of the 0.2 at. % Bi sample at different aging times for 370oC (left), electrical conductivity on the right

6.6.3.2 Microstructure evolution

The TE properties share similar results with their 380^{O}C counterpart. For the 0% Bi, we see a decrease in thermal conductivity for short thermal treatments and higher TC for longer treatments. The thermal conductivity of the 0.2 at. % Bi decreases monotonically with time and is much lower than the 380^{O}C counterpart, a phenomenon that merits further investigation. The electrical properties are similar to our previous research, showing a "more" n-type behavior for the Bi-doped specimen.

6.6.3.3 Microstructure evolution

Similar to section 6.3, we inspect the microstructure and count the precipitates to obtain the Nv and ultimately find the connection between the microstructure and the TE properties:

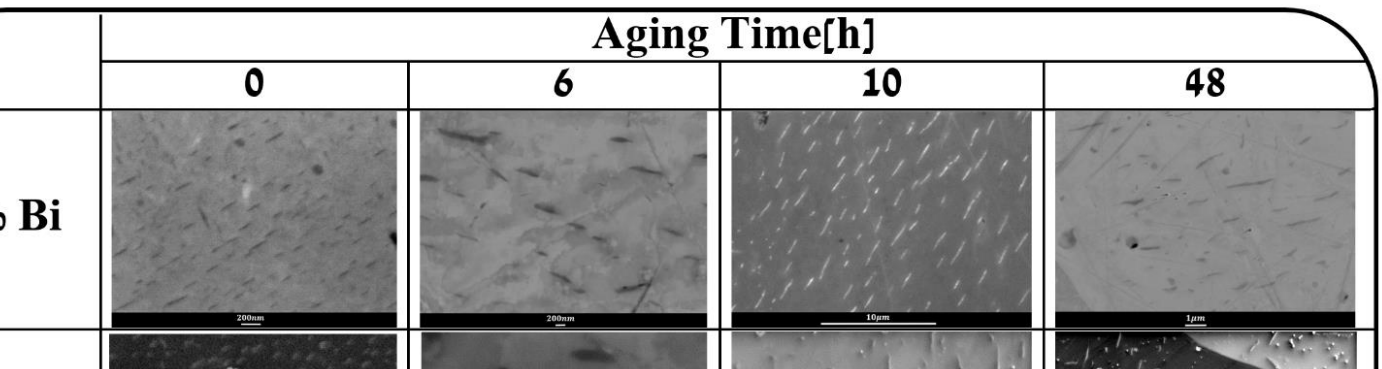

Figure 60 SEM and FIB micrographs of the samples. Precipitates have dark contrast in SEM images and bright contrast in the FIB images

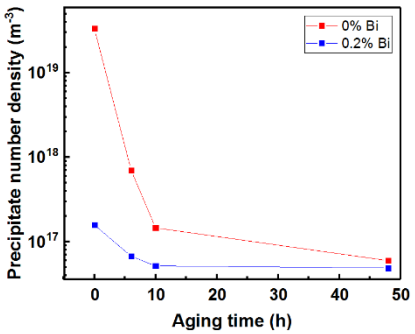

Figure 61 N_V of the samples for the 370ºC annealing temperature

The number density using the SEM micrographs does not exhibit the same correlations we found with the 380^{O}C treatments, as the N_V here shows coarsening. However, we have seen that the SEM micrographs do not show the whole picture, as there are nano-precipitates that we cannot detect.

7 DISCUSSION

7.1 TE measurements

7.1.1 Thermal transport properties

The heat capacities calculated in Figure 30 to 33 **Error! Reference source not found.**along with thermal diffusivity enable us to calculate the thermal conductivity of each sample by applying equation (9). We could calculate the thermal conductivity shown in Figure 35. We calculated κ_e using the electrical conductivity show in Figure 38 and equation(12). By deducing κ_e from the total thermal conductivity, we deduced κ_l.

The temperature-dependent thermal conductivities measured show, at first, a sharp decrease of values until ~150 °C; then, a moderate decrease until 300 °C. The first stage can be attributed to the Umklapp phonon scattering process, in which the lattice thermal conductivity is proportional to $1/T$ (equation (15)) at temperatures adequately higher than θ_D. We can see that for the Bi-free sample and the 0.2 at. % Bi sample there is a decrease in thermal conductivity for brief aging times, and then for the longer times we observe an increase of TC even above the initial values. At first, the supersaturated matrix with Ag acts as a phonon scattering points. After several hours of aging, the N_V is high enough to scatter the phonons better than the initial state. After lengthy aging times, the Ag is completely consumed (up to the solubility limit) and coarsening occurs, leading to an increase of TC. The strains and defects of the matrix are also healed due to the heat treatments, all of which results in a higher TC. It can be inferred from this scenario that the effects of nanoscale precipitates are comparable to that of elastic strain fields. As a side effect, small precipitates induce a high degree of coherency strain fields into the matrix; however, as the precipitates grow, they lose their coherency, which leads to strain relief. This result is similar to results previously observed in our laboratory and published[40]:

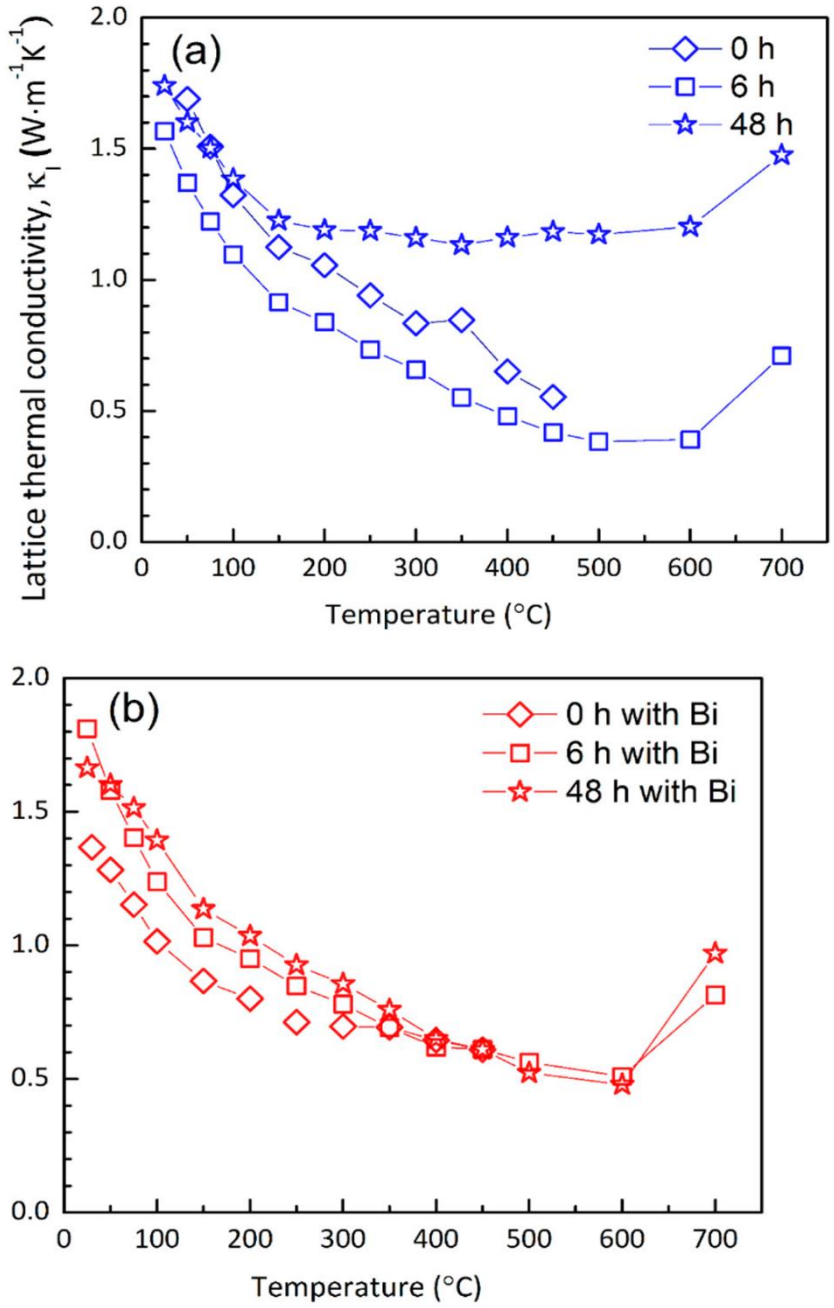

Figure 62 The temperature-dependent lattice thermal conductivity values evaluated from the measured thermal and electrical conductivities, after applying the Wiedmann-Franz relationship to the HP series of specimens, for specimens aged at 380 °C for 0 h (diamonds), 6 h (squares), and 48 h (stars). (**a**) Bi-free (blue symbols) and **b**) Bi-alloyed (red symbols)

Bi inhibits the precipitates' growth and the effects of precipitation, i.e, the TC is higher overall, and the electrical properties are enhanced. Thermal conductivity is higher as the Bi concentration increases; we can also see that the electronic part of TC is much higher for the 0.4 at. % Bi than for the Bi-free sample (Figure 36). We can see in Figure 36 that the lattice component is the dominant part of the TC for the Bi-free sample.

7.1.2 Electrical properties

Generally, all samples exhibit an inverse relation between σ and S, i.e., as one increases the other one decreases, which is expected (eq. 3). The Bi-free sample shows a decrease in EC with temperature while the Seebeck coefficient increases. As the aging time increases, the Ag that helps with conduction is consumed for precipitation and thus the EC decreases. Above 150ºC there is enough thermal energy to excite electrons and increase the EC; this change is visible as the polarity changes from positive to negative (shown in Figure 39) due to the high electron concentration. The EC was not as high as expected, as the densities for the low-yielding EC materials are not very high (Table 3).

0 at. %Bi has low bulk density. The 0.2 at. % Bi sample is a p-type semiconductor at first, and as the aging time increases the material assumes more of n-type behavior until it becomes solely n-type. At first we have a competition between both dopants: the Ag acceptor (p-type) and the Bi donor (n-type). When the Ag is consumed for precipitation, the co-doping levels are diminished and Bi becomes the main dopant, resulting in n-type behavior. The Ag atoms act as electron acceptors for temperatures up to 150 °C and for the current Ag concentration range, resulting in positive S coefficients. The Ag atoms are consumed by Ag-rich precipitates during their nucleation and growth; their average concentration in the PbTe matrix decreases with aging time, resulting in a reduction of the electrical conductivity and increase in |S|. The behavior of the sample aged for 48 h shows a very low electrical conductivity with a positive S-coefficient that changes its sign to negative upon heating. This can be explained by the transition from p- to n-type polarity, which occurs because the volume fraction of Ag2Te is the greatest after 48 h aging, so that the amount of Ag atoms dissolved in the PbTe matrix is the smallest.

The samples containing Bi have a higher EC overall, and the 0.4 at. % Bi sample is significantly higher. At the same time, the Seebeck coefficient becomes more and more negative as the relative Bi concentration increases. The Bi undermines the Ag in terms of electrical properties, making these samples n-type semiconductor from the start.

7.2 Microstructure evolution

Identification and comprehension of the phase transformation mechanisms and discovering the governing dynamics of microstructural evolution is one of the most important subjects in materials science, enabling us understand the relationship between the microstructure evolution and TE properties.

Phase transformations in materials are determined by both thermodynamic and kinetic contributions. For the description of precipitation from a supersaturated matrix, the equilibrium compositions of the different phases must be determined first. Then, the rate of transformation depends on the energy gain due to nucleation

(ΔG), interfacial energy (γ_s), and elastic energy variation. In addition, the diffusion coefficients of the constituents that are involved in the transformation, D_a, should be determined.

Figure 28 shows the N_v values measured using the HRSEM and FIB micrographs. These results may explain the trend of the TC, as the N_v increases for short aging times due to precipitation while the TC decreases; for longer times we have an increase in TC and a decrease of N_v, as coarsening occurs. We also notice that the Bi-free sample has an overall higher N_v for all of the aging times. However these values are rather small, the highest value being ~10^{19} [m^{-3}], which is a number that is not high enough to affect phonon waves.[20] The desirable number density should be above 10^{20}, which could be achieved using APT, where we can detect smaller precipitates than HRSEM, resulting in an estimation of N_v to 10^{25}.

In the case of materials containing a high density of precipitates, the usual way to determine microstructural parameters such as shape, size, precipitate number density, and volume fraction is by visual estimation. To calculate precipitate compositions, the user selects a volume around each region in the 3-D atom map that is considered a precipitate. The process of selecting the desired region in three dimensions can be difficult, especially in the case of non-spherical, needle-shaped, or diffuse precipitates, and will generally introduce some matrix atoms, leading to errors in the subsequent composition calculations. Accordingly, we correlated the HR-TEM micrographs to find the actual size of precipitates and perform the N_v evaluation more accurately.

The diffraction pattern of the precipitate shows that they are in a monoclinic phase. The precipitates seen on the HRTEM are much smaller than those seen on the HRSEM or TEM, and can be separated into 2 types. The first consists of larger precipitates between 50 to 100 nm in diameter (in the Bi-free case) and up to several microns in the 0.4 at. % Bi case. The second is nano-precipitates with a diameter of ~10 nm (Figure 42, Figure 43). The EDS of the larger precipitates affirms that the stoichiometry of the larger precipitates is indeed Ag_2Te; however, the small precipitates were too small to determine. By using these sizes seen in the HRTEM we could find the right conditions for the APT reconstruction and isoconcentration surface values adjustments.

The stoichiometry of the nano-precipitates was measured using the proxigram, which showed that they have a 1:1 chemical stoichiometry. This is not a thermodynamically stable phase[55], although this may be achieved as they are nano-sized particles and can form a metastable form when quenching occurs.

In Figure 54 we notice the same increase in the N_v of the Bi-free sample for short aging times due to precipitation and a decrease after longer times. This agrees with the TC of this sample, as it decreases with shorter times and increases for 48h. The 0.2 at. % Bi N_V sample shows similar behavior. However, this is not visible at first glance in Figure 54. To understand the behavior in this figure we need to examine Table 4, which shows the isoconcentration values when counting the N_v. We can see that the AQ samples values are

much lower than the 6 h and 48h counterparts. The lower the number density, the lower the threshold for forming a surface, which makes the surfaces much higher. Therefore this number should not be taken as the real number when comparing each result.

The N_v shown in Figure 54 for the AQ sample is actually lower than what we measured, and the isoconcentration surface of the AQ sample is much lower than the 6h and 48h samples. If we would have wanted to compare them we would have required the same isoconcentration surface, but these were the best isoconcentration values that could be achieved. To be able to compare we need to understand that if we would have higher isoconcentration surface values the N_v would decrease, so the effective N_v, although not known exactly, is lower than what we measured. If we consider this explanation, then we see the same behavior as the 0 at. % Bi sample: an increase in N_v followed by a decrease. We also notice that the N_V of the Bi-free sample is higher than the 0.2 at. % Bi. This is in agreement with our hypothesis that Bi inhibits the precipitation growth; however, it is as yet unclear how, exactly, Bi inhibits the process. There are results for the 0.4 at.% Bi; the 6h sample has not been measured yet. The EC is affected by the Ag content in the matrix, as the supersaturated Ag enhances the EC (in the Bi-free case—in the Bi samples it interferes with it). Afterwards, the Ag is diluted from the matrix due to precipitation and the EC rises. For longer aging times, the Ag content does not change much, which suggests that coarsening occurs, and the behavior of the electrical properties corresponds to the matrix's Ag content (Figure 38). There is a convergence of the EC at temperatures above 150˚C, when there is enough thermal energy to excite electrons, as the compound has a relatively low band gap.

7.3 Process optimization

7.3.1 HP optimization

We want to improve the overall electrical conductivity by having a denser material. For this purpose we performed HP optimization and correlated the density with the EC. Figure 16 presents the density of the specimen for different times and pressures; the best density was measured for 50 MPa pressure at 15 min. Figure 17 demonstrates the stated correlation: the higher the density, the higher the EC.

7.3.2 Aging temperature

The precipitation process is a competition between the diffusion and nucleation rate: if the annealing temperature is high, diffusion rates will be high and the driving force for nucleation is low; if we lower the supercooling level, we increase the driving force but diffusion rates are low. Thus, there is a temperature in which both mechanisms compromise and we achieve the best rate for precipitation. The size of precipitates also changes due to the temperature: if we have high diffusion rates we obtain a low number of them and large grains/precipitates; when the supercooling temperature is high we obtain a high number of precipitates and

they are much smaller[35]. To date, we examined the following temperatures in our laboratory: 450°C, 400°C, and 380°C[40]. The first two temperatures were too high, showing a low number density and immediate coarsening. The third (380°C) was further examined in this research. We also want to examine other temperatures, in the search for the optimized annealing temperature. In this part we discuss the heat treatments of our specimen at 370°C:

In Figure 55 Thermal conductivity for different aging times at 370oC for the Bi-free sample) and Figure 56 Thermal conductivity for different aging times at 370oC for the 0.2 at.% Bi sample) we present the thermal conductivity of the Bi-free sample and the 0.2 at. % Bi sample, respectively. The Bi-free sample behaved similar to the 380°C counterpart, with similar TC values. However, when we examined the N_V (Figure 56 Thermal conductivity for different aging times at 370oC for the 0.2 at.% Bi sample) it decreases monotonically, contrary to our previous results. Notably, these results were only achieved by SEM imaging, which we have already proved is insufficient to measure N_V. The more interesting result was for 0.2 at.% Bi, where the TC decreases monotonously and reaches a very low TC for 48 h aging time[56,57].

The electronic properties have some missing samples: The Bi-free samples are missing the AQ data, and show a polarity change for longer hours. We can see that above 150°C the thermal energy for exciting electrons has a role here as well.

8 SUMMARY AND CONCLUSIONS

We performed an analysis of the microstructure and TE properties of $Pb_{0.967}Ag_{0.33}Te$ with or without Bi doping (0.2, 0.4 at. %Bi). The materials were fabricated by mixing pure elements in the appropriate stoichiometric ratios, and annealing at 380 °C in an Ar-H2 atmosphere after grinding and hot pressing of the ingots. The specimens were characterized by XRD, HR-SEM, LFA, SBA, and HR-TEM along with APT. We measured the temperature dependence of the Seebeck coefficient, electrical conductivity, and thermal conductivity, and correlated the TE properties to the obtained microstructure; in particular, the Ag2Te precipitate number density, Nv, in a quantitative manner.

Our investigation of Ag2Te precipitation in Bi-doped and undoped $(PbTe)_{1-x}(Ag2Te)_x$ compounds reveals an evolution in number density. The nanoscale Ag2Te precipitates had a spherical morphology. For larger sizes, Ag2Te precipitates are observed as ellipsoidal disks aligned along certain directions in the PbTe matrix. Finally, in lengthy aging treatments, a coarsening process begins. This morphological evolution is consistent with the known competition between elastic misfit energy and interfacial free energies at the matrix/precipitate interface.

The complementary microscopy of APT and TEM shed light on the connection between the microstructure and the TE properties in a quantitative matter, with the N_v reaching up to 10^{24} m^{-3} for the 6h Bi-free sample. Although Bi inhibits precipitation it redeems itself with an increase in the EC.

Our main findings can be summarized as follows:

i. We reduced the thermal conductivity of PbTe by controlled nucleation of Ag2Te-precipitates. The controlled nucleation was implemented by a combination of several factors, such as choosing the appropriate sample preparation method and heat treatment at a temperature that is high enough to enable an adequate diffusion rate, while low enough to provide an adequate degree of supercooling. An additional factor that was tuned is the appropriate Ag concentration in the PbTe matrix.

ii. We tracked the microstructure evolution in terms of nucleation, growth, and coarsening, and showed how it correlates with TE properties, such as Seebeck coefficients and electrical and thermal conductivities.

iii. For the first time, there is a quantitative support for the change in TE properties due to microstructure. This was achieved using a thorough APT analysis of the samples for the different annealing times and observing the changes in the microstructure throughout the different times.

Notwithstanding the research results, some unanswered questions remain. For example, it is unknown how the kinetics of precipitate growth affect the TE properties. Using n-situ heat treatments with TE property measurements, we would examine how the precipitation and coarsening of our material affects the TE properties. Another question is how come the stable phase of Ag2Te is α, yet we get a β phase with a monoclinic structure? Also, how does the bismuth behave during the heat treatment? In-situ heat treatments in TEM can show the microstructure evolution, and if we can thoroughly understand the micro/nano-structure evolution with time, we can "fine tune" our process and find the most optimized process, as well as understand the mechanism of precipitation and maybe see the effects of the bismuth on the growth and how it inhibits the precipitation mechanism. Further investigation of the 370°C heat treatments using TEM and APT is also merited, as the 370^{O}C anneal process showed very low thermal conductivity, while retaining a relatively high EC.

This was merely an initial research, and was conducted using only HRSEM, which does not provide the whole picture—we showed that to calculate the Nv values we need to utilize advanced microscopy at higher resolutions. This research's aging times were restricted to 6, 10, and 48 h—additional times may yield better results.

9 REFERENCES

1. Franz, R. & Wiedemann, G. Ueber die Wärme-Leitungsfähigkeit der Metalle. *Ann. Phys.* **165,** 497–531 (1853).
2. Altenkirch, E. Über den nutzeffekt der thermosäule. *Phys. Zeitschrift* **10,** 560 (1909).
3. FedorovichIoffe, A. ПоЛУпроводниковЫе термоЭЛементЫ. *Москва-Ленинград* **АН,** (1960).
4. Auparay, N. Room Temperature Seebeck Coefficient Measurement of Metals and Semiconductors. (2013).
5. Aimé., W. Problèmes Et Calculs Pratiques D'électricité. *Gauthier-Villaes Fils* **1883,**
6. Fritzsche, H. & H. A general expression for the thermoelectric power. *Solid State Commun.* **9,** 1813–1815 (1971).
7. Drebushchak, V. A. The Peltier effect. *J. Therm. Anal. Calorim.* **91,** 311–315 (2008).
8. Rowe, D. M. *Thermoelectrics handbook : macro to nano*. (CRC/Taylor & Francis, 2006).
9. Ashcroft, N. W. & Mermin, N. D. Solid State Physics. *Solid State Physics* **2,** 848 (1976).
10. Chester, G. V & Thellung, A. The Law of Wiedemann and Franz. *Proc. Phys. Soc.* **77,** 1005–1013 (1961).
11. Kim, H.-S., Gibbs, Z. M., Tang, Y., Wang, H. & Snyder, G. J. Characterization of Lorenz number with Seebeck coefficient measurement. *Cit. APL Mater.* **3,** 41506 (2015).
12. Klemens, P. The Lattice Component of the Thermal Conductivity of Metals and Alloys. *Aust. J. Phys.* **7,** 57 (1954).
13. Stackhouse, S. & Stixrude, L. Theoretical Methods for Calculating the Lattice Thermal Conductivity of Minerals. *Rev. Mineral. Geochemistry* **71,** 253–269 (2010).
14. Kittel, C. *Introduction to Solid State Physics*. *Solid-State Physics (Fourth Extensively Updated and Enlarged Edition): An Introduction to Principles of Materials Science* (2010). doi:10.1007/978-3-540-93804-0
15. He, J. *et al.* Strong phonon scattering by layer structured PbSnS2 in PbTe based thermoelectric materials. *Adv. Mater.* **24,** 4440–4444 (2012).
16. Zheng, J.-C. Recent advances on thermoelectric materials. *Front. Phys. China* **3,** 12 (2011).

17. Callaway, J. & von Baeyer, H. C. Effect of Point Imperfections on Lattice Thermal Conductivity. *Phys. Rev.* **120,** 1149–1154 (1960).

18. Kim, W. *et al.* Thermal conductivity reduction and thermoelectric figure of merit increase by embedding nanoparticles in crystalline semiconductors. *Phys. Rev. Lett.* **96,** (2006).

19. Callaway, J. Model for lattice Thermal Conductivity at Low Temperatures. *Phys. Rev.* **113,** 1046–1051 (1959).

20. Amouyal, Y. Reducing Lattice Thermal Conductivity of the Thermoelectric Compound AgSbTe<inf>2</inf> (P4/mmm) by Lanthanum Substitution: Computational and Experimental Approaches. *J. Electron. Mater.* **43,** 3772–3779 (2014).

21. Khan, A. A., Khan, I., Ahmad, I. & Ali, Z. Thermoelectric studies of IV-VI semiconductors for renewable energy resources. *Mater. Sci. Semicond. Process.* **48,** 85–94 (2016).

22. Minnich, A. J., Dresselhaus, M. S., Ren, Z. F. & Chen, G. Bulk nanostructured thermoelectric materials: current research and future prospects. *Energy Environ. Sci.* **2,** 466 (2009).

23. Y.I. Ravich, B.A. Efimova, I. A. S. *Semiconducting lead chalcogenides*.

24. Lin, J. C., Hsleh, K. C., Sharma, R. C. & Chang, Y. A. The Pb-Te (lead-tellurium) system. *Bull. Alloy Phase Diagrams* **10,** 340–347 (1989).

25. Lead telluride (PbTe) energy gaps: Datasheet from Landolt-Börnstein - Group III Condensed Matter ·Volume 41C: ``Non-Tetrahedrally Bonded Elements and Binary Compounds I'' in SpringerMaterials (https://dx.doi.org/10.1007/10681727_720). doi:10.1007/10681727_720

26. Tung, Y. W. & Cohen, M. L. Relativistic band structure and electronic properties of SnTe, GeTe, and PbTe. *Phys. Rev.* **180,** 823–826 (1969).

27. Korkosz, R. J. *et al.* High ZT in p-type (PbTe)1-2x(PbSe)x(PbS)x thermoelectric materials. *J. Am. Chem. Soc.* **136,** 3225–3227 (2014).

28. James, D. J. New Approaches To Chalcogenide Materials For Thermoelectrics : Lead Telluride-Based Nanostructures And Facile Synthesis Of Tetrahedrite And Doped Derivatives. (2016).

29. Lo, S. H., He, J., Biswas, K., Kanatzidis, M. G. & Dravid, V. P. Phonon scattering and thermal conductivity in p-type nanostructured PbTe-BaTe bulk thermoelectric materials. *Adv. Funct. Mater.* **22,** 5175–5184 (2012).

30. Lensch-Falk, J. L., Sugar, J. D., Hekmaty, M. A. & Medlin, D. L. Morphological evolution of Ag2Te precipitates in thermoelectric PbTe. *J. Alloys Compd.* **504,** 37–44 (2010).

31. Bergum, K., Ikeda, T. & Jeffrey Snyder, G. Solubility and microstructure in the pseudo-binary PbTe–

Ag2Te system. *J. Solid State Chem.* **184,** 2543–2552 (2011).

32. Yakshibaev, R. A., Mukhamadeeva, N. N. & Kadrgulov, R. F. Phase relations, ionic transport, and diffusion in the alloys of Ag2Te□Cu2Te mixed conductors. *Phys. status solidi* **121,** 111–117 (1990).

33. Imamov, R. M. & Pinsker, Z. G. *DETERMINATION OF THE CRYSTAL STRUCTURE OF THE HEXAGONAL PHASE IN THE SILVER-TELLURIUM SYSTEM*. *Translated from Kristallografiya* **11,**

34. Li, J.-F., Liu, W.-S., Zhao, L.-D. & Zhou, M. High-performance nanostructured thermoelectric materials. *NPG Asia Mater.* **2,** 152–158 (2010).

35. Porter, D. A. & Easterling, K. . Phase Transformation in Metals and Alloys. *Chapman Hall* 1–5 (2014). doi:10.1007/s13398-014-0173-7.2

36. Fiss, A. L. & Eiss, A. L. TH11ER MOELECTRIC BO-NDING. STUDY THERMOELECTRIC BONDING STUDY.

37. Biswas, K. *et al.* High-performance bulk thermoelectrics with all-scale hierarchical architectures. *Nature* **489,** 414–418 (2012).

38. LaLonde, A. D., Ikeda, T. & Snyder, G. J. Rapid consolidation of powdered materials by induction hot pressing. *Rev. Sci. Instrum.* **82,** (2011).

39. Pei, Y., Lensch-Falk, J., Toberer, E. S., Medlin, D. L. & Snyder, G. J. High thermoelectric performance in PbTe due to large nanoscale Ag 2Te precipitates and la doping. *Adv. Funct. Mater.* **21,** 241–249 (2011).

40. Grossfeld, T., Sheskin, A., Gelbstein, Y. & Amouyal, Y. Microstructure Evolution of Ag-Alloyed PbTe-Based Compounds and Implications for Thermoelectric Performance. *Crystals* **7,** 281 (2017).

41. Tom Grossfeld. And, Microstructure Evolution Applications, Enhancement of the Thermoelectric Conversion Efficiency of PbTe-based Compounds for Renewable Energy. (technion, 2015).

42. ASTM International. ASTM C373-16^1: Standard Test Methods for Determination of Water Absorption and Associated Properties by Vacuum Method for Pressed Ceramic Tiles and Glass Tiles and Boil Method for Extruded Ceramic Tiles and Non-tile Fired Ceramic Whiteware Products. *Annu. B. ASTM Stand.* 5 (2016). doi:10.1520/C0373-16.2

43. Parker, W. J., Jenkins, R. J., Butler, C. P. & Abbott, G. L. Flash method of determining thermal diffusivity, heat capacity, and thermal conductivity. *J. Appl. Phys.* **32,** 1679–1684 (1961).

44. Cowan, R. D. Pulse method of measuring thermal diffusivity at high temperatures. *J. Appl. Phys.* **34,** 926–927 (1963).

45. Cape, J. A. & Lehman, G. W. Temperature and finite pulse-time effects in the flash method for

measuring thermal diffusivity. *J. Appl. Phys.* **34,** 1909–1913 (1963).

46. Gault, B., Moody, M. P., Cairney, J. M. & Ringer, S. P. *Atom Probe Microscopy*. **160,** (2012).

47. Müller, E. W. & Bahadur, K. Field ionization of gases at a metal surface and the resolution of the field Ion microscope. *Phys. Rev.* **102,** 624–631 (1956).

48. Muller, E. W., Panitz, J. A. & McLane, S. B. The Atom-Probe Field Ion Microscope. *Rev. Sci. Instrum.* **39,** 83–86 (1968).

49. Kelly, T. F. & Larson, D. J. Atom Probe Tomography 2012 Keynote Topic. *Annu. Rev. Mater. Res* **42,** 1–31 (2012).

50. Kelly, T. F. & Miller, M. K. Atom probe tomography Design of a femtosecond laser assisted tomographic atom probe. *Cit. Rev. Sci. Instruments Rev. Sci. Instruments Rev. Sci. Instruments J. Appl. Phys. Appl. Phys. Lett. J. Appl. Phys. J. Appl. Phys.* **78,** 31101–43705 (2007).

51. Miller, M. K. & Forbes, R. G. Atom probe tomography. *Mater. Charact.* **60,** 461–469

52. David J. Larson, Ty J. Prosa, Robert M. Ulfig, Brian P. Geiser, T. F. K. *Local Electrode Atom Probe Tomography: A User's Guide*. (springer, 2008).

53. cameca. No Title. Available at: http://www.cameca.com/products/apt/leap5000.

54. Lorensen, W. E., Cline, H. E., Lorensen, W. E. & Cline, H. E. Marching cubes: A high resolution 3D surface construction algorithm. in *Proceedings of the 14th annual conference on Computer graphics and interactive techniques - SIGGRAPH '87* **21,** 163–169 (ACM Press, 1987).

55. Babanly, D. M., Aliev, I. I., Babanly, K. N. & Yusibov, Y. A. Phase equilibria in the Ag_2Te-PbTe-Bi_2Te_3 system. *Russ. J. Inorg. Chem.* (2011). doi:10.1134/S0036023611090038

56. Finefrock, S. W. *et al.* Measurement of Thermal Conductivity of PbTe Nanocrystal Coated Glass Fibers by the 3ω Method. doi:10.1021/nl400558u

57. Królicka, A. K., Mirowska, A., Materna, A. & Piersa, M. Synthesis and Ball Milling Effect on Thermal Conductivity of PbTe Based Alloys. *Cryst. Res. Technol.* **52,** 1600376 (2017).

פגמים ומשטחי ביניים בתרכובות עופרת טלוריד המסוגסגות בכסף ליישומים תרמואלקטריים

חיבור על מחקר לשם מילוי חלקי של הדרישות לקבלת התואר מגיסטר למדעים בהנדסת חומרים

אריאל שסקין

הוגש לסנט הטכניון - מכון טכנולוגי לישראל אלול תשע"ח

חיפה, אוגוסט 2019

תודות

מחקר זה נעשה תחת הנחייתו המסורה של פרופ 'מ 'ירון אמויאל מהפקולטה למדע והנדסה של חומרים בטכניון – מכון טכנולוגי לישראל.

אני מודה לקרן מינרווה על המענק שאפשר לי לערוך ניסויים במכון המחקר מקס פלנק בדיסלדורף , גרמניה.

תקציר

המרה של חום מבוזבז לחשמל נעשית על ידי שימוש במחולל תרמואלקטרי, שמבוסס על "אפקט סיבק".

תרכובת העופרת-טלור (PbTe) שנחשבת לאחת התרכובות הטובות עבור מחוללים תרמואלקטריים שעובדים בטמפרטורות ביניים עקב מקדם ביצוע תרמואלקטרי (ZT) גבוה. מקדם זה מייצג את יעילות ההמרה התרמודינמית, ניתן לשפר אותו ע"י העלאה של המוליכות החשמלית ומקדם סיבק ובאותו זמן הורדה של המוליכות התרמית. דרך שכיחה לשיפור התכונות התרמואלקטריות היא באמצעות סגסוג החומר באלמנטים נבחרים, מעל גבול המסיסות שלהם כדי לעודד גידול מתבדלים של פאזה שניה, שתנמיך את המוליכות התרמית הגבישית עקב פיזור פונונים.

במחקר שלנו סיממנו עופרת-טלור עם כסף (3.3 at. % Ag) וביסמות (0,0.2 , 0.4 at. % Bi) כאשר הכסף משמש לגידול מתבדלים ואטומי הביסמות משמשים כתורמי אלקטרונים.

אנו עוקבים אחר התפתחות המיקרומבנה של שתי הסגסוגות בזמני זיקון שונים בטמפ' של 380 מ"צ ובוחנים כיצד היא תשפיע על תכונות הטרנספורט התרמואלקטריות ומעונינים למצוא את התהליך האופטימלי עבור חומר שכזה. במחקר קודם במעבדה נעשו ניסויים רבים בטמפ' שונות(450,400,380 מ"צ) , במחקר זה המשכנו לבדוק את הטרנד עבור 380 מ"צ בזמנים שונים (עם שמירה באותם הריכוזים). הכנת הדגמים כללה התכה בואקום והומוגוניזציה, וכבישה חמה לאחר כתישה של החומר.

כמו כן המשכנו בחקירת תנאים אופטימליים לתהליך הנ"ל ע"י בדיקה של הסגסוגת בזיקון של 370 מ"צ בזמנים שונים.

המוליכות התרמית נבדקת באמצעות Laser flash analysis (LFA) ותכונות חשמליות נעשו באמצעות Four point probe המצויד במודול מיקרו-חימום.

מצאנו שהמוליכות התרמית של הדגמים ללא הביסמות יורדת לאחר 6 שעות זיקון ועולה כאשר מזקנים את החומר לזמנים של 48 שעות, המוליכות החשמלית לעומת זאת יורדת מונוטונית עם עליה בזמני זיקון.

המאפיינים שעוזרים לנו להעריך את התכונות הללו הם הצפיפות המספרית של המתבדלים (N_V) וריכוז הכסף המטריצה. השתמשנו בטכניקות אפיון מתקדמות הכוללות מיקרוסקופית אלקטרונים סורקת ברזולוציה גבוהה (HRSEM) ומיקרוסקופיה משלבת של מיקרוסקופית אלקטרונים חודרת (TEM) וטומוגרפית דגימה אטומית (APT) ליכולת גילוי מספקת של המתבדלים.

באמצעות השילוב הזה יש ביכולתנו להעריך בצורה כמותית את המתבדלים של הכסף-טלור, באמצעות משטחים שווי ריכוז כמו כן באמדן תלת מימדי בניגוד לTEM או SEM.

לAPT יש יכולת הערכה של ערכי צפיפות מספרית בערכים אופייניים של 10^{24} m^{-3} ומאפשר הערכה של ריכוז הכסף באיזורים בין המתבדלים.

שילוב האמצעים הניסויים האלה, לראשונה , אפשר לנו לעקוב אחר התפתחות המיקרומבנה של תרכובות מבוססות על עופרת טלור והשפעת התפתחויות אלה על התכונות התרמואלקטריות שלהן.

בדומה לתוצאות שקיבלנו עבור מיקרוסקופית אלקטרונים סורקת, גם כאשר בוחנים את החומר בסקלה ננומטרית באמצעות הטכניקות המתקדמות, גילינו כי גידול המתבדלים הינו כפי בציפינו:

תחילה יש מתדבלים גדולים וקטנים בסטויכומטריות שונות שנובעים מסופר הסטורציה של הכסף במטריצה. בנוסף ישנה התבדלות תחילתית בזמן החיסום של החומר. לאחר זיקון בזמנים קצרים מקבלים כמות רבה של מתבדלים ננומטרים והצפיפות הנפחית של המתבדלים עולה ולבסוף לאחר זמנים ארוכים כמעט שלא ניתן להבחין במתדבלים קטנים, עקב מנגנון ההתגסות של החומר.

התנהגות זו מתארת את התכונות התרמואלקטריות שהתקבלו עבור חומרים אלה. עליה בצפיפות המתבדלים מורידה את הדרך החופשית הממוצעת למעבר חם קטנה ומורידה את המוליכות התרמית. כאשר ההתגסות קרתה וכמות המתבדלים ירדה משמעותית , קיבלנו ערכים נמוכים יותר עבור המוליכות התרמית.

בהתחלה, הצגנו את הביסמוט לחומר זה ע"מ לשפר את התכונות החשמליות שלו החומר כמסמם מסוג "תורם". נוכחנו לגלות שלביסמוט יש תפקיד נוסף בתהליך, הוא מעכב את גידול המתבדלים.

דגמים עם ביסמוט הראו צפיפיות מתדבלים נמוכה בהרבה מהדגמים ללא הביסמוט אך ,ללא הפתעה, בעלי מוליכות חשמלית גבוהה מהם.